A New Powertrain Architecture: From Electromagnetic-Structural Dynamics to Platooning

by

Chenyu Yi

A dissertation submitted in partial fulfillment
of the requirements for the degree of
Doctor of Philosophy
(Mechanical Engineering)
in The University of Michigan
2020

Doctoral Committee:

Professor Bogdan I. Epureanu, Chair
Professor Heath Hofmann
Professor Gregory Hulbert
Assistant Professor Bogdan I. Popa
Doctor Matthew P. Castanier, U.S. Army
Doctor Denise M. Rizzo, U.S. Army

Chenyu Yi
albertyi@umich.edu
ORCID: 0000-0002-5644-7579

For my family and beloved ones

ACKNOWLEDGEMENTS

I would first like to thank my supervisor, Prof. Bogdan I. Epureanu, without whom I would not have been able to learn to research, and without whom I would not have made it through my journey of Ph.D. study. Your insightful feedback and comments helped me shape my mind as a researcher.

I would like to acknowledge my co-advisor, Prof. Heath Hofmann, for selflessly sharing his expertise and knowledge to support my life and research project. I was lucky to know Prof. Hofmann in class and have a chance to work with him in research.

I own my thanks to the rest of my committee members, Prof. Gregory Hulbert, Prof. Bogdan I. Popa, Dr. Matthew P. Castanier, and Dr. Denise M. Rizzo. Your support helped my dissertation work reach a higher level.

I would also like to thank my colleagues in Applied Nonlinear Dynamics of Multi-Scale Systems Lab. Special thanks to Dr. Seunghun Baek for his kind support for me during my first year in the group, and Dr. A. Emrah Bayrak for his valuable guidance though my study.

Finally, I would like to thank my families for their unconditional support and understanding. I could not have completed this dissertation without the support and love from my families and friends.

TABLE OF CONTENTS

CHAPTER

LIST OF FIGURES

Figure

LIST OF TABLES

Table

ABSTRACT

Electrification and vehicle-to-vehicle connectivity have become two of the major areas of vehicle development in recent years. Electrified vehicles show significant advantages because of their high performance in fuel economy and low emissions compared to conventional vehicles. Hybrid electric vehicles (HEVs) share a significant amount of market among electrified vehicles. Although HEV development has resulted in a variety of powertrain architectures and designs, novel high-performance powertrain solutions with fewer components and low cost remain an important need. In addition, common HEV configurations use small internal combustion engines, which can suffer from high torque fluctuations detrimental for NVH performance and safety. Advanced powertrains that absorb these fluctuations efficiently are needed. This thesis presents a novel HEV powertrain architecture without any planetary gears or clutches. Using physics-based component model, a proof-of-concept powertrain model is implemented and demonstrated ability to remove over 99.5% torque fluctuation and fulfill vehicle driving demands. A comprehensive design and control optimization for the novel powertrain is performed. A single utility function is designed by combining multiple objectives, and is tuned using the Pareto front of the novel powertrain performance to obtain different optimal powertrain designs. Optimal novel powertrain designs show comparable performance with optimal designs of commercially available power-split benchmark powertrains. Torque fluctuations in HEVs may result in electromagnetic-structural (EMS) phenomena within the electric machines of the powertrain. The distributed electromagnetic (EM) forces that exist in such devices can lead to structural deformations. These deformations may in turn change the EM forces. Consequently, the mechanical and EM behaviors are coupled. Periodic forces generated by permanent magnets or windings and other disturbances to the EM device can lead to excitation of specific structural resonances due to EMS coupling. Existing EMS models are usually 2D and do not capture the EMS coupling. Thus, a model that accurately and efficiently captures EMS phenomena is required. To capture the EMS phenomena, displacement-dependent EM forces are introduced in the modal space to the structural dynamics of electric machines. Both linear and nonlinear approximations of EM forces are calculated using high-fidelity FEA models, forming a reduced-order model (ROM) with EMS coupling, namely the EMS ROM. The dynamics of the EMS ROM is similar to a damped dynamical system governed by Mathieu's equation, which exhibits parametric excitation. The EMS ROM is used to compute the stability transition threshold for the parametric excitation. Parametric resonance peaks are revealed in the responses from an unstable device with EMS. In addition, a frequency shift of the primary resonance peak caused by (nonlinear) EM force harmonics is detected. Time-domain analyses using the high-fidelity FEA model confirm the EMS phenomena and accuracy of the EMS ROM. Multiple vehicles, each with an advanced powertrain can be used in platoons to enhance fuel economy, road capacity, and safety compared to a single vehicle. Studies that focus on platooning usually do not focus on task-based longitudinal planning and do not capture detailed powertrain operations, which impact the control and energy consumption of the overall platoon. In this thesis, multiple vehicles, each equipped with the novel powertrain, are investigated when they form a platoon and drive on a specified path. The drive schedule and vehicle controllers are optimized to minimize the total energy consumption of the platoon. Energy optimization requires an integrated vehicle-following model and a high-fidelity powertrain model. In addition, component-level, vehicle-level, and platoon-level constraints are applied. Parametric studies are performed for both homogeneous and heterogeneous platoons. Optimization is shown to effectively reduce the maximum headway error by an order of magnitude and enhance energy saving of 17% to 37%.

CHAPTER I

Introduction

1.1 Motivation and Background

With the purpose of reducing emissions and improving fuel economy, policies on vehicle fuel consumption and emission have been set up around the world. This has triggered significant new developments in hybrid electric vehicles (HEVs) and platooning over recent years [124, 5, 109, 3]. Recent studies have proved that HEVs outperforms conventional vehicles in fuel economy and emissions [82, 40, 49, 107, 22, 104]. For decades of development, HEV powertrain architectures/configurations have become standardized. The HEV powertrain configurations can usually be categorized as series, parallel, and power-split. New architectures that are out of the three categories still exist and can demonstrate comparable performance to best existing powertrain configurations. Exploring and optimizing new powertrain architecture is meaningful. Platooning of vehicles, compared to single vehicle operations, can reduce energy consumption of driving, boost road capacity, and improve safety [4, 20, 11, 81]. Vehicle electrification and connection are vital parts of solutions to requirements and regulations on energy efficiency and emission. The two research areas are growing and more overlaps of them will be emerging. Platooning of electrified vehicles contribute to future development of transportation systems. The controls from the component level within electrified powertrains up to the platoon level are all coupled and impact the overall energy efficiency of transportation. Thus efficient operations and controls of platoons of electrified powertrains are necessary.

On the scale of vehicles, hybrid electric vehicles use more than one type of power source. Among all combinations of available power sources, an ICE plus an electric battery system that drives one or more electric motors/generators is the most popular. Since the ICE is not their only power source, typical HEVs use smaller ICEs with fewer cylinders compared to conventional vehicles. Such ICEs suffer from higher torque fluctuations which lower the noise, vibration, and harshness (NVH) performance [18, 115, 83]. Such fluctuation, plus the AC currents, could cause parametric resonances within the electric machines, because the electromagnetic force and structural dynamics of electric machines are coupled. For the purpose of this study, the coupling is referred to as electro-magnetic-strucutral (EMS) coupling. A multiphysics modeling framework that efficiently and accurately captures the the EMS coupling is needed for comprehensive structural analysis of electrified powertrains.

1.2 State of the Art

1.2.1 Electric Machines

Electric machines play a key role in the powertrain of these new vehicles. In particular, the design of powertrains for electric vehicles requires high performance electric motors with high power density and low weight [24, 154, 116, 117, 141]. Moreover, with the increasing demand for low emission vehicles and the development of novel battery technologies, the trend of vehicle electrification and application of high performance electric machines will most likely grow.

The design of systems with EM devices requires accurate modeling methodologies for such devices. The objectives of such models include magnetic force, structural, and thermal analyses [151, 144, 86]. Studies have looked into the impact electromagnetic force on the structure of electric machine [54, 153, 98, 105]. In general, the two commonly used methods for magnetic force analysis are the Maxwell stress tensor method and the co-energy method. The Maxwell stress tensor method uses spatial derivatives, and can determine the spatial distribution of the EM force [135, 118, 27]. However, in finite element analysis (FEA) the application of the Maxwell stress tensor method requires high-order finite differences in space. Hence, the accuracy of the Maxwell stress tensor method is highly dependent on the quality of the mesh. As an alternative, researchers have applied the co-energy method to find the net force in both lumped parameter models and FEA models [28, 46]. The co-energy method does not require spatial derivatives; moreover, its computational cost is typically lower than that of the Maxwell stress tensor method.

1.2.2 Structural Analyses

1.2.2.1 Reduced-Order Models

In structural analysis, reduced-order models (ROMs) are commonly used [13, 56, 57, 50, 155]. ROMs require a modal analysis of the structure and projection onto the modal space. Modal analysis decouples the structural equations of motion, limiting ROMs to a frequency range of interest that can greatly reduce the number of equations for structural dynamics. In addition, for structures with cyclic symmetry, the FEA model of a single sector is needed for modal analysis [93]. Various ROMs have been developed in the past year for both pristine [125] and mistuned structures [13, 21, 99, 99], or structure with mulitple-physics interface [47, 31, 123, 34, 35, 32]. Typically, ROMs can reduce the computational cost from full model by orders of magnitude, depending on the resolusion of full model, symmetry of structure, and physics complexity.

1.2.2.2 Parametric Resonances

The stiffness and damping within a common dynamic system is usually considered constants. However, when stiffness and/or damping are time-varying and periodic, the stability of the system is subject to change. These periodic parameters create parametric excitations to the system. Parametric resonances differ from usual resonances that are caused by force harmonics. Parametric resonances can co-exist with usual resonances. Methodologies to analyze the stability of dynamic systems under parametric excitations were established in previous studies [102, 66]. In these studies, a characteristic equation called the Mathieu's equation is analyzed. The Mathieu's equation is both time and mass normalized, and can represent most systems with parametric excitations. The unique solving technique presented in [102] is able to determine the stability of system in frequency domain, given the intensity of parametric excitation.

1.2.3 Hybrid Elctric Vehicles

Solutions have been developed to suppress the torque fluctuations within powertrains. Mechanically dampening torque fluctuations is one way to address the torque fluctuation problem and enhance NVH performance for HEVs. However, the energy loss in such approaches can be large, and that can affect the efficiency of the powertrain. Previous studies of NVH in HEV powertrains focus mostly on vibrations which occur during the transient period upon mode shifting, clutch engaging or disengaging [131, 52, 63].

Typical configurations of HEV powertrains fall into three categories, namely series, parallel, and power-split. Studies of such architectures have been carried out recently [78, 76, 108, 41, 45, 134, 25, 84, 48] with most focusing on power-split hybrids. Other than that, more limited research focuses on series and parallel hybrids [132, 44]. Related studies for commercial HEV powertrains have been done by Chan [23], and

Wu et al. [138].

To study HEVs, models of powertrain architectures are needed. These include modeling methods and tools for powertrains, system dynamics, and emissions. Powertrain dynamics modeling usually requires integration of component dynamics and vehicle dynamics. Powertrain performance is typically evaluated at vehicle level, like vehicle energy consumption and fuel economy. In past studies, Liu et al. developed a widely applied modeling framework for power-split powertrain dynamics [79, 80]. Such modeling framework requires building torque-angular acceleration mapping matrix rigorously based on powertrain configuration. The matrix creation process is efficient when applied on power-split powertrain configurations that apply planetary gear as transmission can connection among powertrain components. Kim et al. have designed a novel multi-mode parallel HEV powertrain and assessed its fuel economy. Multi-mode operation is realized by planetary gears [65] and by engaging or disengaging different power sources. For example, Zhu et al. have designed a HEV powertrain with a single electric machine and two planetary gears [152]. Millo et al. developed models and a prototype for an urban hybrid bus [87]. Bougrine et al. applied a chemistry-based method and simulated CO and NO emissions models [17]. Also, several researchers have developed modeling tool for HEV architectures with embedded rule-based controllers [26].

Control are also needed for designing HEVs of different topologies, including control and power management of single powertrains and of multi-mode powertrains. Al-Aawar et al. have designed an optimal control strategy which maximizes fuel economy by using a mathematical search algorithm, and maximizes drivability by using a fuzzy logic algorithm [2]. Hou et al. have developed a control strategy based on estimating trip information acquired using statistical methods [51]. Other approaches use game theory controllers developed by Dextreit et al. Their time-independent control strategy manages power by judging the cost of fuel consumption, emissions, and battery SOC [29]. In 2014, Finesso et al. designed and optimized a diesel parallel hybrid powertrain [39]. Torres et al. developed an optimal power management strategy for plug-in hybrid electric vehicles [126]. In contrast, Lee et al. successfully created a controller of continuously variable transmission (CVT) ratio to improve parallel HEVs [70]. Kum et al. have developed a real-time optimal power and catalyst management strategy for plug-in HEV and parallel HEV based on studying the characteristics of dynamic programming results [68, 67]. Zhang et al. have proposed a real-time control strategy that selects the most power efficient mode of a multi-mode HEV powertrain to achieve near-optimal fuel-economy [147]. A similar method is described in Shabbir and Evangelou's work [113], Other control strategies on multi-mode HEVs are found in the work of Zhang et al. [145], Borhan et al. [16], Ahn et al. [1], Katrašnik [60], and Lin et al. [75], among others.

Optimal control methods have been developed for HEV powertrains. For example, dynamic programming (DP) is widely applied in HEV powertrain control optimization [133][69][77]. DP can find the global optimal control for best performance with given component sizes. However, dynamic programming is not a real-time control strategy, and its computational cost is high. Another approach of control optimization is the Pontryagin's minimum principle (PMP). The PMP was applied widely in optimal control for HEV powertrains [111][64]. The PMP, when applied to optimize HEV powertrains, typically requires partial derivatives of the rate of change of the battery state of charge (SOC). These derivatives, in many cases, cannot be approximated very accurately. For that reason, a simplified control method based on PMP was developed, namely the equivalent consumption minimization strategy (ECMS) [95][112], as a near-optimal control strategy for HEVs. The performance with this control approach is lower but very close to the optimal performance [64]. The advantage of ECMS is the relatively low computational cost. In this study, ECMS is applied to evaluate the performance of powertrain designs with different component sizes.

With given devices, a certain (typically large) number of possible powertrain topologies exist. It is of great interest to finding which of these topologies are best, namely maximize for some utility function such as fuel economy. Zhang et al. have developed an exhaustive search methodology for optimal designs for topologies with given power sources and planetary gear sets and clutches [146]. Mohan et al. have designed a framework with similar functionality, but using a systematic search method which compares all possible topologies simultaneously [88]. Silvas et al. have designed an automatic HEV topology generator which generates feasible topologies using given power sources and transmission components [114].

1.2.4 Hybrid Powertrain Optimization

The design optimization and the control optimization problems for HEV powertrains are typically coupled. Optimization methods have been developed for such coupled design and control optimization problems. These methods include sequential, iterative, nested, and simultaneous approaches [37, 9, 10]. Among these approaches, the nested and the simultaneous approaches are more reliable in finding optimal solutions. Nested approaches search different designs in an outer loop, while the optimal control strategy forms an inner loop for each design to find the optimal performance. Nested approaches are able to make use of existing control methods compared with simultaneous approaches.

1.2.5 Platooning

1.2.5.1 Vehicle-to-Vehicle Connection

The primary goal of platooning is to save fuel for vehicles. The vehicles in a platoon benefit from aerodynamic drag reduction. The drag reduction is mainly caused by the propagation of wake and depends on rearward distance and vehicle speed [122, 130, 106]. Experiments and simulations have shown that platooning can improve fuel efficiency, safety, and road capacity [128, 11, 42].

Platooning involves inter-vehicular communications and controls. The communications can be unidirectional or bidirectional. The topology and delays of communication does have an impact on the control of platoons [59, 12, 38, 30, 149], while the control of platoons can be centralized or distributed [71, 15, 129, 72]. One key purpose of platoon-level control is maintaining string stability, regardless of topology or delay of communication. A simple yet classic strategy that achieves string stability is the adaptive cruise control (ACC) [53, 36]. The limitation of of such strategy is the lack of V2V/V2R/V2I communications. To address this issue, control strategies that integrates communications into ACC have been developed. Such a collective control strategies are called the cooperative ACC (CACC). The CACC, if designed correctly, can ensure string stability and save control efforts compared to ACC [140]. In designing of advanced CACC strategies, the inter-vehicular distance or headway is an important parameter. The selection of headway affects the aerodynamic drag reduction, safety, and road capacity [121]. The trade-off between safety and fuel efficiency is an important aspect of designing CACC strategy. Cooperative adaptive cruise control strategies have been designed and developed [74, 100, 101, 62]. Experimental verification is usually effective to prove the reliability and robustness of the CACC strategy [90].

In addition, comprehensive dynamics and control models known as vehicle following models (VFMs) have been developed [110, 127, 91, 119, 33]. The development of VFMs is to study high-level performance such as overall fuel economy, traffic throughput and traffic flows [19].

1.2.5.2 Longitudinal Planning

Motion planning of vehicles and robots has become a major link in autonomy. The focus in planning is mostly on path planning in a field for either holonomic or nonholonomic system [89, 6, 97]. The objective of path planning is on generating a graph that the object can travel from vertex to vertex through edges, and search for a feasible or optimal path between two points on the graph [120, 61, 85, 58]. In path planning problems, the speed of object is usually ignored by assumption.

Longitudinal and lateral vehicle motion planning require time derivatives of position information of vehicle. Longitudinal planning can be real-time or full-horizon. In real-time longitudinal planning, model-predictive control (MPC) like methods are usually applied [139, 92, 73, 148, 43]. Real-time control can be flexible to varying objective, environment, and road conditions. Nevertheless, full-horizon longitudinal planning can be beneficial to task-based operating vehicles, like postal vehicles, delivery trucks, and even some passenger vehicles that belong to people drive to work daily. Such vehicles drives repetitively on the same path. Thus, if the longitudinal motion of vehicle on its task is optimized, energy consumption can be reduced potentially.

1.3 Contributions of This Work

To summarize, this work presents a multi-physics ROM that captures EMS coupling and analyzes the system stability accurately and efficiently, the design, modeling and control of a novel hybrid electric powertrain architecture, the control and design optimization of the novel powertrain, and the drive schedule and vehicle control optimization for platoon of HEVs that are equipped with the novel powertrain.

1.3.1 Capturing EMS Phenomena

Within electric machines, EM forces and structural deformations are coupled. However, the modelling methodology for EMS coupling in previous studies has been either limited. A lot of the models are in 2D and the electromagnetic forces are therefore approximated. In addition, the EMS coupling have not been accurately and efficiently captured. Therefore, in this work, we present **multi-physics ROMs**

that capture structural vibrations, EM forces, and the EMS coupling. The coupling is considered as a deformation-dependent EM force. Given that the ROMs are built in the modal space, **a modal EM force calculation method based on the co-energy method** is presented. In addition, the EM forces are functions of currents that are functions of time. Thus, time-varying parameters exist in the equations of motion. These time-varying parameters create parametric excitations to the system. In this study, a proof-of-concept device was designed and optimized to analyze parametric resonances. A FEA model was created to collect parameters that are necessary to build multi-physics ROMs for this design and to verify the stability of the system using a frequency domain analysis. In addition, The frequency domain response was verified using time domain analysis on the FEA model.

1.3.2 Novel Hybrid Electric Powertrain Architiecture

We have designed a novel hybrid electric powertrain in this work. The powertrain system analyzed in this work takes advantage of **a specialized electric machine which has a stator that is allowed to rotate** [142]. This machine is connected to the ICE (which unavoidably exhibits torque fluctuations) and to another, conventional electric machine. Having a rotating stator enables the first machine to adjust the angular velocity in the powertrain downstream of the ICE. The conventional machine controls the torque transmitted to the wheels, and also **suppresses torque fluctuations** caused by the ICE. Typical mechanical connections for HEVs such as **planetary gears and clutches are not needed** in this novel powertrain. This new architecture does not fall into any of the three existing HEV configurations, but is viewed as between a series and a power-split.

To evaluate the performance of the new powertrain architecture, a vehicle-level model is created. This includes a two-level control framework which sets the ICE operating point and distributes power to the electric machines. The controller uses an **event-based power management** strategy where events represent changes in driving conditions and vehicle status.

The vehicle-level model and its control were implemented in Matlab Simulink® with separate **physics=based models** for the powertrain and vehicle components, namely: ICE model, electric machine models, battery model, vehicle dynamics, and driver model. The electric machine models contain their drive, including the power electronics, and real-time field-oriented controllers. The component models and controllers were connected to obtain a vehicle-level model. Each component of the model was tested individually. With the complete powertrain model, tests verify that the functionality of the powertrain system are the same as designed. These tests include vehicle driving on a single and multiple drive cycles, which monitor the functionality of individual devices and components, and the power sustaining of the powertrain system over relatively long times of driving.

1.3.3 Design and Control Optimization of Novel Powertrain

The potential of each new architecture can be estimated based on its optimal performance, which is largely based on the powertrain design, component sizes, and control scheme. Metrics used to quantify the optimal performance typically include fuel economy, 0–60 mph acceleration time, cost, etc., or a combination thereof [8] [136].

The novel hybrid electric powertrain architecture illustrated in Fig. 1.1 was proposed in a previous study [143] in which the component sizes are arbitrarily selected only to prove the functionality of the novel architecture, and the control scheme was rule-based and non-optimal. Either using components with larger size or employing optimal control was able to improve the fuel economy, as shown in Fig. 1.2. The optimal control strategy illustrated in this example is dynamic programming (DP).

The focus of the current study was to apply control and design optimization techniques to **determine the potential performance of the novel powertrain**

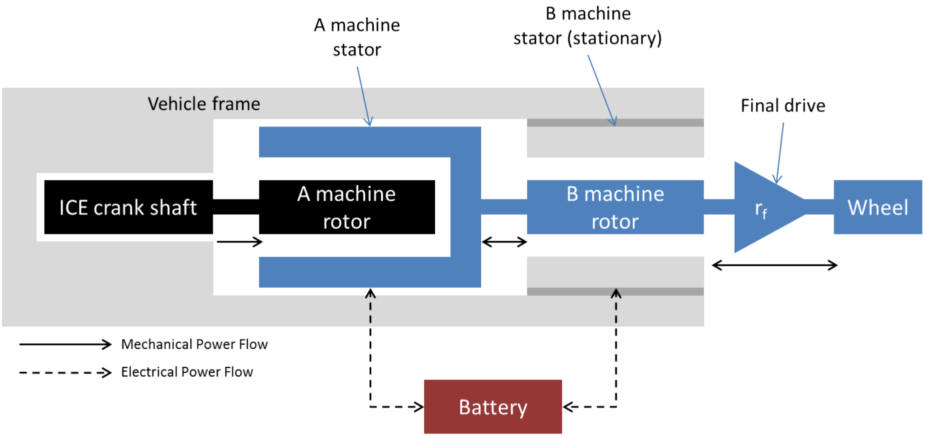

Figure 1.1: Architecture of a novel hybrid electric powertrain

architecture [141]. This included optimizing the various components, including the electric machines (the two machines denoted A and B), battery, and final drive gear ratio. The major objectives of the optimization is maximizing the fuel economy and minimizing the component sizes. When building the vehicle and powertrain model, a **physics-based modeling method** was applied to the electric machines and battery pack, which differs from scalable maps in conventional powertrain modeling. While the focus of this study was passenger sized vehicles, the same method is also applicable to other types of vehicles.

Here, the design problem was specifically related to the powertrain components; thus, the architecture of the powertrain remained fixed throughout. A near-optimal control simulation model that included the ECMS was constructed to evaluate the performance of each design. To solve the multi-objective optimization problem, Pareto front is searched and approximated by evaluating multiple randomly generated designs in design space. Single objective function is formulated using weighted sum of the two individual objectives. Combining with Pareto front, different optimal powertrain design can be obtained by adjusting the weight in single objective function. The optimal design obtained here requires information of Pareto front, which is only an approximation. Thus, the single objective powertrain optimization is necessary.

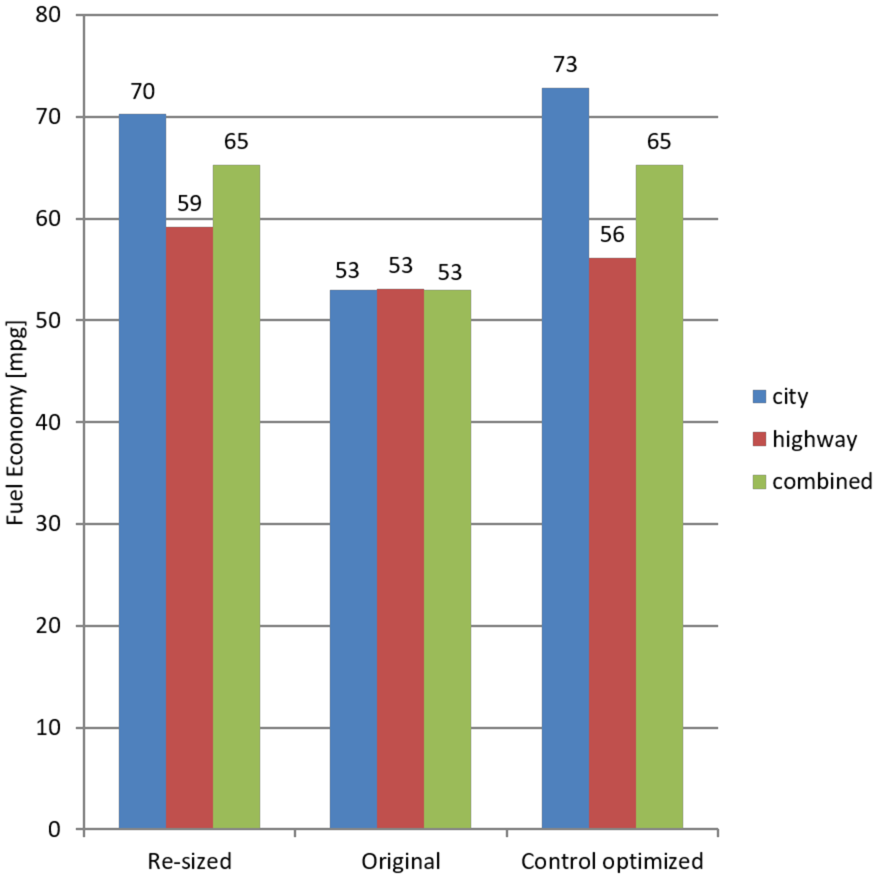

Figure 1.2: Fuel economy was improved by up-sizing components or applying optimal control

A polynomial **surrogate model** is developed to represent the ECMS model to accelerate the optimization process. The single objective optimization process is depicted in Fig. 1.3.

Multiple optimal designs are obtained with different relative weight between component size cost and fuel cost. To verify the optimal designs for novel powertrain, four **commercially available power-split HEV powertrains are selected as benchmark powertrains**. The benchmark poowertrains are and evaluated and optimized. Power-split configurations are selected as benchmarks due to their similary with the novel powertrain. **Similar component functionalities and operations can be observed between novel and benchmark powertrains**. The optimal

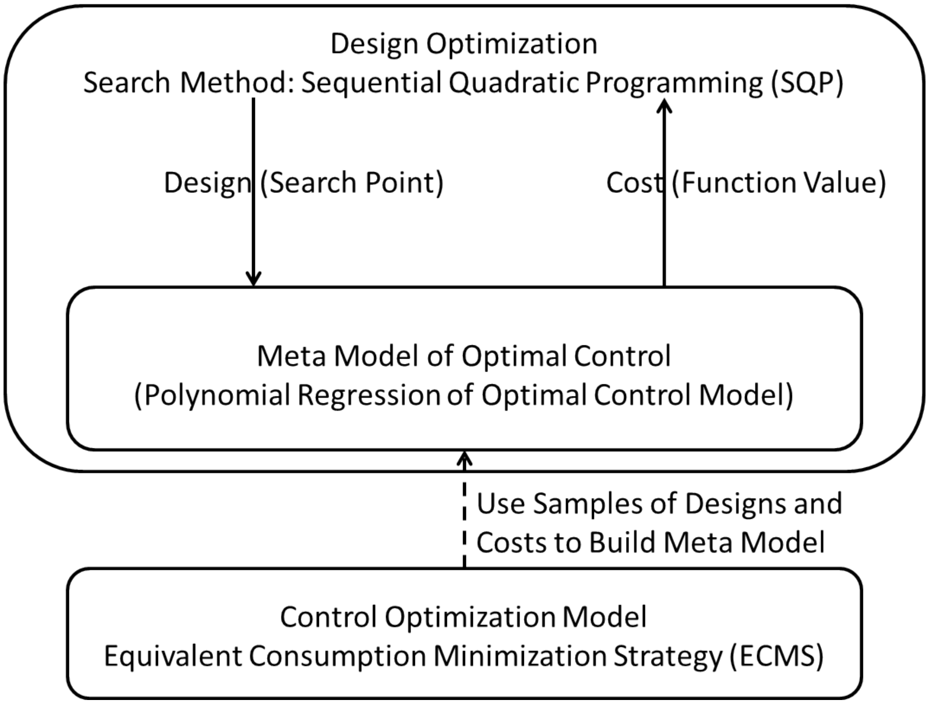

Figure 1.3: Block diagram of the system-level optimization

designs for benchmark powertrains are compared to those for novel powertrain, with same weights in single objective function. The results show that the novel powertrain produces comparable performance to benchmark powertrains.

1.3.4 Platooning of Electrified Powertrains

The platooning of electrified vehicles is desired for future transportation. Nevertheless, interaction of electrified powertrains and energy efficiency of a platoon is by far undermined. The components of electrified powertrains are all coupled together. The power management decisions are made by a supervisory controller based on the power demand from the driver or vehicle. Determining the power demand of each individual vehicle is the key to platooning. Thus the component status impacts the platoon operations. The drive schedule design for platoons in a specific task was not rigorously studied. The optimization of drive schedule design of vehicles can therefore improve energy efficiency in platoon operations.

In this work, a **modeling and optimization framework** was built for platoons of HEVs. The vehicles in this study are equipped with the novel hybrid electric powertrain. The study is aimed at analyzing and optimizing the energy efficiency and quality of vehicle following while moving the connected vehicles from the starting point to destination. The road grade along the way is specified. Inter-vehicular interaction includes the drag reduction [122] of vehicles and vehicle communications. We employed adaptive ECMS as the power management strategy for each individual vehicle. **The drive schedule and vehicle controllers are optimized to minimize energy consumption while maintaining minimal vehicle following error and relatively high vehicle speed**.

The modeling and optimization framework is applied on homogeneous platoons and heterogeneous platoons. Homogeneous platoon contain all identical vehicles while the size of vehicle or powertrain components can vary from vehicle to vehicle in a heterogeneous platoon. Parametric studies are designed for both homogeneous and heterogeneous platoons. Reference headway and its impact on optimal drive schedule design is explored for homogeneous platoon. The order of vehicles in a heterogeneous platoon is investigated. Optimization is shown to effectively reduce the maximum headway error by an order of magnitude and enhance energy saving of 17% to 37%.

CHAPTER II

Multi-Physics ROMs for EMS Coupling

2.1 Structural ROMs

A class of reduced-order modeling techniques use full-order finite element models and projection. In this study, the multi-physics ROMs apply modal projection to construct a structural ROM as a precursor for building the multi-physics ROMs.

A structural ROM can be built by carrying out modal analysis on the structure of interest. The full-order equation of motion of the structure can be expressed as follows

$$\mathbf{M}\ddot{\mathbf{x}} + \mathbf{C}\dot{\mathbf{x}} + \mathbf{K}\mathbf{x} = \mathbf{0}, \tag{2.1}$$

where $\mathbf{M}$, $\mathbf{C}$, and $\mathbf{K}$ are the mass, damping, and stiffness matrices, and $\mathbf{x}$ is the vector of displacements for all degrees of freedom. By projecting Eq. (2.1) onto the modal space, the structural ROM can be expressed using the modal matrix $\mathbf{\Phi}$ as

$$\mathbf{M}_{ROM}\ddot{\mathbf{q}} + \mathbf{C}_{ROM}\dot{\mathbf{q}} + \mathbf{K}_{ROM}\mathbf{q} = \mathbf{0}, \tag{2.2}$$

where

$$\mathbf{M}_{ROM} = \mathbf{\Phi}^T\mathbf{M}\mathbf{\Phi},\ \ \mathbf{C}_{ROM} = \mathbf{\Phi}^T\mathbf{C}\mathbf{\Phi},\ \ \mathbf{K}_{ROM} = \mathbf{\Phi}^T\mathbf{K}\mathbf{\Phi}, \tag{2.3}$$

and

$$\mathbf{x} = \mathbf{\Phi}\mathbf{q}. \tag{2.4}$$

Next, multi-physics ROMs are designed to suit systems/devices with potential EMS coupling phenomena. The electromagnetic (EM) forces $\mathbf{f}$ experienced by EM devices are modeled as generalized modal forces that are added to the structural ROM to obtain

$$\mathbf{M}_{ROM}\ddot{\mathbf{q}} + \mathbf{C}_{ROM}\dot{\mathbf{q}} + \mathbf{K}_{ROM}\mathbf{q} = \mathbf{f}. \tag{2.5}$$

It should be noted that EM forces are dependent on current, magnetic flux, and structural deformations. In this sense, the ROM can be written as

$$\mathbf{M}_{ROM}\ddot{\mathbf{q}} + \mathbf{C}_{ROM}\dot{\mathbf{q}} + \mathbf{K}_{ROM}\mathbf{q} = \mathbf{f}\big(\mathbf{q}, \mathbf{y}(t)\big), \tag{2.6}$$

where $\mathbf{y}(t)$ accounts for the current applied to system (and the flux). The electromagnetic force is typically nonlinear with respect to modal displacements. Thus, Eq. (2.6) represents the multi-physics ROM with nonlinear electromagnetic force. For structural vibrations with small displacements, this force can be linearized with respect to modal displacements. Linearizing the force, the following equation is obtained

$$\mathbf{f}\big(\mathbf{q}, \mathbf{y}(t)\big) = \mathbf{f}\big(\mathbf{0}, \mathbf{y}(t)\big) + \mathbf{K}_e\big(\mathbf{y}(t)\big)\mathbf{q} + \text{H.O.T.}, \tag{2.7}$$

where H.O.T. refers to higher order terms in $\mathbf{q}$. By excluding these higher-order terms, the EM force can be approximated by finding the modal EM force and stiffness at equilibrium. Let $\mathbf{f}_0(t) = \mathbf{f}\big(\mathbf{0}, \mathbf{y}(t)\big)$ and $\mathbf{K}_e(t) = \mathbf{K}_e\big(\mathbf{y}(t)\big)$. Then, the equation of motion for the multi-physics ROM with linearized electromagnetic force is given as

$$\mathbf{M}_{ROM}\ddot{\mathbf{q}} + \mathbf{C}_{ROM}\dot{\mathbf{q}} + \mathbf{K}_{ROM}\mathbf{q} = \mathbf{f}_0(t) + \mathbf{K}_e(t)\mathbf{q}. \tag{2.8}$$

Evaluating the EM force is key to capturing accurately the EMS coupling. For a multi-physics ROM with a linearized force, this is equivalent to determining the modal EM stiffness $\mathbf{K}_e(t)$. Moreover, this term is time dependent and usually periodic because of the periodic nature of the current input and/or operations of the EM system. Thus, building a multi-physics ROM necessitates an approach for evaluating the modal EM force $\mathbf{f}_0(t)$ and stiffness $\mathbf{K}_e(t)$ at zero structural deformation. In this study, the co-energy method is applied to evaluate $\mathbf{f}_0(t)$ and $\mathbf{K}_e(t)$ for the ROM with linearized force, and $\mathbf{f}\big(\mathbf{q}, t\big)$ for the ROM with nonlinear force.

2.2 Modal EM Force and Stiffness Calculation

The co-energy method is an alternative to the Maxwell stress tensor method for determining EM forces. The primary advantage of the co-energy method over the Maxwell stress tensor method is that for FEA models, a spatial finite difference along the mesh is not required. In this study, the multi-physic ROM is built directly in the modal space. To compute the modal EM forces and stiffness in the modal space using the Maxwell stress tensor, the EM force distributions are found first. Then, these forces are projected onto the modal space to obtain the modal EM forces. The same process is repeated at multiple magnitudes of modal displacements in order to find the modal EM stiffness. In contrast, with the co-energy method, the co-energy is determined at multiple magnitudes of modal displacement to compute both the modal EM forces and stiffness.

The co-energy of an EM system can be expressed as

$$W'(\mathbf{q}, \mathbf{y}) = \int\limits_{V} \int\limits_{\mathbf{H}} \mathbf{B}(\mathbf{H}) \cdot \mathrm{d}\mathbf{H}\mathrm{d}V, \tag{2.9}$$

where $\mathbf{B}(\mathbf{q}, \mathbf{y})$ and $\mathbf{H}(\mathbf{q}, \mathbf{y})$ are the magnetic flux density and magnetic field, respectively. The displacement $\mathbf{q} = [q_1, q_2, \ldots, q_n]^T$. In the modal space, the modal EM force and stiffness for mode k can be expressed as

$$f_k(t) = \left.\frac{\partial W'}{\partial q_k}\right|_{\mathbf{q}=\mathbf{0}}, \quad k = 1, 2, \ldots, n \tag{2.10}$$

$$\mathbf{K}_e(t) = \left.\begin{bmatrix} \frac{\partial f_1}{\partial q_1} & \cdots & \frac{\partial f_1}{\partial q_n} \\ \vdots & \ddots & \vdots \\ \frac{\partial f_n}{\partial q_1} & \cdots & \frac{\partial f_n}{\partial q_n} \end{bmatrix}\right|_{\mathbf{q}=\mathbf{0}} = \left.\begin{bmatrix} \frac{\partial^2 W'}{\partial q_1^2} & \cdots & \frac{\partial^2 W'}{\partial q_1 q_n} \\ \vdots & \ddots & \vdots \\ \frac{\partial^2 W'}{\partial q_1 q_n} & \cdots & \frac{\partial^2 W'}{\partial q_n^2} \end{bmatrix}\right|_{\mathbf{q}=\mathbf{0}} \tag{2.11}$$

It should be noted that a numerical approximation for the first and second order derivatives of the co-energy is required. The finite difference approximations can be expressed as

$$f_{0,i} = \frac{W'(\Delta\mathbf{q_i}) - W'(-\Delta\mathbf{q_i})}{2\Delta q_i}, \tag{2.12}$$

$$K_{e,ii} = \frac{W'(\Delta\mathbf{q_i}) + W'(-\Delta\mathbf{q_i}) - 2W'(\mathbf{0})}{\Delta q_i^2}, \tag{2.13}$$

$$K_{e,ij} = \frac{W'(\Delta\mathbf{q_{i,j}}) + W'(\mathbf{0}) - W'(\Delta\mathbf{q_i}) - W'(\Delta\mathbf{q_j})}{\Delta q_i \Delta q_j}, \tag{2.14}$$

where

$$\Delta\mathbf{q_i} = [0, \ldots, 0, \Delta q_i, 0, \ldots, 0]^T, \tag{2.15}$$

$$\Delta\mathbf{q_{i,j}} = [0, \ldots, 0, \Delta q_i, 0, \ldots, 0, \Delta q_j, 0, \ldots, 0]^T, \tag{2.16}$$

where Δq_i is a small perturbation in q_i at $q_i = 0$. The indices $i, j = 1, 2, \ldots, n$.

By choosing an 8-pole AC synchronous electric machine as an example, the resulting modal EM stiffness matrix of the stator is shown in Fig. 2.1.

The matrix is diagonally dominant and time-dependent. Consider, for example that the electric machine is rotating at a constant angular velocity; thus, the rotor angle is proportional to time. Figure 2.2 illustrates the diagonal terms of $\mathbf{K}_e(t)$ with respect to the rotor angle.

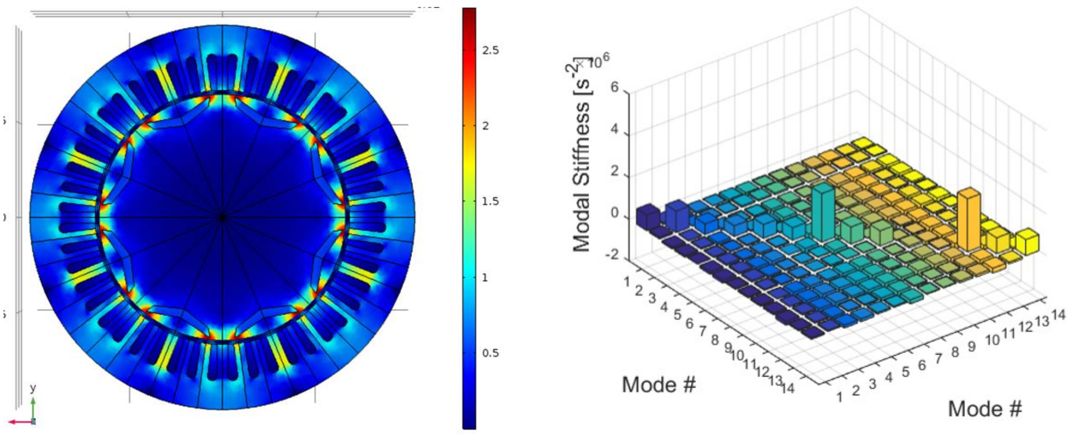

(a) (b)

Figure 2.1: 8 pole AC machine (left) and $\mathbf{K}_e(t)$ matrix at one time instant (right). Such matrix is diagonally dominant.

For an 8-pole synchronous machines, $\mathbf{K}_e$ is periodic with respect to rotor angle and the period is $2\pi/8$ at a constant rotor angular velocity. The periodicity of $\mathbf{K}_e$ with respect to time may cause unexpected resonances and system performance issues, as discussed next.

2.3 Stability of the EMS System under Parametric Excitation

The projection of equations of motion onto the structural modal space reduces the model order and simultaneously decouples the structural equations. For the structure-only model, the mass and stiffness matrices are diagonal in the modal space. However, for the multi-physics ROM, the EM stiffness matrix is not completely diagonal. However, the EM stiffness matrix is still diagonally dominant, even for structures with high modal density. Therefore, the analysis of a single mode is necessary to understand the stability of the system. The stability of multi-physics ROM with linearized EM forces is discussed in this section. The equation of motion for a single mode is

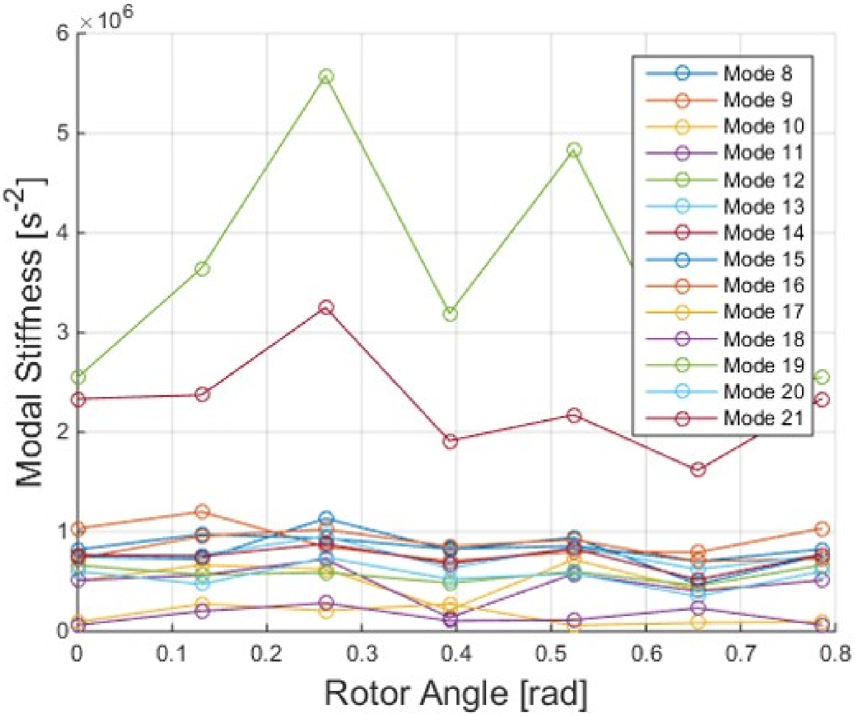

Figure 2.2: The diagonal terms are shown relative to the rotor angle at constant rotor angular velocity. Periodicity holds, as expected.

expressed as

$$m_{ROM}\ddot{q} + c_{ROM}\dot{q} + k_{ROM}q = f_0(t) + k_e(t)q. \tag{2.17}$$

The periodic EM force and stiffness can be expressed as a Fourier series in time as

$$f_0(t) = f_{0,s} + \sum_{n=1}^{\infty} f_{n,v}\cos(n\omega t), \tag{2.18}$$

$$k_e(t) = k_0 + \sum_{n=1}^{\infty} k_n\cos(n\omega t), \tag{2.19}$$

where ω is the fundamental frequency. In cases where the fundamental frequency is dominant, one can approximate $f_0(t)$ and $k_e(t)$ as

$$f_0(t) = f_{0,s} + f_{0,v}\cos(\omega t), \tag{2.20}$$

$$k_e(t) = k_0 + k_1\cos(\omega t). \tag{2.21}$$

For studying the stability of the structure under parametric excitation, the force $f_0(t)$ is omitted. Thus, Eq. 2.17 becomes

$$\frac{\mathrm{d}^2 q}{\mathrm{d}\tau^2} + \frac{c_{ROM}}{m_{ROM}\omega}\frac{\mathrm{d}q}{\mathrm{d}\tau} + \left(\frac{k_{ROM} - k_0}{m_{ROM}\omega^2} - \frac{k_1}{m_{ROM}\omega^2}\cos\tau\right)q = 0, \tag{2.22}$$

where $\tau = \omega t$. Note that $m_{ROM} = 1$ for a mass-normalized system. Thus, the equation of motion can be simplified to

$$\frac{\mathrm{d}^2 q}{\mathrm{d}\tau^2} + \frac{c_{ROM}}{\omega}\frac{\mathrm{d}q}{\mathrm{d}\tau} + \left(\frac{k_{ROM} - k_0}{\omega^2} - \frac{k_1}{\omega^2}\cos\tau\right)q = 0. \tag{2.23}$$

This equation is in the form of damped Mathieu's equation [102], namely

$$\frac{\mathrm{d}^2 x}{\mathrm{d}t^2} + c\frac{\mathrm{d}x}{\mathrm{d}t} + (\delta + \epsilon\cos t)x = 0. \tag{2.24}$$

A system governed by Eq. (2.24) becomes unstable once the amplitude of parametric excitation ϵ is large enough. The threshold value of ϵ is a function of δ. The stability transition curve in the neighbourhood of $\delta = 1/4$ is expressed as

$$\delta = \frac{1}{4} \pm \frac{\sqrt{\epsilon^2 - c^2}}{2}. \tag{2.25}$$

To explore the theoretical stability transition stiffness, the model of a dynamical system described by Eq. (2.23) is examined. When the parametric excitation frequency is twice that of the natural frequency of the structure, the transition stiffness is $k_{1,t} = 2c_{ROM}\omega_n$. In this study, the damping is determined by selecting the damping

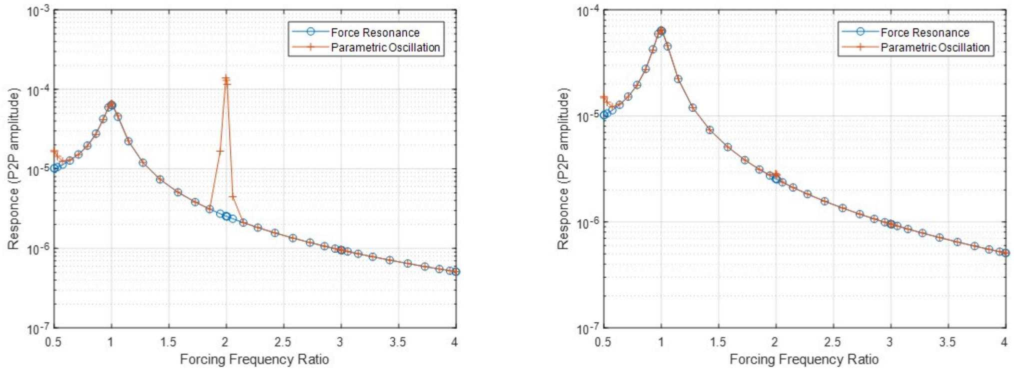

(a)

(b)

Figure 2.3: (a) Observed parametric resonance when amplitude of parametric excitation is 10% higher than the transition stiffness.(b) Parametric resonance was not triggered when amplitude of parametric excitation is 10% lower than the transition stiffness.

ratio. Thus, $c_{ROM} = 2\zeta\sqrt{k_{ROM}}$. The transition stiffness is expressed as

$$k_{1,t} = 4\zeta k_{ROM}, \tag{2.26}$$

where ζ is the damping ratio of the structure. Two k_1 values were selected, $0.9k_{1,t}$ and $1.1k_{1,t}$. In both cases, the (peak-to-peak) amplitude of the steady state response was evaluated using time marching simulation over the frequency range, both with and without the parametric excitation term $\frac{k_1}{\omega^2}\cos\tau$. The response showed that a parametric resonance peak was obtained when $k_1 = 1.1k_{1,t}$, which is slightly higher than the transition stiffness in Fig. 2.3. In contrast, that peak was not observed when $k_1 = 0.9k_{1,t}$, as shown in Fig. 2.3. In these plots, the horizontal axis represents the ratio between frequency of force harmonics and the natural frequency. The parametric excitation frequency is the same as the frequency of force.

2.4 Proof-of-Concept Device

In this study, a proof-of-concept device is considered to demonstrate the EMS phenomena by applying the multi-physics ROM. The device is a laminated soft iron core with coil to support AC current, as shown in Fig. 2.4. The upper arm is allowed to deform and vibrate, while the other portions of the core are fixed. The electromagnetic force is periodic when the input is a periodic AC current. Thus, both the force and the parametric excitation frequencies are dependent on the frequency of AC current. Table 2.1 shows the properties of the device. In this table, the notations I and N represent the amplitude of the AC current and the number of turns in the coil, respectively.

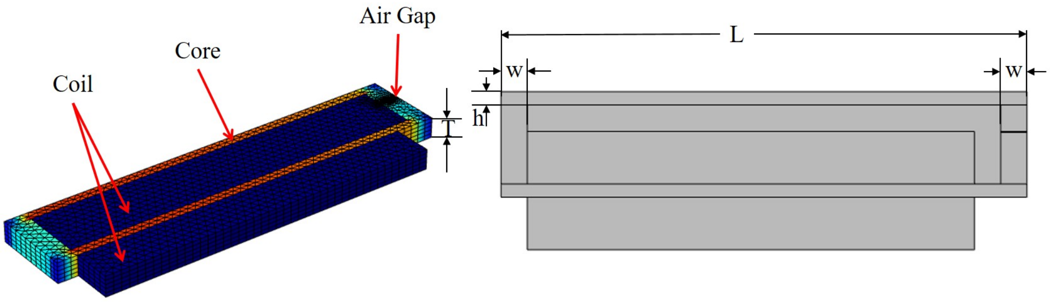

Figure 2.4: Magnetic flux and geometry plot for the proof-of-concept device.

Table 2.1: Parameters of the Proof-of-Concept Device

L	0.20 m
w	0.01 m
T	0.01 m
h	0.005 m
I	2.0 A
N	150

2.4.1 Construction of Multi-Physics ROMs

A high fidelity FEA model is constructed first. Then structural parameters and electromagnetic forces are determined. Their quantities are necessary for constructing the multi-physics ROM for the proof-of-concept device.

2.4.1.1 Construction of Multi-Physics ROMs with Linearized EM Forces

The construction of multi-physics ROMs force involves creating first a model for the EM forces and stiffness using the co-energy method. The advantage of using the co-energy method is that only static EM analyses are needed using the full-fidelity FEA model. The co-energy of the device depends on the modal displacement and the current. For calculating the linearized EM force, the co-energy of the device is computed under different current values. By perturbing the magnitude of the modal displacement, the EM force and stiffness at all current values can be determined using Eqs. (2.12) to (2.14). Thus, the EM force and stiffness are obtained as functions of the current. The current input is a function of time. Thus, the EM force and stiffness can be determined as functions of time. The amplitudes of the EM force and stiffness for the first mode of the device and the stability transition stiffness when damping ratio $\zeta = 0.045$ are listed in Tab. 2.2. These results of EM forces and stiffness suggest that the amplitude of parametric excitation k_1 is larger than the transition stiffness k_t for the selected mode. The current input in these calculations is harmonic with an amplitude of $I = 2A$ as shown in Tab. 2.1.

Table 2.2: FEA Results

$f_{0,v}$	8.87 [mkg$^{1/2}$s^{-2}]
k_t	8.52×10^4[s^{-2}]
k_1	9.32×10^4 [s^{-2}]

The EM force f_0 and stiffness k_e depend on the current. The current depends on time, which makes f_0 and k_e depend on time. The corresponding FEA results for $f_0(t)$ and $k_e(t)$ are shown in Fig. 2.5. These results show that the modal EM force and stiffness are both quadratic functions of current for this design. They are therefore

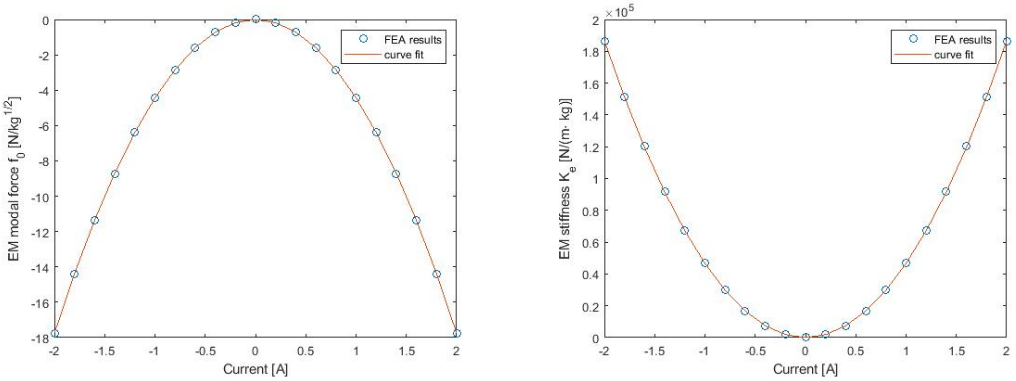

(a) (b)

Figure 2.5: (a) Modal EM force is a quadratic function of current. (b) Model EM stiffness is a quadratic function of current.

approximated as

$$\begin{aligned} f_0(t) &= a_f i(t)^2, \\ k_e(t) &= a_k i(t)^2, \end{aligned} \tag{2.27}$$

where $i(t)$ is the current, and parameters a_f and a_k are determined using regression. Note that the quadratic relationship holds because the magnetic material is not saturated. Therefore, the quadratic relation is valid only for a limited range of current values. With the expressions for the modal EM force and stiffness found, the multi-physics ROM with linearized force is expressed as

$$m_{ROM}\ddot{q} + c_{ROM}\dot{q} + (k_{ROM} - a_k i(t)^2)q = a_f i(t)^2. \tag{2.28}$$

2.4.1.2 Construction of Multi-Physics ROMs with Nonlinear EM Forces

Building ROMs with nonlinear EM forces requires finding the EM forces as a function of both the current and the modal displacement. Assume that the modal displacement is small such that the change of air gap thickness is the result of displacement in an EMS model. An analytic study results in an expression of the total co-energy within the device in the form.

$$W' \cong \frac{\beta h\big(i(t)\big)}{(\alpha q+1)^2}, \tag{2.29}$$

where h is the magnetic field as a function of current, α and β are constant coefficients that need to be determined, and q is the modal displacement of the selected mode. The values of α and β are mode dependent.

This is a generalized expression, which is applicable to both linear and nonlinear magnetic materials. The FEA results for the device suggest that the magnetic material was not saturated, which means that such material can be treated as linear magnetic material. Thus, the co-energy can be expressed as function of the modal displacement

$$W' \cong \frac{\gamma i^2(t)}{(\alpha q+1)^2}, \tag{2.30}$$

where γ is a constant value that can be determined using FEA analysis. Taking the derivative of W' with respect to the modal displacement q, the modal force is expressed as

$$f \cong -\frac{2\alpha\gamma i^2(t)}{(\alpha q+1)^3}. \tag{2.31}$$

The multi-physics ROM with nonlinear force can thus be expressed as

$$m_{ROM}\ddot{q} + c_{ROM}\dot{q} + k_{ROM}q = -\frac{2\alpha\gamma i^2(t)}{(\alpha q+1)^3}. \tag{2.32}$$

Parameters α and γ are required to complete building the ROM. These parameters are calculated using the high-fidelity FEA model as follows. The co-energy of the device is computed at various values of the modal displacement and current as shown in Fig.. A function approximation given by Eq. (2.31) is obtained by using the high0fidelity calculations. The errors in the approximation of the co-energy and force in Eq. (2.31) are acceptable, as shown in Fig. 2.6.

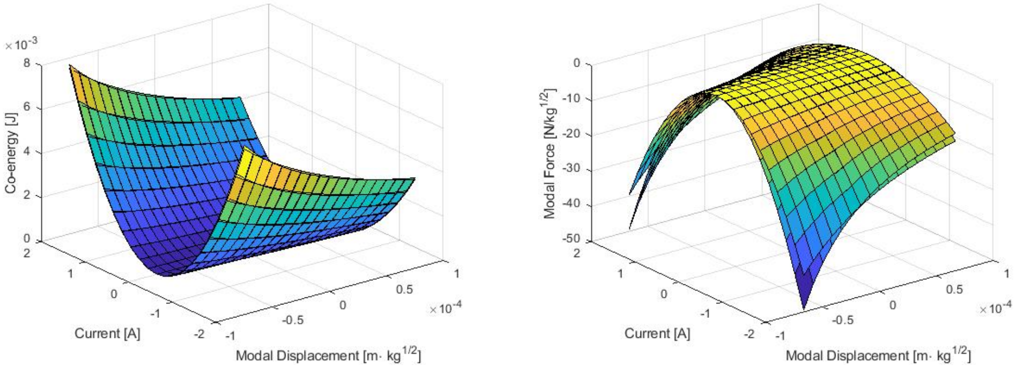

(a) (b)

Figure 2.6: (a) Co-energy approximation illustrates high accuracy. (b) EM force approximation yield acceptable accuracy.

2.4.2 Parametric Resonance

We performed a frequency domain study of the response of the device using the multi-physics ROM to verify the stability of the proof-of-concept device. A transient analysis was performed until the system settled onto a periodic behavior. By considering a single mode, namely the first mode of the upper arm of the device, the multi-physics ROM has a single structural degree of freedom.

2.4.3 Response of ROM with Linearized EM Forces

The stiffness k_{ROM} was obtained from the results of FEA, and the damping ratio was first set to $\zeta = 0.045$. For a harmonic current, the quadratic relationship between k_e and current ensures that k_e is harmonic plus a constant, with a frequency that is twice that of the AC current. As stated earlier, the parametric resonance occurs when the parametric excitation frequency is twice the natural frequency. Therefore, for this design, the parametric resonance occurs when the current frequency is close to the natural frequency.

Results of a time dependent analysis of the multi-physics ROM are shown in Fig. 2.7. Symbols + represent the frequency domain response from the model without

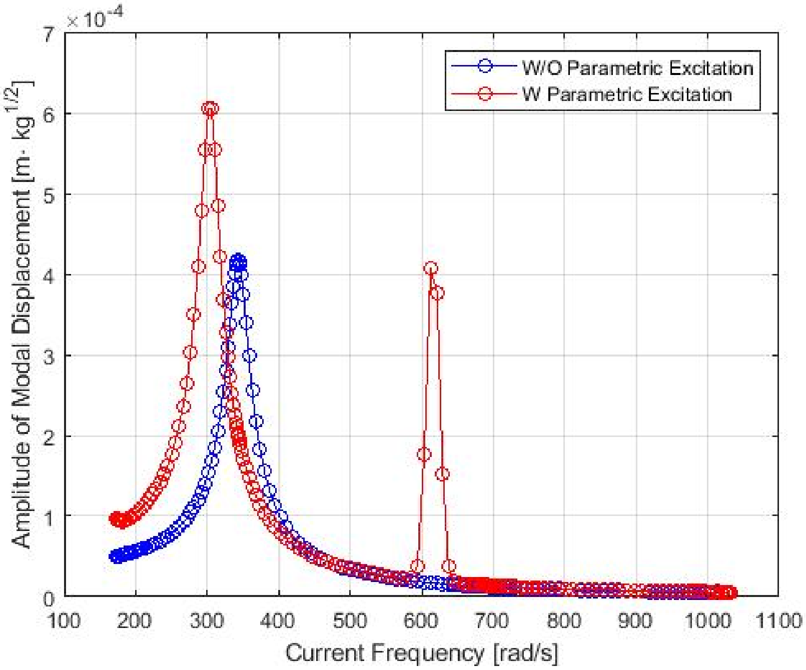

Figure 2.7: Frequency domain response at $\zeta = 0.045$ shows peak amplification and shift of normal resonance and appearance of parametric resonance peak.

k_e. Circles indicate the response from the system with parametric excitation, i.e. with k_e. With parametric excitation, a new peak appears slightly before the current frequency reaches the natural frequency. This peak represents a parametric resonance. The peak exists because the amplitude of the parametric excitation is higher than the stability transition stiffness. The other peak of the usual resonance shifts slightly to the left. This can be attributed to the non-zero mean of the modal EM stiffness. As shown in Eq. (2.23), the constant k_0 component of k_e is subtracted from the structural model stiffness, which results in a shift in the usual resonance. In addition, the usual resonance peak is higher in the presence of parametric excitation.

Results in Fig. 2.7 were obtained for $\zeta = 0.045$. The value of the damping ratio affects the system responses as shown in Fig. 2.8. These results show that the parametric resonance is sensitive to the damping ratio.

2.4.4 Response of ROM with Nonlinear EM Forces

The nonlinear EM force is stiffening with respect to modal displacement. Thus, an amplification of the response is expected. Thus, a smaller amplitude of current was selected to avoid instability. With the damping ratio $\zeta = 0.02$ and an amplitude $I = 1.2A$ of the current, the frequency domain response of nonlinear ROM is shown in Fig. 2.9. In this plot, the response of the ROM with linearized EM force under the selected damping and current is shown for comparison. A zoomed-in version of the frequency response near the parametric resonance frequency shows the existence of a parametric resonance peak.

The resonance peak caused by force harmonics is amplified and shifted for system responses with EMS coupling, for both linearized and nonlinear EM forces. While the amount of frequency shift is the same for linear and nonlinear model, the amplification is stronger with a nonlinear EM force. Nonlinearity amplifies the force compared to its linear prediction. The peak-to-peak amplitude of nonlinear force in frequency domain is shown in Fig. 2.10. Note that the amplitude of EM force with EMS coupling is higher than that without EMS coupling. The amplitude of the nonlinear EM force is higher than the linearized EM force.

2.4.5 FEA Verification of ROM Simulation Results

The results obtained from time marchings using the multi-physics ROM were verified using time domain analysis (TDA) on the FEA model. Two scenarios are designed for this verification process. One is the verification of the resonance caused by force harmonics without EMS coupling. The other is the verification of the response to displacement-dependent EM forces. A harmonic AC current in the coil is the input to the system for both scenarios. A comparison of frequency domain responses using FEA model and multi-physics ROM are shown in Figs. 2.11 and 2.12.

In the first scenario, the FEA verification is done for the case without EMS coupling. The residual between the FEA and ROM results is approximately 4.3%. This residual is expressed as $r = \frac{||\mathbf{D}_{ROM} - \mathbf{D}_{FEA}||_2}{||\mathbf{D}_{FEA}||_2}$, where $\mathbf{D}_{ROM}$ and $\mathbf{D}_{FEA}$ are the vectors of amplitudes of modal displacement frequency domain responses using ROM and transient analysis of FEA, respectively. The frequencies in these vectors are the frequencies used in FEA verification.

In the second scenario, the EM force is determined at each instant, as the structure deforms and vibrates. Thus, the physical displacement of vertices, especially the FEA vertices at both edges of the air gap, are limited by the geometry of the structure. The amplitude of the current for the second scenario is selected so that the displacement of these vertices does not exceed the geometric limits. The residual between FEA and ROM results at these critical frequencies is approximately 12.8%. The computational times required to find the frequency domain responses for the ROM and the FEA approaches is listed below in Tab. 2.3.

Table 2.3: Comparison of Computational Time at a Single Frequency

Method	Value
ROM without EMS Coupling	30.7 [ms]
ROM with Linearized EM Force	31.0 [ms]
ROM with Nonlinear EM Force	953 [ms]
FEA with EMS Coupling	∼4 [hr]

The FEA time-domain analysis is computationally expensive. The computation time shown in Tab. 2.3 for FEA simulation is for the response of one frequency only, which is much higher than the time for the ROM. These two verification scenarios demonstrate the computational accuracy and efficiency for the proposed ROM.

2.5 Conclusions

Eletromagnetic-structural (EMS) phenomena are caused by the coupling of structural deformation and distributed electromagnetic forces in electromagnetic devices. However, previous studies, especially those focused on electric machines, did not adequately model EMS coupling phenomena. This study demonstrates that coupling can lead to excitation of specific structural resonances, such as parametric resonances. In addition, multi-physics ROMs that capture the EMS coupling between structural vibration and electromagnetic forces was presented. A proof-of-concept electric device was proposed, and a multi-physics ROM was constructed for the device. The ROM was shown to capture the system response in the frequency domain, including the shift and amplification of the response caused by force harmonics and parametric resonances. Results suggest that the response is sensitive to structural parameters. The amplification of the force response and the appearance of parametric resonances are stronger for devices with lighter materials and smaller damping, which are preferred in high-performance electromagnetic products. The insights gained from the proposed EMS models can aid in the design of high performance EM devices.

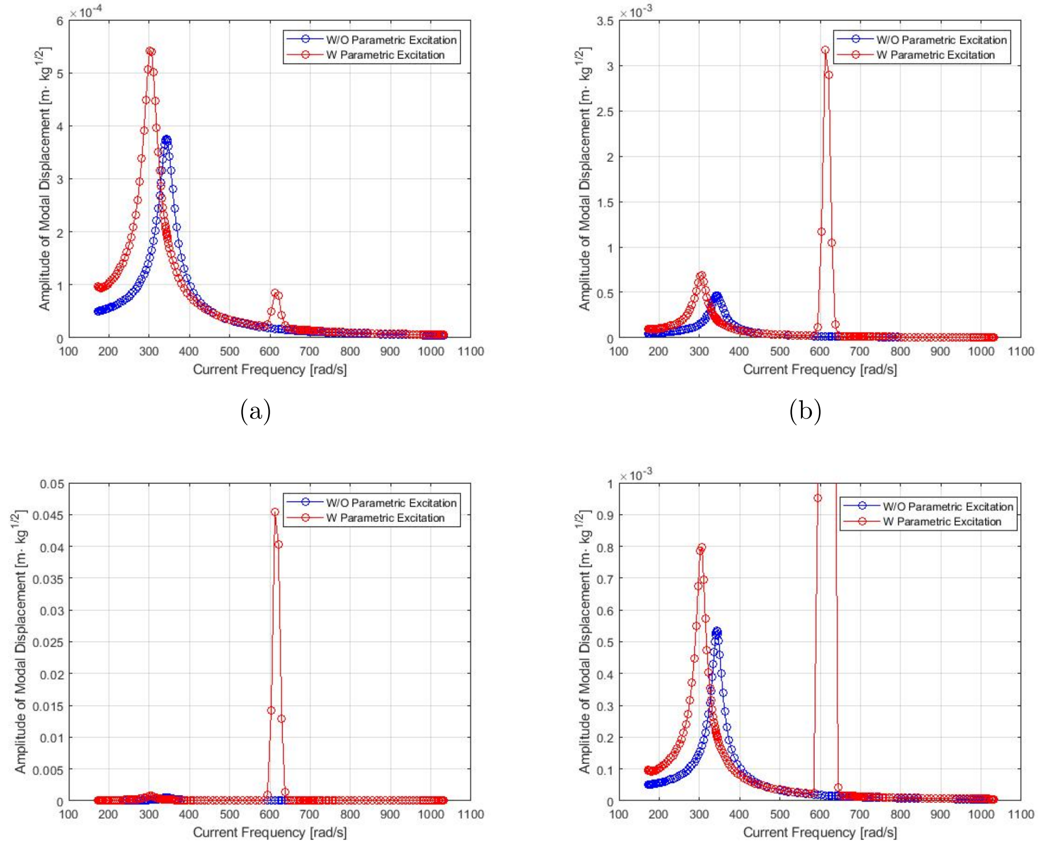

(a) (b)

(c) (d)

Figure 2.8: (a) Frequency domain response at $\zeta = 0.05$ shows peak amplification and shift of normal resonance and very small parametric resonance peak. (b) Frequency domain response at $\zeta = 0.04$ shows peak amplification and shift of normal resonance and high parametric resonance peak. (c) Frequency domain response at $\zeta = 0.035$ shows extremely high parametric resonance peak. (d) Zoomed in frequency domain response at $\zeta = 0.035$ shows peak amplification and shift of left resonance peak.

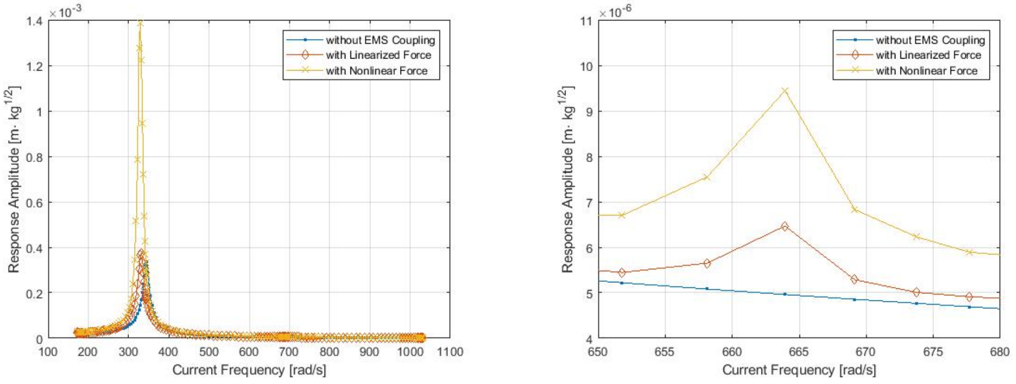

(a) (b)

Figure 2.9: (a) Frequency domain response of ROM with nonlinear force shows higher amplification of the resonance peak compared with ROM with linearized force, while the amounts of frequency shift are the same. (b) Zoomed frequency domain response shows the existence of parametric resonance peak for models with EMS coupling.

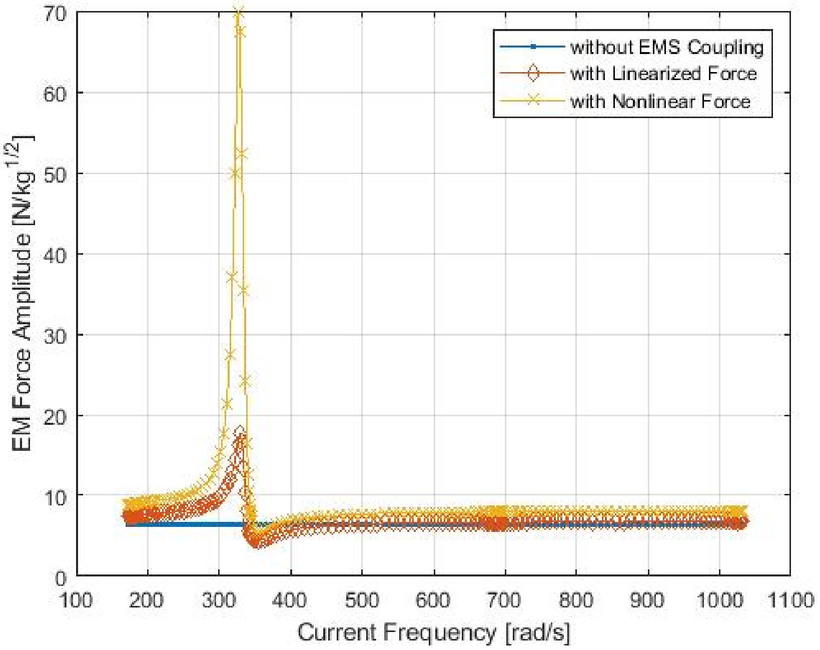

Figure 2.10: Amplitude of force with nonlinear force can reach as high as 9 times the amplitude of force without considering EMS coupling

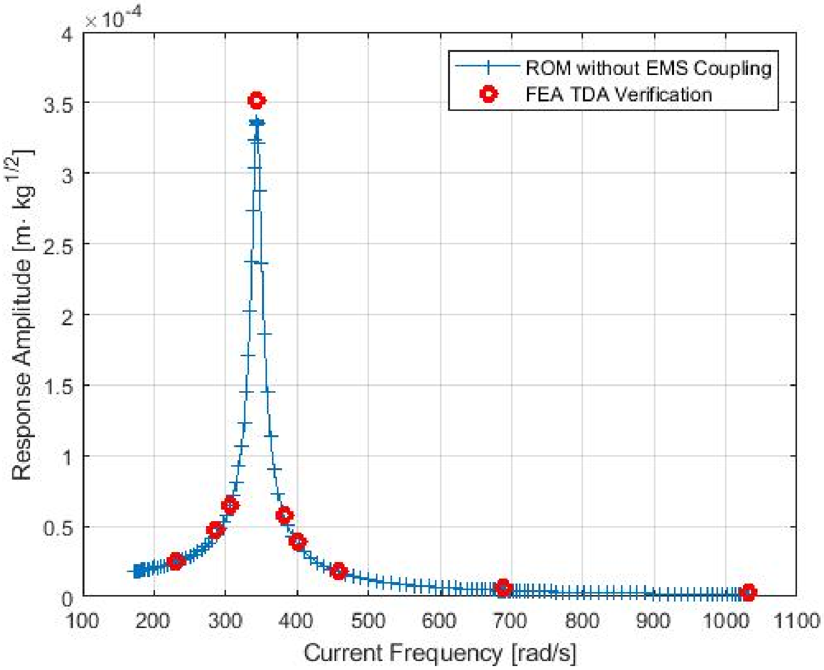

Figure 2.11: FEA results are matching the frequency domain response of the EM force without EMS coupling.

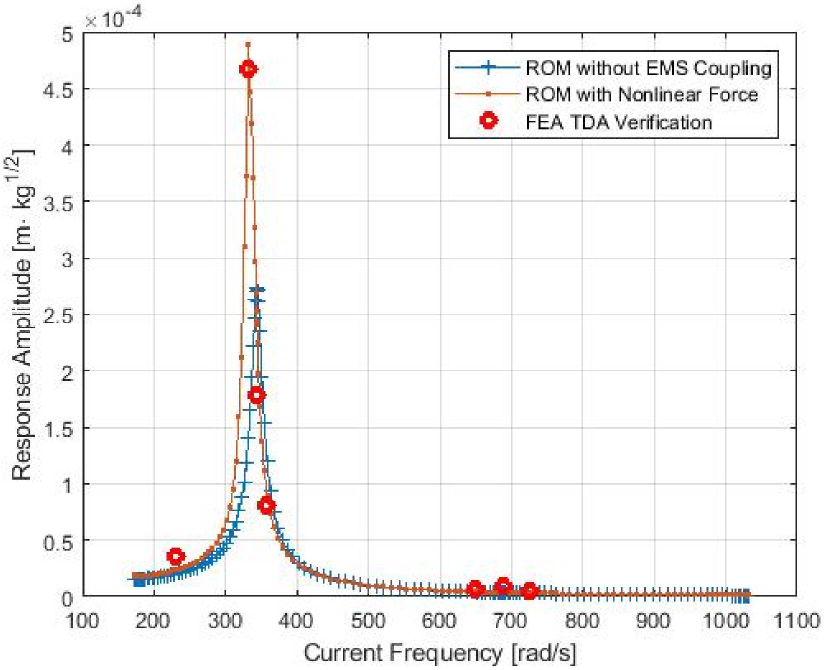

Figure 2.12: Residual between amplitude of response from FEA results and ROM results is below 13%

CHAPTER III

Novel Hybrid Electric Powertrain Architecture

3.1 Hybrid Powertrain Structure Overview

This section introduces the new hybrid powertrain architecture, including its structure and operating modes.

This hybrid powertrain system consists of an ICE, two electric machines (motors/generators) with their regulators, a battery, and necessary mechanical connections. Existing HEV powertrain designs typically use planetary gears and clutches [7]. However, planetary gears and clutches are not necessary in our design. This change sacrifices the multiple configuration possibilities, but enhances the reliability of the powertrain. The two electric machines are referred to as the A and B machines. The configuration of the powertrain is shown in Fig. 3.1. The ICE block is mounted on the frame of the vehicle. The crank shaft (rotor) of the ICE is connected to the A rotor. The A stator can rotate, and is connected to the B rotor, which is further connected to the wheels and may include a gear with a fixed ratio. The B stator is mounted on the vehicle frame.

The crank shaft angular velocity is denoted by ω_E and the angular velocity of the A rotor by ω_{AR}. When the shaft connecting the ICE and the A rotor is rigid, $\omega_{AR} = \omega_E$. The angular velocity of the A stator is denoted by ω_{AS} and the angular velocity of the B rotor is denoted by ω_B. When the shaft connecting the A rotor to

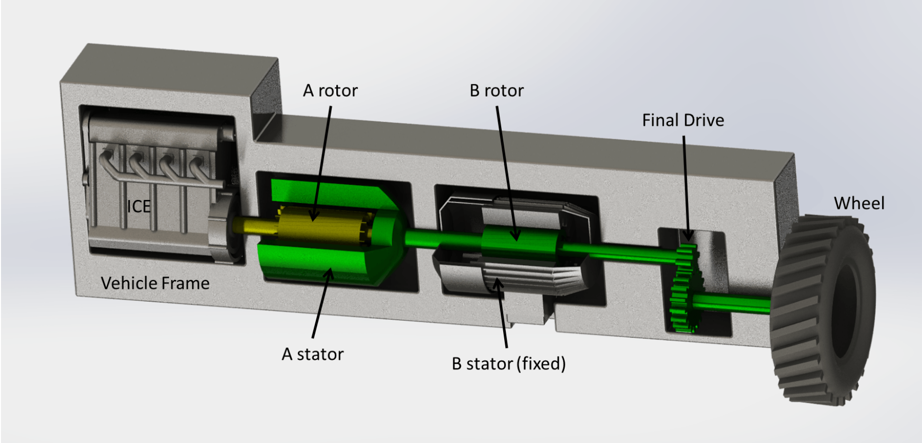

Figure 3.1: Structure of the novel powertrain showing the ICE, the A machine which has a rotating stator and the conventional B machine. The A machine controls the angular velocity transmitted to the wheels, and the B machine controls the torque transmitted to the wheel

the B rotor is rigid, $\omega_{AS} = \omega_B$. Also, the angular velocity of the rotating components which are upstream of the final drive but downstream of the B machine is denoted by ω_d. When the shaft connecting the B rotor to the final drive is rigid, $\omega_d = \omega_B$. The angular velocity of the wheels is denoted by ω_w. The final drive ratio can be expressed as $r_f = \omega_d/\omega_w$, and thus the vehicle speed is $v = r_w\omega_w = r_w(\omega_d/r_f)$, where r_w is the wheel radius.

Note that neither the stator nor the rotor of the A machine is fixed. The A rotor has an angular velocity of ω_{AR} whereas the A stator has an angular velocity of ω_{AS}. Thus, the A machine is able to provide a difference between the angular velocities ω_E of the crank shaft and the angular velocity ω_B of the B rotor. We refer to the relative angular velocity between the rotor and the stator of the A machine as the A angular velocity, and denote it by $\omega_A = \omega_{AR} - \omega_{AS}$. The angular velocity ω_A enables the A machine ultimately to regulate the angular velocity transferred to the B machine.

The B machine has the role of regulating the torque applied to the wheels. The B machine does not change the vehicle speed, but can regulate the torque applied to the wheels. Since the torque produced by the ICE has fluctuations, the B machine accomplishes two goals. First, it regulates the torque applied to the wheels by adding or subtracting from the average torque which comes from the ICE. Second, it suppresses the torque fluctuations that come from the ICE.

This new powertrain architecture resembles a series hybrid configuration, but the stator of the generator (corresponding to the stator of the A machine) is movable and connected to the rotor of the motor (corresponding to the rotor of the B machine). This change in configuration compared to series hybrid enables the split of power. It is possible for the power from the ICE to partially flow to the battery and partially to the wheels. However, the hybrid powertrain designed here is not a traditional power-split hybrid either. Neither a planetary gear nor a clutch is being used. The transmission function of this newly designed hybrid powertrain is referred to as an extended electronic continuously variable transmission (EECVT) system.

The EECVT system can accomplish many operation modes. A list of such modes is shown in Tab. 3.1. Note also that the new architecture allows the ICE to be used either at several operating points or just at a single optimal operating point. The operating points for the ICE can be chosen so that the power efficiency of the ICE is highest. Both the A and the B machines operate sometime in generator mode, and other times in motor mode. The freedom of operation for each device ensures multiple operation modes for the EECVT system.

The novel architecture has advantages, but it also has some drawbacks. The main drawback is the fact that it requires electrification of a rotating component. This can be addressed through the next generation of slip rings.

3.2 Vehicle-Level Model

To analyze the powertrain system, a model was developed and implemented in Matlab Simulink®. This section describes first the models of the different components which comprise the powertrain. Next, this section presents the system-level model

Table 3.1: Operation modes for the EECVT system (EV=electric vehicle mode)

ICE	**A Machine**	**B Machine**	**Operation Mode**
Off	Off	Motor	EV Mode Acceleration
Off	Off	Generator	EV Mode Acceleration
On	Motor	Motor	Power Boost High Speed
On	Motor	Generator	Battery Charging High Speed
On	Generator	Motor	Power Boost Low Speed
On	Generator	Generator	Battery Charging Low Speed

for the vehicle and powertrain dynamics, electric machines, battery, and ICE.

3.2.1 Powertrain Dynamics

To predict the vehicle dynamics, simplified models such as ones based on rigid bodies and lumped inertia/masses have been used in the literature [78]. We augment such models with elastic coupling elements to account for the elasticity of the mechanical couplings and shafts. Thus, we develop a system-level model which accounts for vibrations due to the flexibility of the shafts which connect the ICE to the A machine, the A machine to the B machine, and the B machine to the wheels.

Figure 3.2 shows the characteristics of the components modeled. Three flexible shafts are modeled with three torsional stiffnesses k_1, k_2, and k_3. The moments of inertia are modeled for the ICE crank shaft, the A rotor, the A stator, the B rotor, and the components downstream of the B rotor, including the wheels and the inertia of the vehicle. This results in a model with 5 degrees of freedom, namely: the angles of rotation θ_E of the ICE crank shaft, the angle of rotation θ_{AR} of the A rotor, the

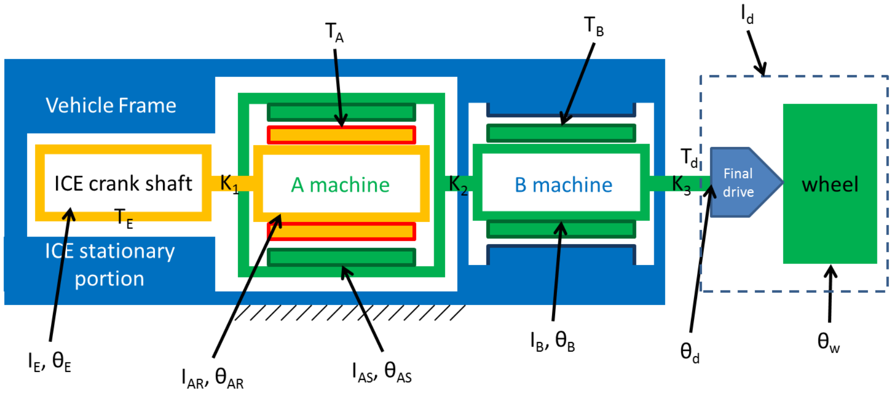

Figure 3.2: Structure of the novel powertrain showing the moments of inertia I_E, I_{AR}, I_{AS}, I_B, and I_W of the ICE rotating components, the A rotor, the A stator, the B rotor, and the rotating components downstream of the B machine, including the wheels and the effects of the vehicle mass. The angles of rotation and the torsional stiffnesses of the elastic elements are indicated also.

angle of rotation θ_{AS} of the A stator, the angle of rotation θ_B of the B rotor, and the angle of rotation θ_d of the components downstream of the B machine but before the final drive. Note that the elasticity in the final drive is not explicitly considered. Hence, the angle of rotation θ_w of the wheels is not a degree of freedom. Instead, θ_w is related to θ_d by the final drive ratio $\theta_w = \theta_d/r_f$. The equations of motion can be expressed as

$$\begin{aligned}
I_E\ddot{\theta}_E =& T_E - k_1(\theta_E - \theta_{AR}),\\
I_{AR}\ddot{\theta}_{AR} =& k_1(\theta_E - \theta_{AR}) + T_A,\\
I_{AS}\ddot{\theta}_{AS} =& -T_A - k_2(\theta_{AS} - \theta_B),\\
I_B\ddot{\theta}_B =& k_2(\theta_{AS} - \theta_B) + T_B - k_3(\theta_B - \theta_d),\\
I_d\ddot{\theta}_d =& k_3(\theta_B - \theta_d) - f m_v g \frac{1}{\eta_f}\left(\frac{r_w}{r_f}\right) - \frac{1}{2}\rho d A_F \ddot{\theta}_d^2 \frac{1}{\eta_f}\left(\frac{r_w}{r_f}\right)^3,
\end{aligned} \tag{3.1}$$

where I_E, I_{AR}, I_{AS}, I_B, and $I_d = \frac{6m_w + m_v}{\eta_f}(\frac{r_w}{r_f})^2$ are the moments of inertia of the ICE rotating components, the A rotor, the A stator, the B rotor, and the rotating components downstream of the B machine, including the wheels. The final drive ratio is r_f, and the final drive efficiency is η_f. The vehicle mass is m_v. The wheel mass is m_w and the wheel radius is r_w. T_E is the torque value created by the ICE. T_A and T_B are the electromagnetic torques created in the A machine and the B machine. In addition, resistive forces including aerodynamic drag and friction are included. f is the rolling resistance ratio, ρ is the density of air, d is the drag coefficient, A_F is the frontal area.

The first 4 relations in Eq. 3.1 are obtained easily for each of the corresponding components. The 5th relation is obtained by first accounting for the rolling motion of the wheels and the translation motion of the vehicle to obtain

$$\begin{aligned} 4\left(\frac{\left(\frac{1}{2}m_w r_w^2\right)\ddot{\theta}_w}{r_w} + m_w\dot{v}\right) + m_v\dot{v} &= F_w \\ &-f m_v g - \frac{1}{2}\rho d A_F v^2, \end{aligned} \tag{3.2}$$

where F_w is the forward drive force acting on the four wheels. Using $\dot{v} = r_w\ddot{\theta}_w$, one can transform Eq. 3.2 to obtain successively $4\left(\frac{1}{2}m_w\dot{v}+m_w\dot{v}\right)+m_v\dot{v} = F_w - f m_v g - \frac{1}{2}\rho d A_F v^2$ and

$$(6m_w + m_v)\dot{v} = F_w - f m_v g - \frac{1}{2}\rho d A_F v^2, \tag{3.3}$$

The force F_w is related to the torque T_w applied to the wheels by $F_w = T_w/r_w$. Also, the torque applied to the wheels is related to the torque T_d applied by the B rotor immediately upstream of the final drive by $T_w = r_f\eta_f T_d$. Thus, $F_w = r_f\eta_f T_d/r_w$. Moreover, the torque T_d is related to the elastic deformation of the shaft connecting the B rotor to the final drive by $T_d = k_3(\theta_B - \theta_d)$, so

$$\begin{aligned} F_w = \frac{r_f \eta_f T_d}{r_w} &= \frac{r_f \eta_f k_3(\theta_B - \theta_d)}{r_w} \\ &= \frac{r_f}{r_w} \eta_f k_3(\theta_B - \theta_d), \end{aligned} \tag{3.4}$$

Substituting F_w from Eq. 3.4 into Eq. 3.3, one obtains

$$\begin{aligned} (6m_w + m_v) r_w \ddot{\theta}_w &= \frac{r_f}{r_w} \eta_f k_3(\theta_B - \theta_d) \\ &\quad - f m_v g - \frac{1}{2} \rho d A_F (r_w \dot{\theta}_w)^2, \end{aligned} \tag{3.5}$$

Substituting $\theta_w = \theta_d / r_f$, one transforms Eq. 3.5 into

$$\begin{aligned} (6m_w + m_v) \frac{r_w}{r_f} \ddot{\theta}_d &= \frac{r_w}{r_f} \eta_f k_3(\theta_B - \theta_d) \\ &\quad - f m_v g - \frac{1}{2} \rho d A_F (\frac{r_w}{r_f} \dot{\theta}_d)^2, \end{aligned} \tag{3.6}$$

which leads to the 5th relation in Eq. 3.1 after algebraic manipulation.

A simpler model can be obtained by assuming [78] that the shafts connecting the ICE, and the A and B machines are very stiff (i.e., rigid). As a consequence, the torsional stiffnesses k_1, k_2, and k_3 are condidered infinite. The equations of motion are simplified to

$$
\begin{aligned}
\theta_E =& \theta_{AR}, \\
(I_E + I_{AR})\ddot{\theta}_E =& T_E + T_A, \\
\theta_{AS} =& \theta_B, \\
(I_{AS} + I_B + I_d)\ddot{\theta}_d =& T_B - T_A - f m_v g \frac{1}{\eta_f}\Big(\frac{r_w}{r_f}\Big) \\
& - \frac{1}{2}\rho d A_F \dot{\theta}_d^2 \frac{1}{\eta_f}\Big(\frac{r_w}{r_f}\Big)^3, \\
\theta_B =& \theta_d,
\end{aligned}
\tag{3.7}
$$

Thus, the simplified model has only 2 degrees of freedom (namely θ_E and θ_d) and two lumped inertias, namely $I_E + I_{AR}$ and $I_{AS} + I_B + I_d$.

3.2.2 Electric Machine Models

The two electric machines being chosen in the EECVT system are both surface-mounted permanent magnet (SMPM) machines [103]. SMPMs are one of the types of the alternating current permanent magnet synchronous machines (PMSM). In this work, each SMPM machine is modeled by governing equations, which is more accurate and distinct from look-up tables. The physics based models we use are more intensive computationally, but they are more accurate and are easier to modify automatically, which is beneficial for system optimization. Once the optimal system-level parameters are identified, lookup tables can be used for the two electric machines for faster vehicle-level simulations [150].

From a transfer function perspective, the model we use for each electric machine takes as input the voltage supplied by the battery and the torque command for that machine, and provides as output the actual electromagnetic torque and corresponding current. The model of each electric machine contains a field-oriented controller [14], power electronics and the electric machine itself. Direct current (DC) to alternative current (AC), three-phase to two-phase transforms [96] are applied for modeling each machine, which enables the connection between each AC electric machine and the battery (which, of course, is a DC power source). The parameters of the electric machine models are shown in Tab. 3.2.

Table 3.2: Parameters of the A and B electric machine models

Parameter	**Notation**	**Value**[unit]
Resistance	R_A and R_B	$0.08[\Omega]$
Direct Inductance	L_{Ad} and L_{Bd}	$0.2[mH]$
Quadrature Inductance	L_{Aq} and L_{Bq}	$0.2[mH]$
Rotor Flux Linkage	Λ_A and Λ_B	$0.1[Wb]$
Number of Poles	n_{Ap} and n_{Bp}	8

A field-oriented controller regulates the electromagnetic torque of each electric machine by regulating the direct currents i^r_{Ad} and i^r_{Bd}, and the quadrature currents i^r_{Aq} and i^r_{Bq} in a synchronous reference frame, namely the rotor reference frame for each machine. The commands of the i^r_{Aq} and i^r_{Bq} regulators are obtained from the torque requirements of the two electric machines T_{Ar} and T_{Br}. The command values of the quadrature currents $\tilde{i}^r_{Aq}$ and $\tilde{i}^r_{Bq}$ are proportional to T_{Ar} and T_{Br}, and are given by

$$\begin{gathered}\tilde{i}^r_{Aq} = \frac{T_{Ar}}{\frac{3}{4} n_{Ap} \hat{\Lambda}_A}, \tilde{i}^r_{Bq} = \frac{T_{Br}}{\frac{3}{4} n_{Bp} \hat{\Lambda}_B}, \\ \tilde{i}^r_{Ad} = 0, \tilde{i}^r_{Bd} = 0,\end{gathered} \tag{3.8}$$

where $\hat{\Lambda}_A$ and $\hat{\Lambda}_B$ are estimated rotor flux linkages, which for simplicity are considered equal to their exact values Λ_A and Λ_B. The command values of the direct currents $\tilde{i}^r_{Ad}$ and $\tilde{i}^r_{Bd}$ are set to zero to achieve minimum current operation.

The current regulators provide two-phase voltage commands $\tilde{v}^r_{Ad}$ and $\tilde{v}^r_{Bd}$, and $\tilde{v}^r_{Aq}$

and $\tilde{v}^r_{Bq}$ in the rotor reference frame of each machine. These voltages are converted into voltages $\tilde{v}_{Ad}$ and $\tilde{v}_{Bd}$, and $\tilde{v}_{Aq}$ and $\tilde{v}_{Bq}$ in the stator reference frame for each machine by using inverse Park transforms expressed as

$$\begin{aligned} \begin{bmatrix} \tilde{v}_{Ad} \\ \tilde{v}_{Aq} \end{bmatrix} &= \begin{bmatrix} \cos\theta^e_A & -\sin\theta^e_A \\ \sin\theta^e_A & \cos\theta^e_A \end{bmatrix} \begin{bmatrix} \tilde{v}^r_{Ad} \\ \tilde{v}^r_{Aq} \end{bmatrix}, \text{and} \\ \begin{bmatrix} \tilde{v}_{Bd} \\ \tilde{v}_{Bq} \end{bmatrix} &= \begin{bmatrix} \cos\theta^e_B & -\sin\theta^e_B \\ \sin\theta^e_B & \cos\theta^e_B \end{bmatrix} \begin{bmatrix} \tilde{v}^r_{Bd} \\ \tilde{v}^r_{Bq} \end{bmatrix}, \end{aligned} \tag{3.9}$$

where $\theta^e_A = \frac{1}{2} n_{Ap} \int_{\tau=0}^{t} \omega_A d\tau$ and $\theta^e_B = \frac{1}{2} n_{Bp} \int_{\tau=0}^{t} \omega_B d\tau$ are the electric field angles in the stator reference frame of each machine.

Next, the three-phase voltages needed are obtained. A pulse width modulation (PWM) technique referred to as space vector modulation is applied for voltage generation [103]. The two-phase duty cycles D_{Ad} and D_{Aq}, and D_{Bd} and D_{Bq} for the two electric machines, and the three-phase duty cycles D_{Aa}, D_{Ab}, and D_{Ac}, and D_{Ba}, D_{Bb}, and D_{Bc} are calculated for each electric machine using the space vector modulation from $\tilde{v}_{Ad}$ and $\tilde{v}_{Aq}$, and $\tilde{v}_{Bd}$ and $\tilde{v}_{Bq}$.

The space vector modulation technique for duty cycle calculation can be expressed for the A machine by first defining

$$D_{Ad} = \frac{\tilde{v}_{Ad}}{V_b}, D_{Aq} = \frac{\tilde{v}_{Aq}}{V_b}, \tag{3.10}$$

where V_b is the supply voltage, i.e. an output from the battery model in Eq. 3.24 (described in more detail in the next section).

When $D_{Aq} \geq 0$ and $D_{Ad} > D_{Aq}/\sqrt{3}$, or when $D_{Aq} \leq 0$ and $D_{Ad} < D_{Aq}/\sqrt{3}$ the values of D_{Aa}, D_{Ab}, and D_{Ac}, are obtained as

$$\begin{aligned}
D_{Aa} &= \frac{1}{2} + \frac{3}{4}D_{Ad} + \frac{\sqrt{3}}{4}D_{Aq}, \\
D_{Ab} &= \frac{1}{2} - \frac{3}{4}D_{Ad} + \frac{3\sqrt{3}}{4}D_{Aq}, \\
D_{Ac} &= \frac{1}{2} - \frac{3}{4}D_{Ad} - \frac{\sqrt{3}}{4}D_{Aq},
\end{aligned} \tag{3.11}$$

When $D_{Aq} \geq 0$ and $D_{Ad} < -D_{Aq}/\sqrt{3}$, or when $D_{Aq} \leq 0$ and $D_{Ad} > -D_{Aq}/\sqrt{3}$ the values of D_{Aa}, D_{Ab}, and D_{Ac}, are obtained as

$$\begin{aligned}
D_{Aa} &= \frac{1}{2} + \frac{3}{4}D_{Ad} - \frac{\sqrt{3}}{4}D_{Aq}, \\
D_{Ab} &= \frac{1}{2} - \frac{3}{4}D_{Ad} + \frac{\sqrt{3}}{4}D_{Aq}, \\
D_{Ac} &= \frac{1}{2} - \frac{3}{4}D_{Ad} - \frac{3\sqrt{3}}{4}D_{Aq},
\end{aligned} \tag{3.12}$$

Otherwise the values of D_{Aa}, D_{Ab}, and D_{Ac}, are obtained as

$$\begin{aligned}
D_{Aa} &= \frac{1}{2} + \frac{3}{2}D_{Ad}, \\
D_{Ab} &= \frac{1}{2} + \frac{\sqrt{3}}{2}D_{Aq}, \\
D_{Ac} &= \frac{1}{2} - \frac{\sqrt{3}}{2}D_{Aq},
\end{aligned} \tag{3.13}$$

For the B machine, one obtains similar three-phase duty cycles as those in Eqs. 3.11, 3.12 and 3.13 (omitted for the sake of brevity).

Half-bridge inverters use the duty cycles of each machine to generate three-phase voltages v_{Aa}, v_{Ab}, and v_{Ac} (for the A machine) and v_{Ba}, v_{Bb}, and v_{Bc} (for the B machine) which drive each electric machine

$$v_i = D_i V_b, \quad \text{where} \quad i = Aa, Ab, Ac, Ba, Bb, Bc, \tag{3.14}$$

The electric machines first transfer three-phase voltages v_{Aa}, v_{Ab}, and v_{Ac} (for the A machine) and v_{Ba}, v_{Bb}, and v_{Bc} (for the B machine) into two-phase voltages v_{Ad} and v_{Aq} (for the A machine) and v_{Bd} and v_{Bq} (for the B machine) in stator reference frames using

$$\begin{aligned} \begin{bmatrix} v_{Ad} \\ v_{Aq} \end{bmatrix} &= \begin{bmatrix} \frac{2}{3} & -\frac{1}{3} & -\frac{1}{3} \\ 0 & \frac{\sqrt{3}}{3} & -\frac{\sqrt{3}}{3} \end{bmatrix} \begin{bmatrix} v_{Aa} \\ v_{Ab} \\ v_{Ac} \end{bmatrix}, \\ \begin{bmatrix} v_{Bd} \\ v_{Bq} \end{bmatrix} &= \begin{bmatrix} \frac{2}{3} & -\frac{1}{3} & -\frac{1}{3} \\ 0 & \frac{\sqrt{3}}{3} & -\frac{\sqrt{3}}{3} \end{bmatrix} \begin{bmatrix} v_{Ba} \\ v_{Bb} \\ v_{Bc} \end{bmatrix}, \end{aligned} \tag{3.15}$$

The two-phase voltages are converted from stator reference frames into voltages v^r_{Ad} and v^r_{Aq} (for the A machine) and v^r_{Bd} and v^r_{Bq} (for the B machine) in rotor reference frames using Park transforms as

$$\begin{aligned} \begin{bmatrix} v^r_{Ad} \\ v^r_{Aq} \end{bmatrix} &= \begin{bmatrix} \cos\theta^e_A & \sin\theta^e_A \\ -\sin\theta^e_A & \cos\theta^e_A \end{bmatrix} \begin{bmatrix} v_{Ad} \\ v_{Aq} \end{bmatrix}, \\ \begin{bmatrix} v^r_{Bd} \\ v^r_{Bq} \end{bmatrix} &= \begin{bmatrix} \cos\theta^e_B & \sin\theta^e_B \\ -\sin\theta^e_B & \cos\theta^e_B \end{bmatrix} \begin{bmatrix} v_{Bd} \\ v_{Bq} \end{bmatrix}, \end{aligned} \tag{3.16}$$

The two-phase voltage-current relation for each machine in the rotor reference frame can be expressed as

$$\begin{aligned}
L_A \frac{d}{dt}\begin{bmatrix} i^r_{Ad} \\ i^r_{Aq} \end{bmatrix} &= \begin{bmatrix} -R_A & \omega^e_A L_A \\ -\omega^e_A L_A & -R_A \end{bmatrix}\begin{bmatrix} i^r_{Ad} \\ i^r_{Aq} \end{bmatrix} \\
&\quad + \begin{bmatrix} v^r_{Ad} \\ v^r_{Aq} \end{bmatrix} + \begin{bmatrix} 0 \\ -\omega^e_A \end{bmatrix}\Lambda_A, \\
L_B \frac{d}{dt}\begin{bmatrix} i^r_{Bd} \\ i^r_{Bq} \end{bmatrix} &= \begin{bmatrix} -R_B & \omega^e_B L_B \\ -\omega^e_B L_B & -R_B \end{bmatrix}\begin{bmatrix} i^r_{Bd} \\ i^r_{Bq} \end{bmatrix} \\
&\quad + \begin{bmatrix} v^r_{Bd} \\ v^r_{Bq} \end{bmatrix} + \begin{bmatrix} 0 \\ -\omega^e_B \end{bmatrix}\Lambda_B,
\end{aligned} \tag{3.17}$$

where $\omega^e_A = \frac{1}{2} n_{Ap}\omega_A$ and $\omega^e_B = \frac{1}{2} n_{Bp}\omega_B$ are the electric field angular velocities in the stator reference frame of each machine (i.e., time derivatives of θ^e_A and θ^e_B). Also, the two-phase voltages from Eq. 3.16 are used in Eq. 3.17. Note that parameters R_A, L_A, R_B and L_B are the resistances and inductances within each of the two the electric machines (Tab. 3.2), where the direct and quadrature inductances are considered to have the same values.

The two-phase currents i^r_{Ad} and i^r_{Aq} (for the A machine) and i^r_{Bd} and i^r_{Bq} (for the B machine) are used as inputs to four separate PI current regulators (two regulators for each machine), which close the loop with the command values of the direct and quadrature and currents $\tilde{i}^r_{Ad}$, $\tilde{i}^r_{Aq}$, and $\tilde{i}^r_{Bd}$, $\tilde{i}^r_{Bq}$ The gains of the 4 controllers are designed as

$$k^p_{Ad} = k^p_{Aq} = c_p R_A, k^p_{Bd} = k^p_{Bq} = c_p R_B, \tag{3.18}$$

$$
\begin{aligned}
k^i_{Ad} = k^i_{Aq} &= \frac{(k^p_{Ad} + R_A)^2}{c_i L_A}, \\
k^i_{Bd} = k^i_{Bq} &= \frac{(k^p_{Bd} + R_B)^2}{c_i L_B},
\end{aligned}
\tag{3.19}
$$

where superscript p indicates proportional gain, and superscript i indicates integral gain. The nondimensional coefficients c_p and c_i were chosen to obtain a good torque response (overshoot and time constant).

The torque generated by each of the two electric machines is proportional to corresponding quadrature current in the rotor frame as

$$
T_A = \frac{3}{4} n_{Ap} \Lambda_A i^r_{Aq}, T_B = \frac{3}{4} n_{Bp} \Lambda_B i^r_{Bq},
\tag{3.20}
$$

The battery model is connected to the models of the A and B electric machines by using the total power P_r required by both electric machines, which can be expressed as a sum of mechanical power output and loss due to electric resistance as

$$
\begin{aligned}
P_r = &\eta_A T_A \omega_A + ({i^r_{Aq}}^2 + {i^r_{Ad}}^2) R_A \\
&+ \eta_B T_B \omega_B + ({i^r_{Bq}}^2 + {i^r_{Bd}}^2) R_B,
\end{aligned}
\tag{3.21}
$$

where

$$
\begin{aligned}
\eta_A &= \begin{cases} 1+\eta_p, T_A\omega_A \geq 0 \\ 1-\eta_p, T_A\omega_A < 0 \end{cases}, \\
\eta_B &= \begin{cases} 1+\eta_p, T_B\omega_B \geq 0 \\ 1-\eta_p, T_B\omega_B < 0 \end{cases},
\end{aligned}
\tag{3.22}
$$

Here η_p is an efficiency penalty added to the model to capture otherwise unmodeled losses in the electric machines. The value of η_p was obtained by the following procedure. An efficiency map was generated for the electric machine models we use but with parameter values corresponding to an existing product, namely UQM PowerPhase 145 (and using the governing equations in this section). The difference between the efficiency map predicted by the model and the actual efficiency map for the product revealed a difference at the electric machine operating points shown by the dark areas in Fig. 3.3. Thus, a constant efficiency penalty is added to the electric machine model. The efficiency differences at these operating points can be observed between these two efficiency maps. As the results show, the average efficiency difference is less than 5%. We choose a more conservative value of 5% as a worst-case estimation so that our fuel economy estimates are lower. Note that the use of a constant efficiency penalty is a conventional estimation approach for electric machines. Thus, the efficiency penalty $\eta_p = 5\%$ was used to compute the power requirements for the electric machines.

Look-up tables with experimental data are not used because the model is designed not only for simulation of one powertrain realization, but also for system-level optimization. Hence, all aspects of the model are physics-based and parameterized to allow the components in the powertrain to be easily re-sized during optimization.

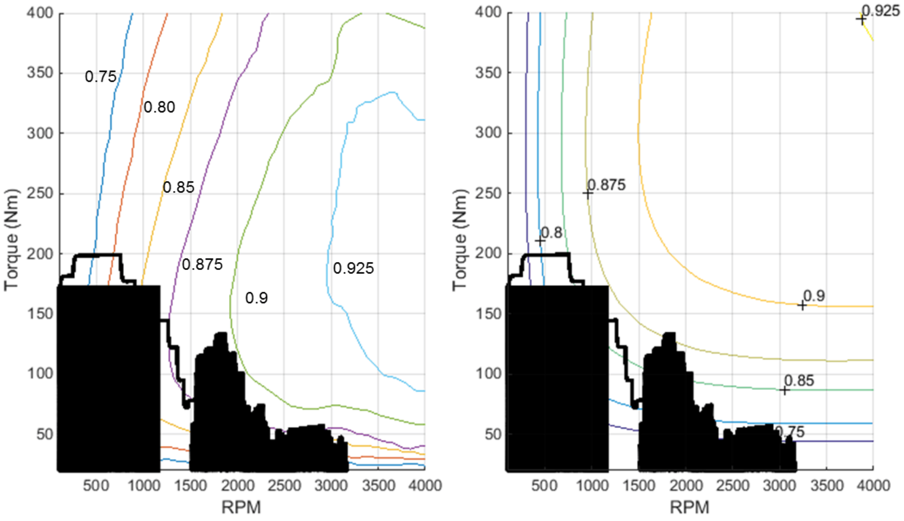

Figure 3.3: Comparison of efficiency maps for UQM PowerPhase 145 (left) and model (right) with A and B machine operating points illustrates that the model efficiency is up to 5% higher.

3.2.3 Battery Model

The battery model is derived from the work of Liu et al. [55]. The battery model is cell-based, which allows us to easily change the number of cells during system-level optimization. For simplicity, we consider a battery system where all cells are connected in series. Also for simplicity, we consider the case where the temperature in the battery is regulated and does not vary considerably. The open circuit voltage of the entire battery pack, V_0 is proportional to the open circuit voltage V_0^c of each cell as

$$V_0 = n_c V_0^c, \tag{3.23}$$

where n_c is the number of cells in the battery system.

For each of the cells, the open circuit voltage is a function of the state of charge (SOC) of the battery system. Note that we consider the case where the SOC of each cell is regulated to be approximately the same. Also, the internal resistance of each cell, R_c is a function of the SOC, and is distinct for charging and discharging. The open circuit voltage, and the charging/discharging internal resistance used in this work for each cell are shown in Fig. 3.4.

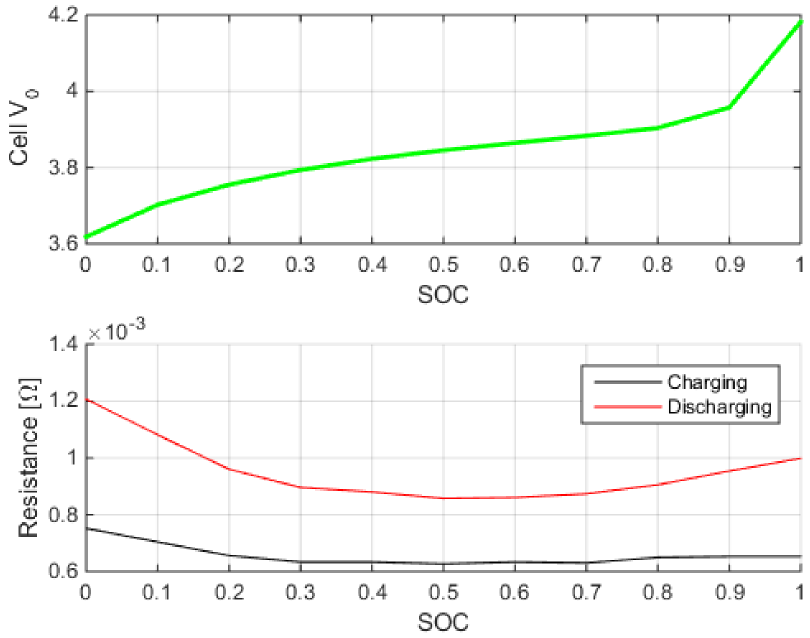

Figure 3.4: Open circuit voltage, and the internal resistance used in this work for each Li-ion cell in the battery system.

From a transfer function perspective, the battery model takes as input the power P_r required by the two electric machines, in Eq. 3.21, and outputs the voltage V_b and the SOC of the battery system as

$$V_b = V_0 - R_b I_b, \tag{3.24}$$

$$SOC = SOC_0 - \frac{1}{C_0} \int_{\tau=0}^{t} I_b d\tau, \tag{3.25}$$

where C_0 is the battery pack capacity, SOC_0 is the initial SOC, R_b is the total internal resistance of the battery system, given by $R_b = n_c R_c$, and I_b is the total current through the battery system, given by

$$I_b = \frac{1}{2R_b}\big(V_0 - \sqrt{V_0^2 - 4R_bP_r}\big), \tag{3.26}$$

Note that P_r is the total power, which can be negative when (one or both) the electric machines are generators. Also, note that the output voltage V_b of the battery is the DC voltage supplied to the power electronics, which in turn supply the A and B machines.

3.2.4 Simplified Internal Combustion Engine Model

To maximize fuel efficiency, the ICE in the novel architecture is operated either at its peak efficiency point or it is turned off. Thus, the ICE can be modeled using a very simplified approach as having an angular velocity ω_E which is constant over time, and an engine torque T_E which varies over time (due to ICE torque fluctuations). Also, the ICE is considered to be either on or off. In the off state, the ICE has zero ω_E and zero engine torque T_E. The engine torque is the sum of a constant and two sinusoidal functions, where the sinusoidal functions are chosen to resemble torque fluctuations. One example of torque fluctuations is illustrated in Fig. 3.5.

The torque fluctuation data in Fig. 3.5 is representative of experimental measurements of a 3-cylinder ICE. Such data are collected in a test of the ICE at a fixed operating point, i.e. fixed load and fixed angular velocity. The measured test data (torque) is Fourier transformed, and the DC components and two of the dominating frequencies are selected. The specific frequencies used in this process are related to the fact that the ICE has 3 cylinders. That being said, the algorithms and the overall powertrain architecture can tackle other frequencies as well. We limit the analysis to a 3-cylinder ICE for the sake of brevity.

The ICE could be operated not just as the on-and-off fashion, but also with a variable angular velocity and torque. From a system-level perspective, various

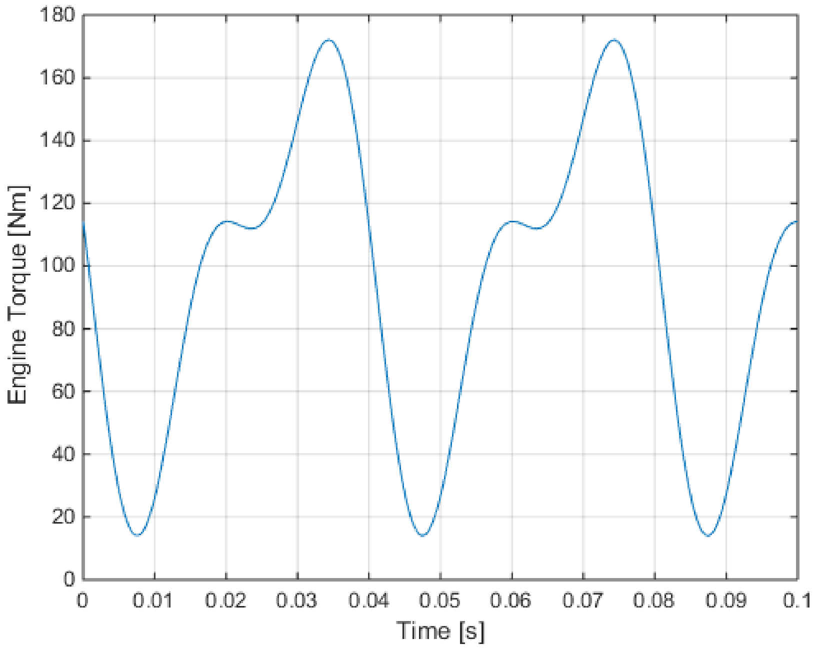

Figure 3.5: ICE torque versus time, which shows fluctuations.

ICE operations may enhance the fuel economy. However, our goal in this study is not to show the best possible fuel economy, but to demonstrate that the proposed architecture is efficient even when the system is not optimized. When the system is optimized, components are re-sized and the control logic is adjusted. This can lead to the use of various ICE operation points for optimal fuel economy.

3.2.5 Driver Model

A vehicle-level model requires a model for the driver. For clarity, we use a simple driver model, namely a PI controller [55] which takes the speed command (from a drive cycle) and the actual vehicle speed as inputs and generates two outputs, namely the operational throttle f_t, and the operational brake f_b given by

$$f_t = |max(u_s, 0)|, f_b = |min(u_s, 0)|, \tag{3.27}$$

where the variable u_s is obtained by a well known formula using proportional and integral gains denoted by k_d^p and k_d^i as follows

$$u_s = \begin{cases} -1, & u < -1 \\ u, & -1 \leq u \leq 1 \\ 1, & u > 1 \end{cases}, \text{ where}$$
$$u = k_d^p(v_r - v) + k_d^i \int\limits_{\tau=0}^{t} (v_r - v) d\tau, \tag{3.28}$$

The speed v_r is the required vehicle speed, and comes from the drive cycle. Note that since u_s is saturated between -1 and 1, both f_t and f_b vary only between 0 to 1, and they are never simultaneously non-zero. Also, f_t and f_b are used to determine the required value T_{dr} for the torque T_d as

$$T_{dr} = (f_t - f_b)T_c, \tag{3.29}$$

where T_c is a torque capacity, namely the maximum torque allowed to be required, and is a constant in the powertrain model.

3.3 Control Strategy

The control strategy is to regulate the vehicle speed and the distribution of power to or from ICE and the electric machines according to real-time driving conditions. To achieve power distribution, a control strategy with two levels is designed and two corresponding controllers are modeled. These controllers are referred to as the multi-state EECVT controller, and the hybrid controller. This section introduces the control strategy, and the logic that the two controllers follow.

The overall control architecture is illustrated in Fig. 3.6. The driver converts the speed command v_r from the drive cycle and the actual vehicle speed v in Eqs. 3.28 and 3.2 into an operational throttle signal f_t and an operational brake signal f_b using Eqs. 3.27 and 3.28. The hybrid controller converts f_t and f_b into a torque command T_{dr} in Eq. 3.29. At the same time, the hybrid controller uses the ICE operating condition (namely on or off) and calculates the torque commands for the A and B machines, namely T_{Ar} and T_{Br} which are used in Eq. 3.8. The distribution of the torque command between the A and B machines is discussed in Sec. 4.1. The torque T_d is applied downstream of the B machine. The torque T_E from the ICE and the torques T_A and T_B from Eq. 3.20 generated by the A and B machines are input to the vehicle dynamics model. The vehicle dynamics model calculates the vehicle speed v which is input to the driver model in Eq. 3.28.

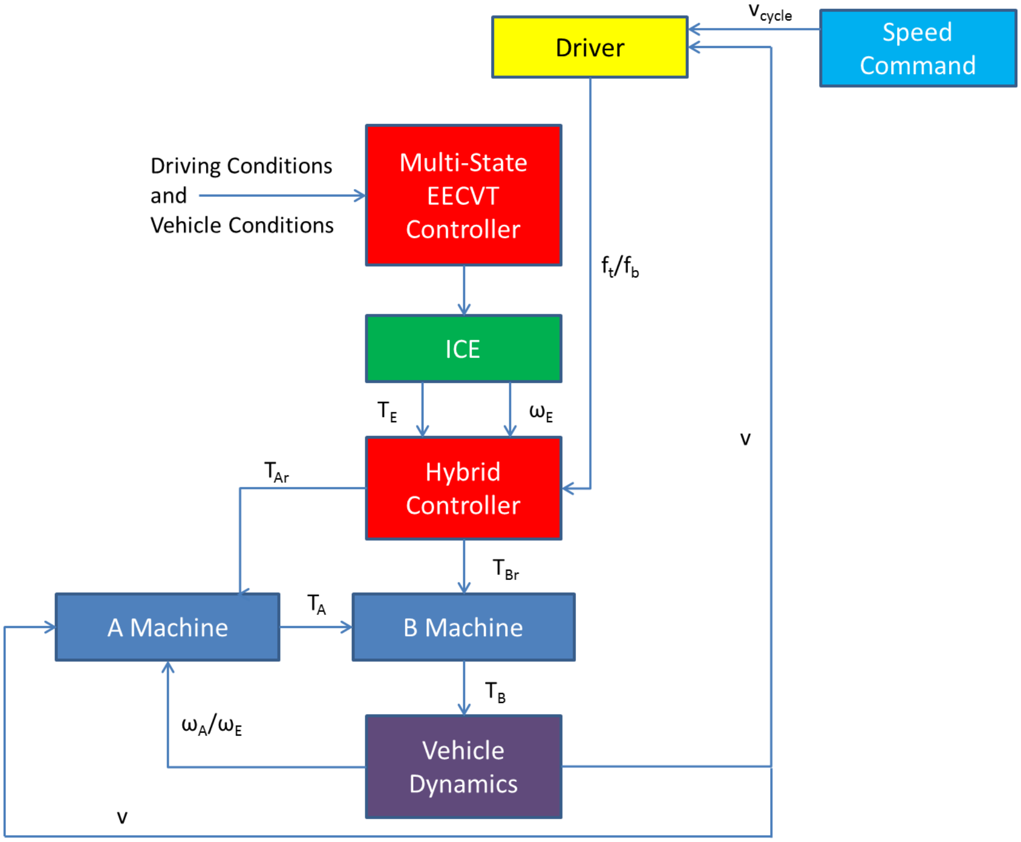

Figure 3.6: Block diagram illustrating the overall control strategy.

In addition to the processes mentioned above, the multi-state EECVT controller monitors the driving conditions, namely the vehicle speed v and the battery SOC and determines the operating point command for the ICE, namely on or off.

3.3.1 Hybrid Controller

First, we focus on the hybrid controller. This controller starts by interpreting the operational throttle signal f_t and the brake signal f_b in Eq. 3.27 from the driver as torque requirement from driver, namely T_{dr} in Eq. 3.29. The hybrid controller then distributes the torque to the A machine and to the B machine in Eq. 3.8 so that the applied torque T_d follows the required torque T_{dr}. In case of very stiff shafts, the torque T_A of the A machine is obtained from Eq. 3.20 for the steady state operation of the ICE, namely for $\ddot{\theta}_E = 0$. Hence, the hybrid controller calculates the difference between the command torque for the vehicle T_{dr} and the command torque from the A machine T_{Ar} as command torque T_{Br} to the B machine.

The hybrid controller is designed to ensure that the system operated for different ICE operating conditions. In that sense, the system can operate even without a multi-state EECVT controller, because such controller is only deciding the operating point of the ICE. However, if the ICE is not controlled according to driving conditions, but is kept at a pre-specified condition instead, some unreasonable scenarios can occur. For example, the ICE can provide more power than required into the system all the time during a drive cycle even when the battery is fully charged. This would be a waste of energy. Many other issues, beyond this simple example, may occur if the ICE is not properly controlled. The multi-state EECVT controller controls the ICE operation according to vehicle speed, required torque, battery SOC, and operational throttle. The controller makes sure that the battery SOC is kept within a reasonable range. During operations which do not involve battery-charging, the controller avoids improper energy distribution among the two electric machines.

Table 3.3: State definitions for the multi-state EECVT controller

State	**Description**	**vehicle speed**	**Torque Required**	**Battery SOC**
Rest	Vehicle parked	0	0	DC
EV Mode	Vehicle driven only by electric machine	Details shown in Table 3.4		SOC sufficient
Boost	Vehicle driven by ICE and electric machines			SOC sufficient
Regenerative Braking	Negative power required by the driver	DC	Negative	SOC sufficient
Battery Charging	Battery SOC is low, ICE is on to charge the battery	DC	DC	Expected SOC is between SOC_{med} and SOC_{high}
SOC Protection	Battery SOC is very low, ICE provides high power for SOC regeneration	DC	DC	Expected SOC is between SOC_{low} and SOC_{med}

3.3.2 Multi-State EECVT Controller

In this section, we focus on the multi-state EECVT controller. This controller follows the event-based logic. Six states are defined for different driving modes. An event means that the change in driving conditions triggers switching among states. In this controller, three variables are monitored to judge the driving conditions, namely the vehicle speed v, the torque required by the driver T_{dr}, and the battery SOC. Each state corresponds to a set of general conditions as shown in Tab. 3.3, where DC means "do not care".

The multi-state EECVT controller sustains the battery SOC during driving. The logic for the switching between states as a function of the three SOC thresholds, namely SOC_{low}, SOC_{med}, and SOC_{high} are shown in Fig. 3.7. The bar in the figure represents the battery SOC, which is 100% at the top, and 0% at the bottom. The blue and green regions are normal regions for driving. The green region shows the expected range of battery SOC where the battery should remain while driving. The yellow and red regions represent SOC ranges where the battery requires SOC regeneration, with red indicating a region of urgent requirement for SOC regeneration.

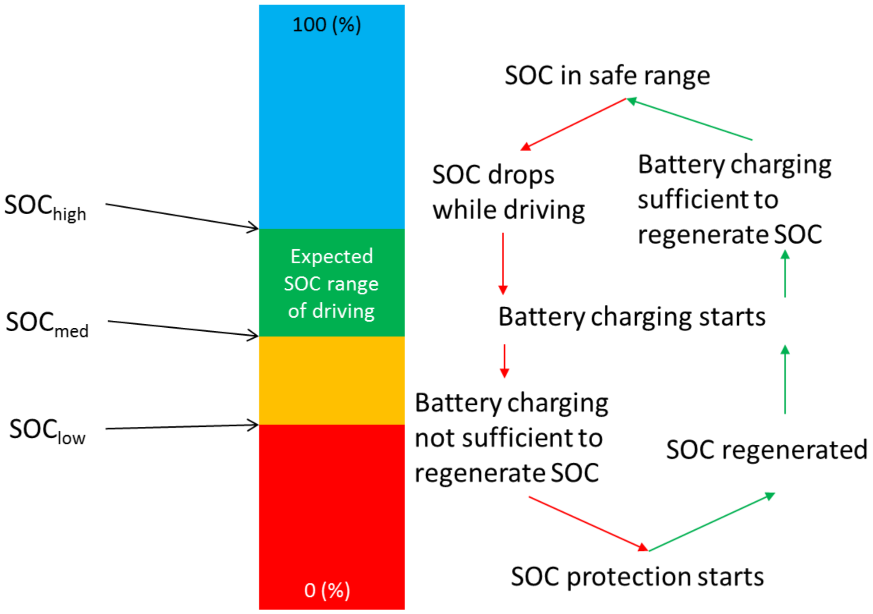

Figure 3.7: SOC control logic and threshold values with a expected switching shown on the right and the SOC values on the left.

For example, consider that the vehicle is driving with a battery SOC within the normal driving SOC region. Driving the vehicle consumes power and the SOC drops below SOC_{med}, and enters the yellow region. At this moment, the controller switches to the battery charging state. Two cases may occur when the battery charging starts. In the first case, the battery charging power from the ICE is sufficient to recharge the battery. Thus, the SOC increases back to the normal driving region, and the controller switches to normal driving states as needed. In the second case, the battery charging power from the ICE is not sufficient to regenerate the SOC and also drive. Thus, the SOC keeps dropping, and enters red region below SOC_{low}. The controller now changes to the SOC protection state, and more power is required from ICE for SOC regeneration. The battery SOC is raised until it reached SOC_{med}. After that, the battery charging state takes over and continues to charge the battery raising the SOC until it reaches SOC_{high}. The vehicle is back in the normal driving region.

Once the multi-state EECVT controller switches to the SOC protection state, the vehicle speed and the required torque are not affecting the EECVT state. The SOC protection state continues until the battery SOC reaches SOC_{med} (when the SOC protection state ends, and the battery charging state starts).

Once the multi-state EECVT controller switches to the battery charging state, the vehicle speed and the required torque are not affecting the EECVT state until the battery SOC reaches SOC_{high} (when the battery charging state ends).

Thresholds for the vehicle speed and required torque are used for switching among normal driving states, especially between the EV mode state and the boost state, whenever SOC is sufficient. The effects of the vehicle speed and required torque on state switching is summarized in Tab. 3.4. The logic is able to avoid requiring high power, either as a motor or as a generator. T_l and T_h are torque thresholds which separate low, medium and high torque values. In addition, v_t is a vehicle speed threshold between high and low speed. This value is chosen so that the vehicle speed is v_t when ω_A is close to zero and the ICE is on.

Table 3.4: Vehicle speed and required torque thresholds

Required Torque, T_{dr}	**Vehicle Speed**, v	**Desired State**
Low($< T_l$)	$< v_t$	EV Mode
Low($< T_l$)	$\geq v_t$	EV Mode
Medium($\geq T_l \& \leq T_h$)	$< v_t$	EV Mode
Medium($\geq T_l \& \leq T_h$)	$\geq v_t$	Boost
High($> T_h$)	$< v_t$	Boost
High($> T_h$)	$\geq v_t$	Boost

3.4 Results

3.4.1 System Failure Modes

In this section we present some of the consequences of the failure of the ICE, electric machines, and battery. We explore different combinations of component failures to understand when a vehicle with such failures is still able to drive. All component failure combinations which lead to a powertrain able to propel the vehicle are listed in Tab. 3.5, where 1 indicates a functional component, and 0 indicates a component which has failed.

In certain situations, a locking mechanism is needed for the B machine or for the ICE to allow the rest of the powertrain move the vehicle. Such mechanisms do not have to provide the functionality as clutches, but they are simpler locking devices. Note also that certain combinations of failures may result in an impaired ability to drive the vehicle, when not all normal driving features are available.

3.4.2 Drive Cycle Tests

The controllers together with all system components, were assembled in a vehicle-level model in MATLAB Simulink®. Simulations using this model on EPA drive cycles were carried out. These simulations include single drive cycle tests on EPA UDDS, HWFET (Highway Fuel Economy Driving Schedule), and US06 drive cycles. These tests focus on illustrating the functionality of the novel system. Also, these results were obtained for very rigid shafts, which simplify the models and the controllers needed.

The parameters used to model the vehicle are listed in Tab. 3.6. These are reasonable values selected to mimic a real commercial HEV sedan. These values were chosen without systematic system-level optimization.

First, we focus on drive cycle following, A speed, B torque, and battery SOC

Table 3.5: Powertrain failure modes where the vehicle can still move

ICE	Battery	A	B	Resultant System Description
0	1	0	1	Only EV mode is possible
0	1	1	0	EV mode when ICE engine locked
0	1	1	1	Only EV mode is possible
1	0	0	0	Need to lock beta, various ICE operation required
1	0	0	1	Need to lock beta, various ICE operation required
1	0	1	0	Need to lock beta, various ICE operation required
1	0	1	1	Need to lock beta, various ICE operation required
1	1	0	0	Need to lock beta, various ICE operation required
1	1	0	1	Need to lock beta, various ICE speed required
1	1	1	0	Various ICE torque required

sustaining performance. Figure 3.8 shows that the novel system is able to follow the drive cycle. From top to bottom, the three plots correspond to UDDS, HWFET, and US06, respectively.

The maximum errors between the target and the actual vehicle speed in the UDDS, HWFET and US06 tests were $0.1052 m/s$, $0.0975 m/s$ and $0.8078 m/s$, respectively. The largest speed error occurs in the US06 drive cycle due to sharp speed changes in this drive cycle, which require very high power and short reaction time.

The operation of the throttle and the brake is as expected, as shown in Fig. 3.9

Table 3.6: Main parameters for the vehicle-level model

Parameter	**Value**
Vehicle Mass (m_v)	$1,565kg$
Wheel Weight (m_w)	$7.5kg$
Roll Resistance (f)	0.015
Air Density (ρ)	$1.225kg/m^3$
Drag Coefficient (d)	0.25
Front Area (A)	$1.8m^2$
Wheel Radius (r_w)	$0.3m$
Final Drive Ratio (r_f)	3.267
FDR Efficiency (η_f)	0.96
Rated Battery Voltage	$330V$
Battery Capacity (C_0)	$22Ah$
Torque Capacity (T_c)	$375Nm$
Driver Proportional Gain (k_d^p)	$5s/m$
Driver Integral Gain (k_d^i)	$1/601/m$
Electric Machine Proportional Control Coefficient (c_p)	100
Electric Machine Integral Control Coefficient (c_i)	16
Torque Threshold Low (T_l)	$100Nm$
Torque Threshold High (T_h)	$200Nm$
Vehicle Speed Threshold (v_t)	$25m/s$
SOC Threshold Low (SOC_{low})	44%
SOC Threshold Med (SOC_{med})	45%
SOC Threshold High (SOC_{high})	55%

which displays the operational throttle and brake profile throughout the HWFET drive cycle.

3.4.3 Battery SOC Sustaining and Controller State

Consider a test using the EPA HWFET drive cycle. The desired battery SOC operating range are set between $SOC_{high} = 55\%$ and $SOC_{low} = 45\%$. The initial battery SOC is $SOC_0 = 55\%$. The battery SOC and the switching in the controller states over time are shown in Fig. 3.10. Results show that the battery SOC bounces between 55% and 45%, as expected. The increase in the battery SOC coincides with

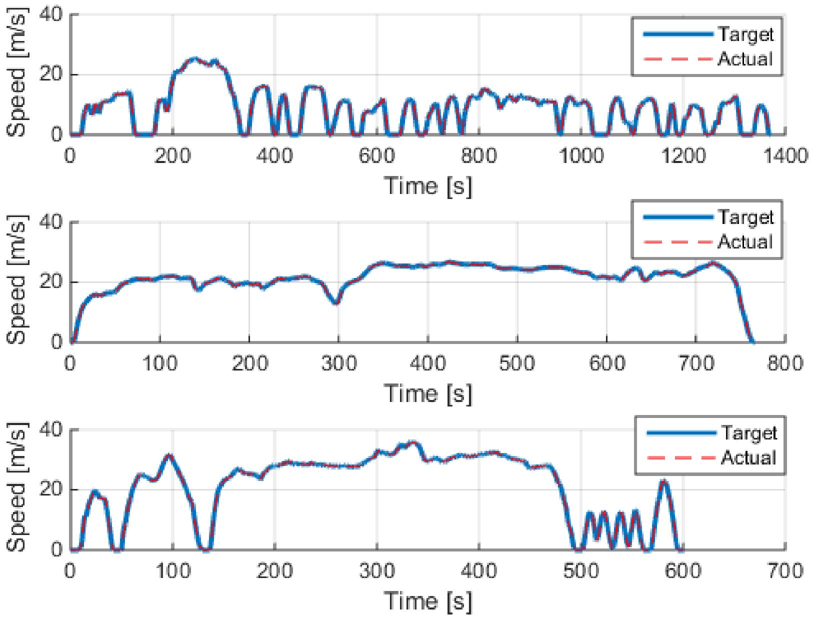

Figure 3.8: Drive cycle following results, from top to bottom, the plots correspond to the UDDS, HWFET, and US06 drive cycles.

state 5 (namely the battery charging state) over time because the system enters the battery charging state when SOC drops below 45%.

A similar result is obtained also after the multiple drive cycles. The battery SOC and ICE operation are shown in Fig. 3.11. The powertrain sustains the battery SOC effectively over time. The EPA HWFET drive cycle requires relatively low power compared to the EPA UDDS and US06 drive cycles. Also, the EPA HWFET drive cycle does not require high power or torque. Thus, the system keeps changing between EV mode and battery charging state as expected.

3.4.4 Electric Machine Performance

Recall that the angular velocity ω_A is the relative angular velocity between the A stator and A rotor. The values obtained for ω_A are shown in Fig. 3.12 for the EPA HWFET drive cycle. While the ICE is off, ω_A is proportional to the vehicle speed

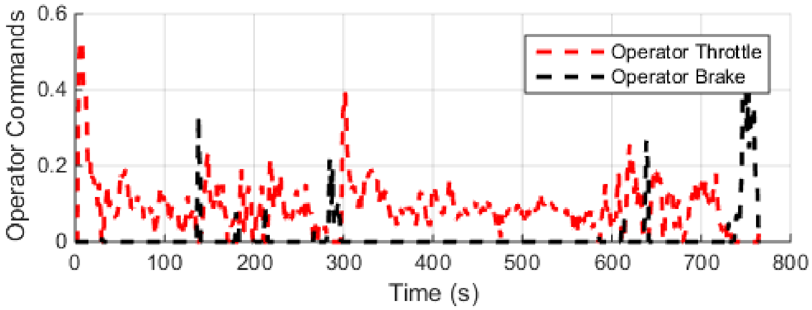

Figure 3.9: Operational throttle and operational brake profiles in the HWFET drive cycle test.

in the drive cycle because the ICE angular velocity is zero, and hence the angular velocity of the A rotor is also zero, which means that ω_A is the same as the B angular velocity ω_B, which is the same as ω_d, which is proportional to vehicle speed. However, during HWFET cycle, the system enters battery charging state, where the ICE is on. That period corresponds to the time interval in Fig. 3.12 where ω_A has low values.

The operation of the B machine depends on the ICE operating point. When the ICE is off, the powertrain is in EV mode, and the B machine is the only torque which propels the vehicle. When the ICE is on, the B machine suppresses the torque fluctuations from the ICE, and changes the average ICE torque to the required torque to follow the drive cycle. The torque in the B machine is shown in Fig. 3.13. Whenever the ICE is off, the torque in the B machine is the same as the torque required by the driver. When the ICE is on in this EPA HWFET drive cycle, the system is in battery charging state. During such periods, fluctuations in the torque of the B machine occur. A detail of the torque in the B machine when the ICE is on is shown in Fig. 3.14. A closer view of the torque in the B machine shows that its fluctuations cancel the ICE torque fluctuations. The difference between the average torque in the B machine and the output torque means that the B machine compensates the difference between the required output torque and the average ICE torque.

The power required from the A and the B machines is related to the fuel economy.

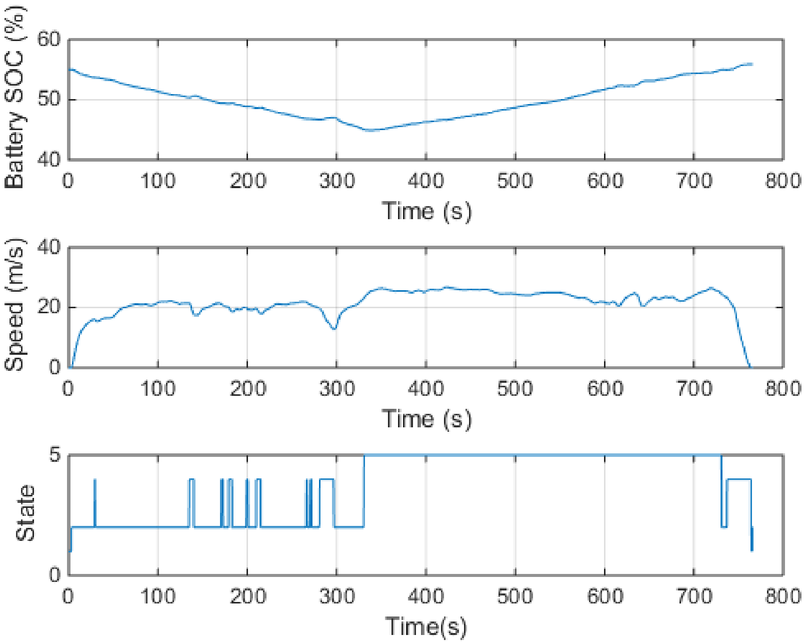

Figure 3.10: Battery SOC and the switching in the controller states over time in the EPA HWFET drive cycle.

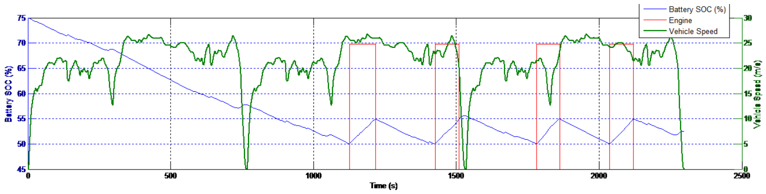

Figure 3.11: Vehicle speed, battery SOC and ICE state over time in three consecutive EPA HWFET drive cycles.

The power over time in the EPA HWFET drive cycle is shown in Fig. 3.15. The power of the A machine varies from $-10kW$ to $25kW$. The power of the B machine varies between $-40kW$ and $20kW$. The power of the A machine is zero when the ICE is off. In this drive cycle, the ICE is on when entering battery charging state, where the A power is not zero, and varies according to the ICE torque and the speed requirement. At the same time, the B machine is working as a generator most of the time when the ICE is on, which means that the ICE is providing more energy than necessary for driving during this battery charging state. Thus, the power generated by the A

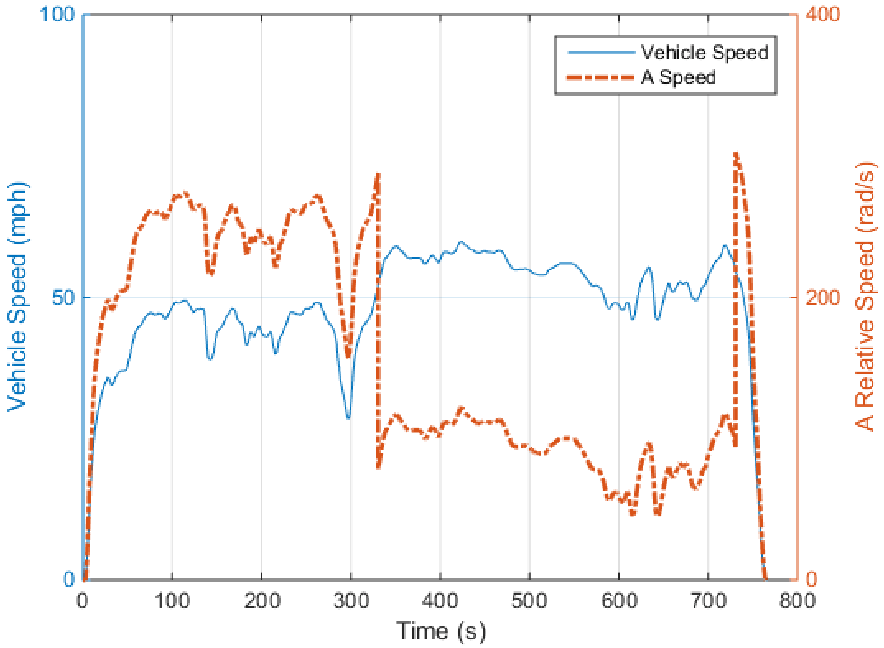

Figure 3.12: Comparison of the A speed ω_A and the vehicle speed over time in the EPA HWFET drive cycle.

machine goes to the battery. Also, the power of both the A and the B machines are fluctuating as expected due to fluctuations in the ICE torque.

3.4.5 Fuel Economy Analysis

Finding fuel economy values in miles per gallon (MPG) for HEVs requires consistent initial and final battery SOC values. To achieve consistent SOC, simulations with long duration are used so that the initial and final SOC values are the same, or the effect of the difference between the initial and final SOC values is negligible. To avoid long testing durations, we developed an alternative to assess the real-time cumulative MPG during a drive cycle. The method takes SOC variation into account.

In the proposed MPG analysis method, we consider an SOC drop from its initial value as additional fuel consumption. Also, we consider an SOC rise from its initial value as additional EV miles. Thus, we obtain an MPG value corrected for the SOC

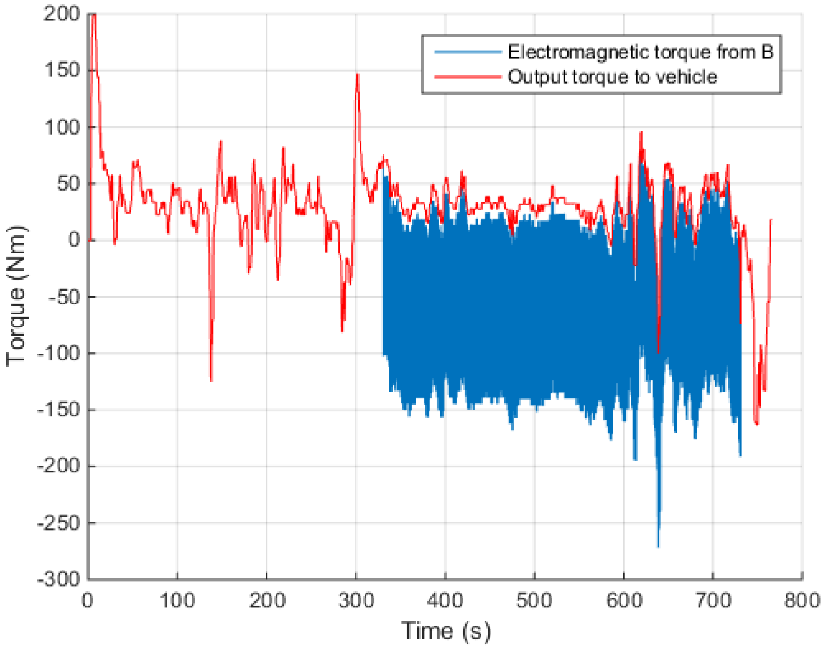

Figure 3.13: Comparison of the torque of the B machine and the output torque to the vehicle over time in the EPA HWFET drive cycle.

value. The MPG value is assessable at any moment during the simulation.

Two preliminary calculations are performed before a simulation on drive cycles. In the first calculation, we start with a low initial SOC at SOC_{med}, which is the lower bound of the expected normal SOC range during driving. Next, the ICE is turned on while the vehicle is parked. The calculation lasts until the battery SOC reaches SOC_{high}, the higher bound of the normal SOC range. We measure the total fuel consumed in this simulation, and obtain the fuel consumption per 1% SOC recovery η_d. The value of η_d is used to calculate the extra fuel consumed to charge the battery back to its initial SOC when the SOC at the end of a drive cycle is lower that the initial SOC. The corrected MPG is given by

$$MPG = \frac{D_s}{F_s + \eta_d |\Delta SOC|}, \tag{3.30}$$

where D_s is the total number of miles traveled during a simulation, F_s is the total

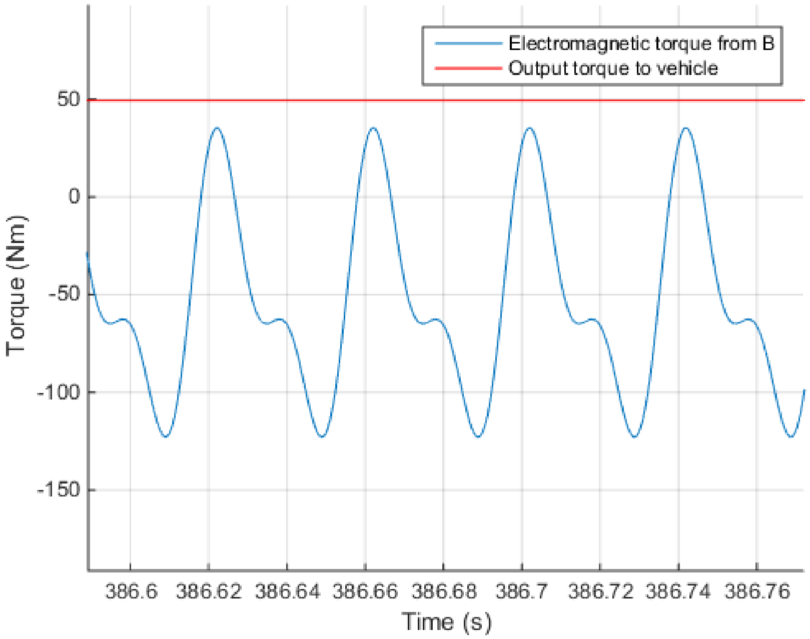

Figure 3.14: Detail of the torque of the B machine illustrates the function of the B machine as vibration suppression, canceling out the ICE torque fluctuations.

fuel consumed in that simulation, and ΔSOC is the difference between the initial and the final SOC in the simulation.

In the second calculation, the initial SOC is set at SOC_{high}, and the vehicle is driven only in EV mode on the drive cycle (which is the same as the drive cycle to be simulated) until the SOC reaches SOCmed. The total miles traveled are calculated. These extra EV miles per 1% SOC spent η_r are calculated. The corrected MPG is given by

$$MPG = \frac{D_s + \eta_r |\Delta SOC|}{F_s}, \tag{3.31}$$

The real-time MPG values obtained after correction in the EPA HWFET drive cycle is shown in Fig. 3.16.

The vehicle was tested under different drive cycles. The fuel economy performance,

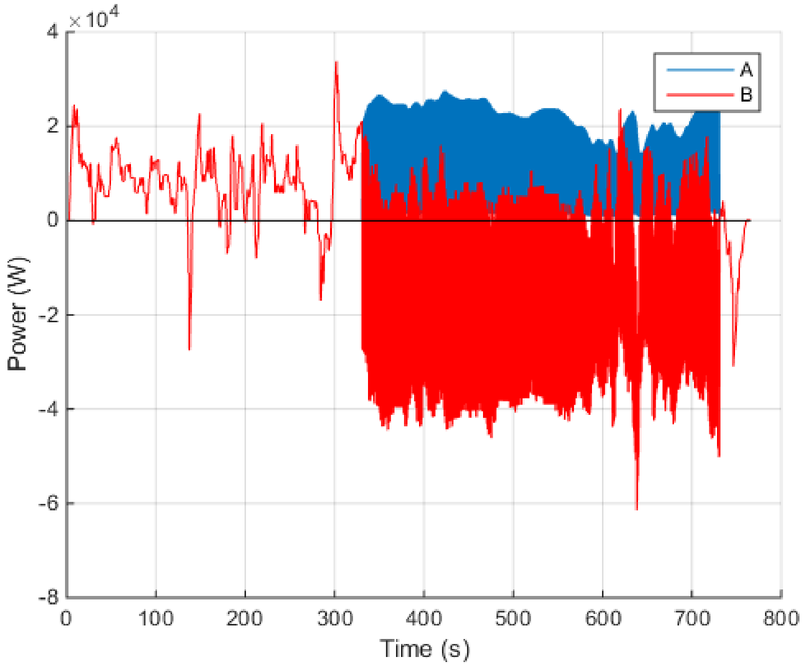

Figure 3.15: Power of the A and B machines over time in the EPA HWFET drive cycle.

in different driving conditions defined by the drive cycles are shown in Tab. 3.7.

Table 3.7: Fuel economy values for two drive cycles

Drive Cycle	**Proposed Method**	**Conventional Method**
UDDS	52.52 mpg	52.96 mpg
HWFET	54.25 mpg	53.09 mpg
Combined	53.30 mpg	53.02 mpg

We applied one of the conventional MPG calculation methods and compared the results with our strategy. We simulated our model for several consecutive drive cycles and found the cumulative fuel economy when the ending/final SOC value is the same as the starting/initial SOC value. In our case, the ICE operating point is fixed, and hence the fuel consumption is dependent essentially only on the amount of time the ICE was on, and on the number of times the ICE was turned on. The MPG results from the conventional method are shown in Tab. 3.7.

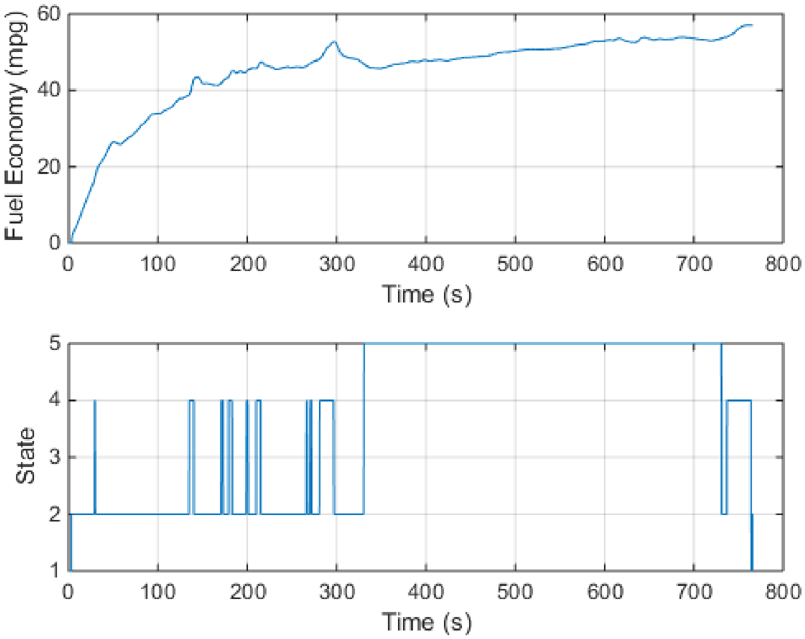

Figure 3.16: Real-time MPG values and the switching in the controller states over time in the EPA HWFET drive cycle.

The fuel economy values from both methods are close which indicates that the proposed fuel economy calculation approach is consistent with the results provided by the conventional method.

Note that the values reported here are for a system without a system-level optimization. Fuel economy is expected to improve for optimized parameter values. Such optimization includes adjusting the sizes of components, and the optimization of the control. Preliminary optimization results show improved fuel economy when the final drive ratio and the sizes of the electric machines are changed as shown below in Tab. 3.8.

Table 3.8: Fuel economy values for two drive cycles, with re-sized components

Drive Cycle	**Fuel Economy**
UDDS	70.23 mpg
HWFET	59.19 mpg
Combined	65.27 mpg

3.5 Conclusions

The high torque fluctuations in ICEs used in HEV powertrains motivated the design of a new architecture and a new EECVT system which suppresses torque fluctuations. The system takes advantage of a rotating stator of an electric machine in a new configuration which lies between a series and a power-split hybrid. The new architecture is able to change the angular velocity and torque created by an ICE, as well as to add or remove power, replacing the function of transmissions. To test the functionality of this EECVT powertrain, a vehicle-level model including the powertrain and vehicle dynamics was developed in Simulink®. In addition, a two-level control strategy was designed and modeled. The model was simulated for several EPA drive cycles. The simulation results verified that the controllers and components work as expected, and the entire powertrain is able to fulfill the goal of torque fluctuation suppression and power management while providing excellent fuel economy.

CHAPTER IV

Optimization of Novel Powertrain

4.1 Powertrain Co-Optimization Overview

A novel hybrid electric powertrain architecture was designed in an earlier work [142]. The design is illustrated in Fig. 4.1. Similar to commercially available powertrain designs, the novel powertrain architecture contains an internal combustion engine (ICE), two electric machines (machine A and B), a battery system, and a final transmission. The novelty of the powertrain is that no planetary gears or clutches are applied, by allowing the stator of machine A to rotate.

The purpose of this study is to explore the full capabilities of the new architecture architecture by co-optimizing the components the control algorithms used to operate it such that the fuel economy is maximized and component costs(sizes) are minimized. Both control and component sizes affect the powertrain performance. In addition, the design and control of powertrains are coupled, and component behaviours are nonlinear. Component sizes change the component efficiency map and have an impact on power management.

In co-optimization, the design variables are the component sizes and the control inputs at all time instances. The nested optimization allows ECMS to determine the control inputs based on the global rule of minimizing the total equivalent fuel consumption, for each set of values of the component sizes. Thus, the control inputs

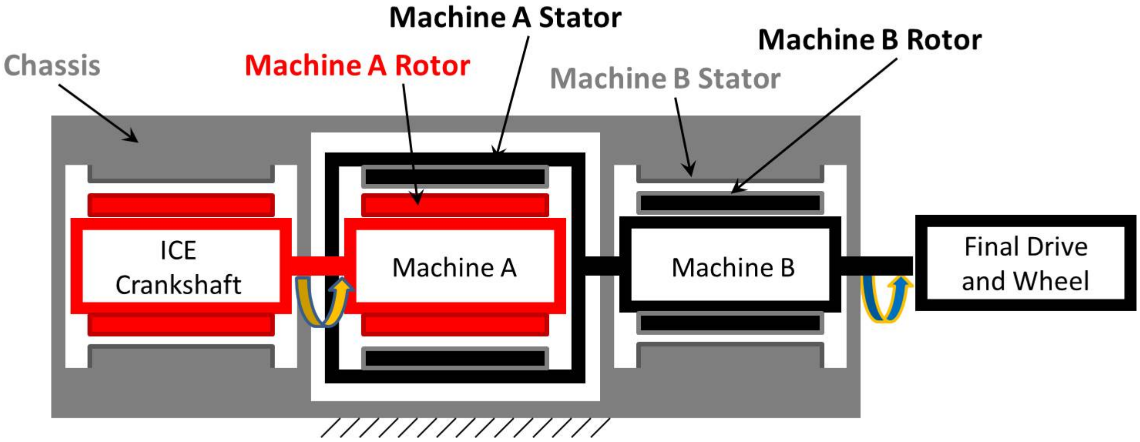

Figure 4.1: Novel powertrain allows the stator of machine A to rotate

are not explicit design variables in the powertrain co-optimization. The explicit design variables, denoted as $\mathbf{x} = [x_1, x_2, \ldots, x_7]^T$ in this study are listed in Tab. 4.1.

Table 4.1: List of design variables

Notation	**Variable**
x_1, P_{Ar}	Rated power of machine A in kW
x_2, T_{Ar}	Rated torque of machine A in Nm
x_3, P_{Br}	Rated power of machine B in kW
x_4, T_{Br}	Rated torque of machine B in Nm
x_5, r_f	Final drive ratio
x_6, V_b	Voltage of battery pack in V
x_7, C_b	Capacity of battery pack in Ah

Two powertrain performance metrics are used as utility functions in this study. The utility functions represent fuel and component costs. They can be expressed as

$$\begin{aligned} J_f &= -F_{e,cb}(\mathbf{x}), \text{ (fuel costs)} \\ J_c &= \gamma_1 x_1 + \gamma_2 x_3 + \gamma_3 x_6 + \gamma_4 x_7, \text{ (component costs)} \end{aligned} \tag{4.1}$$

where

$$F_{e,cb} = 0.55F_{e,ur}(\mathbf{x}) + 0.45F_{e,hw}(\mathbf{x}), \tag{4.2}$$

The fuel cost J_f is defined as the negative of the combined fuel economy $F_{e,cb}$, which is a weighted sum of urban and highway fuel economy $F_{e,ur}$ and $F_{e,hw}$. The component size cost J_c is based on the sizes of the electric machines and the battery pack because larger component sizes typically lead to higher manufacturing cost. The component costs in J_c are expressed as a regression of the rated power of the electric machines and the battery capacity. The regression reflects the relation between the component sizes and the dollar cost for several commercially available component products. The coefficients of the linear regression $\gamma_i, i = 1, 2, 3, 4$ are summarized in Tab. 4.2.

Table 4.2: Component size cost normalization parameter

Parameter	**Value**
γ_2	$0.0600\ kW^{-1}$
γ_3	$0.0600\ kW^{-1}$
γ_4	$0.0263\ V^{-1}$
γ_5	$0.395\ Ah^{-1}$

Both utility functions need to be minimized to obtain the best fuel economy at minimum component costs. To apply a gradient-based optimization, a single objective can be formed as

$$J = J_f + \alpha J_c, \tag{4.3}$$

where the parameter α can be adjusted to obtain different optimal solution on the Pareto front.

A nested approach is applied in this study to solve the coupled design and control optimization problem for the novel powertrain, as illustrated in Fig. 4.2. Such approach allows the application of existing control algorithms. In this study, the near-optimal control algorithm ECMS is applied. The near-optimal control algorithm ECMS is selected rather than optimal control like DP and PMP. This is due to the fact that DP is computationally expensive. The computational time to evaluate one design using ECMS is about 2 minutes CPU time, while DP requires about an hour. Applying PMP requires finding the time derivative of battery state of charge (SOC)

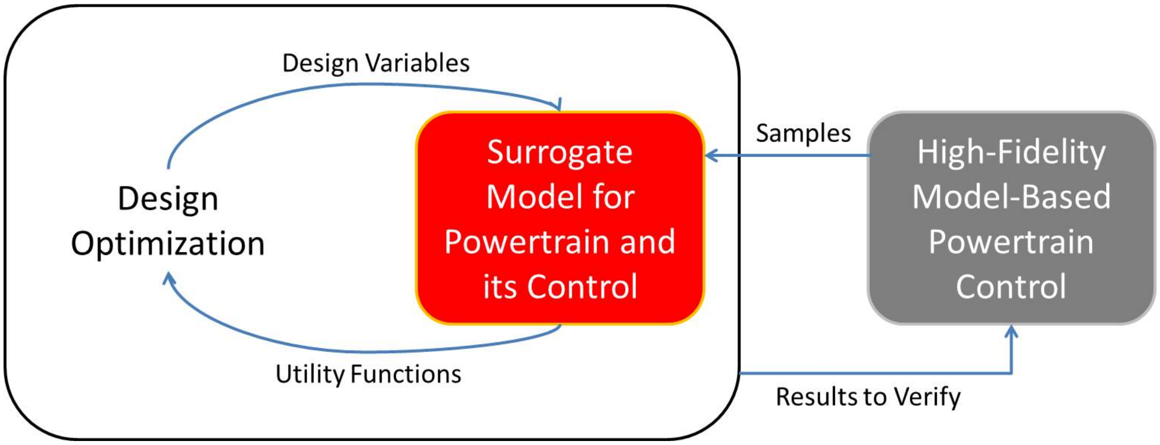

Figure 4.2: The nested co-optimization contains the design optimization as the outer loop and control optimization as the inner loop. In the inner loop, a surrogate model for a high-fidelity model with a model-based control strategy is applied. The model-based control strategy is the near-optimal ECMS control.

as a function of battery power. Computing such derivatives can be inaccurate without high-resolution battery data. In addition, the performance of powertrains using ECMS and PMP are very similar [64]. The computational cost of ECMS is slightly better than PMP due to the one fewer degree of freedom in the optimal control.

Despite these good features of ECMS, the computation efficiency still need to be improved. Thus, a polynomial surrogate model is developed for the novel powertrain architecture and its control. This surrogate model is applied as the inner loop in the nested co-optimization.

4.2 Powertrain Model and Power Management

The powertrain model contains the powertrain dynamics, component models, and ECMS control algorithm. The objective of the ECMS control is to minimize the total equivalent fuel consumption expressed as

$$\min \int_{t=0}^{t_f} \dot{m}_E(t) + \dot{m}_b(t) dt, \tag{4.4}$$

where

$$\dot{m}_b(t) = f_C f_P\big(SOC(t)\big)P_b(t), \tag{4.5}$$

$$SOC(0) = SOC(t_f). \tag{4.6}$$

The total equivalent fuel rate contains the engine fuel rate $\dot{m}_E$ and the virtual fuel rate $\dot{m}_b$ from the battery power P_b. The parameter f_C is a constant conversion factor that converts battery power to virtual fuel rate. The variable SOC denotes the battery state of charge, and f_P is the penalty function that adjusts the conversion factor for better SOC control. The constraint in Eq. 6 shows the boundary condition for the ECMS control problem. This condition eliminates the effect of total battery energy on fuel economy.

The ICE fuel rate $\dot{m}_E(t)$ and virtual fuel fate $\dot{m}_b(t)$ depend on the operation of components, including ICE, electric machines, and battery. The operations of all components are coupled through powertrain and battery dynamics. The ECMS control algorithm needs to find the operating point of all components that minimizes the equivalent fuel rate. Thus, the powertrain dynamics and component models are required to establish the relationship between the component operating point and fuel rate. These components include the ICE, two electric machines, and the battery.

4.2.1 Powertrain Dynamics

The equations of motion for the novel powertrain can be expressed as

$$\begin{aligned} (I_E + I_{AR})\dot{\omega}_E &= T_E + T_A, \\ (I_{AS} + I_B + I_d)\dot{\omega}_d &= T_B - T_A - T_r, \end{aligned} \tag{4.7}$$

where

$$T_r = f m_v g \frac{r_w}{r_f \eta_f} + \frac{1}{2}\rho_a C_d A_v \omega_d^2 \left(\frac{r_w}{r_f}\right)^3, \tag{4.8}$$

$$I_d = \frac{6m_w + m_v}{\eta_f}\left(\frac{r_w}{r_f}\right)^2, \tag{4.9}$$

$$m_v = m_f + m_A + m_B + m_{batt}. \tag{4.10}$$

$$\tag{4.11}$$

Here, the equivalent torque from road resistance is denoted as T_r. The variables ω_E and ω_d denote the ICE crankshaft and pre-final-transmission angular velocities, respectively. The torque of ICE, machine A, and machine B are denoted as T_E, T_A, and T_B. The parameters in powertrain dynamics are listed in Tab. 4.3. Further details of this model can be found at [142].

Table 4.3: Parameters of the powertrain dynamics

Notation	**Parameter**
I_E	Rotational moment of inertia, ICE crankshaft
I_{AR}	Rotational moment of inertia, machine A rotor
I_{AS}	Rotational moment of inertia, machine A stator
I_B	Rotational moment of inertia, machine B rotor
I_d	Equivalent vehicle rotational moment of inertia, pre-final-transmission
r_w	Wheel radius
η_f	Final drive efficiency
ρ_a	Air density
C_d	Drag coefficient of vehicle
A_v	Frontal area of vehicle
m_f	Mass of vehicle frame
m_w	Mass of wheel
m_v	Mass of vehicle
m_A	Mass of electric machine A
m_B	Mass of electric machine B
m_{batt}	Mass of battery system

4.2.2 Internal Combustion Engine Model

The fuel rate of the ICE can be obtained as

$$\dot{m}_E(t) = \dot{m}_E(\omega_E(t), T_E(t)), \tag{4.12}$$

where optimal brake specific fuel consumption (BSFC) operation is assumed for the ICE. Thus,

$$T_E(t) = f_{ob}(\omega_E). \tag{4.13}$$

with f_{ob} being the optimal BSFC curve, which indicates the ICE torque that grants optimal BSFC at various ICE speed.

4.2.3 Electric Machine Model

Efficiency maps for both electric machines are needed in the ECMS model. In this study, the efficiency maps depend on the sizes of both electric machines, and are generated using physics-based models. The sizes of the two electric machines in the novel powertrain are defined by 4 of the design variables, namely P_{Ar}, T_{Ar}, P_{Br}, and T_{Br} as shown in Tab. 4.1. These design variables are considered primary parameters in electric machine models. The primary parameters are required to calculate the secondary parameters that are required to generate the efficiency maps. The secondary parameters contain the wire resistances R_A, R_B, inductances L_A, L_B, and masses m_A, m_B. A second order polynomial surrogate model is created and trained to convert primary parameters to secondary parameters, using parameters collected from several commercially available electric machines.

The efficiency map contains efficiency of the electric machines at specified operating points. The operating points are defined by the torques T_A, T_B and angular speeds ω_A, ω_B for the electric machines. The mechanical power output of the two electric machines A and B can be expressed as

$$\begin{aligned} P_{m,A} &= T_A \omega_A, \\ P_{m,B} &= T_B \omega_B. \end{aligned} \tag{4.14}$$

The damping loss of each electric machine is expressed as

$$\begin{aligned} P_{lc,A} &= b_A \omega_A^2, \\ P_{lc,B} &= b_B \omega_B^2. \end{aligned} \tag{4.15}$$

where b_A and b_B represent the damping characteristics of each electric machine.

By assuming minimum current operations for both electric machines, equivalent 2-phase currents are obtained as

$$I_{d,A} = 0, I_{d,B} = 0, I_{q,A} = \frac{4T_A}{3p_A \Lambda_A}, I_{q,B} = \frac{4T_B}{3p_B \Lambda_B}. \tag{4.16}$$

Note that minimum current operation is applicable over range of angular speeds of interest in this application. Here, parameters p_A and p_B represent the number of poles. The parameters Λ_A and Λ_B denotes the permanent magnet flux linkages of each respective electric machine. Thus, the wire losses of the electric machines are expressed as

$$\begin{aligned} P_{le,A} &= (I_{d,A}^2 + I_{q,A}^2) R_A, \\ P_{le,B} &= (I_{d,B}^2 + I_{q,B}^2) R_B. \end{aligned} \tag{4.17}$$

The core loss of each electric machine can be expressed as

$$
\begin{aligned}
P_{c,A} &= \frac{(I_{d,A}^2 + I_{q,A}^2)L_A|\omega_A|\frac{p_A}{2}}{\sqrt{(L_A\omega_A\frac{p_A}{2})^2 + R_{C,A}^2}}, \\
P_{c,B} &= \frac{(I_{d,B}^2 + I_{q,B}^2)L_B|\omega_B|\frac{p_B}{2}}{\sqrt{(L_B\omega_B\frac{p_B}{2})^2 + R_{C,B}^2}}.
\end{aligned}
\tag{4.18}
$$

where $R_{C,A}$ and $R_{C,B}$ represent the equivalent core loss resistance of electric machines A and B.

The efficiencies η_A^m and η_B^m of each electric machine in motor mode and the efficiencies η_A^g and η_B^g in generator mode can be expressed as.

$$
\begin{aligned}
\eta_A &= \frac{P_{m,A}}{P_{m,A} + P_{lc,A} + P_{le,A} + P_{c,A}}, \\
\eta_B &= \frac{P_{m,B}}{P_{m,B} + P_{lc,B} + P_{le,B} + P_{c,B}}.
\end{aligned}
\tag{4.19}
$$

$$
\begin{aligned}
\eta_A &= \frac{P_{m,A} + P_{lc,A} + P_{le,A} + P_{c,A}}{P_{m,A}}, \\
\eta_B &= \frac{P_{m,B} + P_{lc,B} + P_{le,B} + P_{c,B}}{P_{m,B}}.
\end{aligned}
\tag{4.20}
$$

4.2.4 Battery Model

The bus power indicates the power flow between battery and the electric machines, and can be obtained as

$$
P_{bus} = P_{m,A}\eta_A^{-\text{sign}(P_{m,A})} + P_{m,B}\eta_B^{-\text{sign}(P_{m,B})}. \tag{4.21}
$$

The battery current is calculated as

$$
I_b = \frac{V_{oc} - \sqrt{V_{oc}^2 - 4R_bP_{bus}}}{2R_b}, \tag{4.22}
$$

where $V_{oc} = V_{oc}(SOC)$ is the open circuit battery voltage, which depends on battery SOC. The time derivative of the battery SOC and the battery power can be expressed as

$$\dot{SOC} = -\frac{I_b}{3600 C_b}, P_b = I_b V_{oc}. \tag{4.23}$$

4.2.5 Power Management

The fuel economy of a specified powertrain design using ECMS control is valid only when the boundary condition in Eqn. 7 is satisfied. The conversion factor f_c can directly affect the final SOC and the operating point selection of all components. Thus, the conversion factor f_c needs to be tuned to find the fuel economy. In ECMS simulations, different conversion factor values lead to different final SOC values, $SOC(t_f)$. One can denote the difference between the final and the initial SOC as $SOC_d = SOC(t_f) - SOC(0)$. The relationship between SOC_d and the conversion factor f_c is usually monotonic. This relationship can be written as

$$SOC_d = f_{ECMS}(f_c). \tag{4.24}$$

To ensure satisfaction of the SOC boundary condition in ECMS, finding the root of Eqn. 4.24 is required. A iterative root searching method, namely the secant search, is applied in this study as

$$f_{c,i} = f_{c,i-1} - \frac{SOC_{d,i-1}}{g_{i-1}}, \tag{4.25}$$

where

$$g_{i-1} = \frac{SOC_{d,i-1} - SOC_{d,i-2}}{f_{c,i-1} - f_{c,i-2}}. \tag{4.26}$$

Here, subscript i indicates that the value belongs to the i^{th} iteration. The root of Eqn. 4.24 can be denoted as f_c^*. For each value of the conversion factor f_c, a fuel economy result F_e can be obtained. The fuel economy that corresponds to f_c^* is considered the fuel economy value with SOC correction, or f_e^*. This process is repeated for both EPA urban and highway drive cycles for fuel economy. Thus, the urban and highway fuel economy of the specified powertrain design, $f_{e,ur}$ and $f_{e,hw}$, are obtained.

4.3 Surrogate Model

A surrogate ECMS model can reduce the computational cost in control optimization. Polynomial surrogate models are often used [10]. Such models can be expressed in a general form as

$$y(\mathbf{x}) = \sum_{m_7=0}^{r_7} \sum_{m_6=0}^{r_6} \sum_{m_5=0}^{r_5} \sum_{m_4=0}^{r_4} \sum_{m_3=0}^{r_3} \sum_{m_2=0}^{r_2} \sum_{m_1=0}^{r_1} (\beta_n \prod_{i=1}^{7} x_i^{m_i}), \tag{4.27}$$

where indices $m_i, i = 1, 2, \ldots, 7$ represent the order of each design variable. Parameters $r_i, i = 1, 2, \ldots, 7$ are integers that denote the maximum order of each design variable. Each of the indices m_i is an integer that ranges from 0 to r_i. β_n represent the coefficients of all terms in the polynomial surrogate model. The index n of each term in the polynomial model is between 1 and $\prod_{i=1}^{7}(r_i + 1)$. The relationship between n, m_i, and r_i can be expressed as

$$n = \sum_{a=2}^{7} m_a \prod_{b=1}^{a-1}(r_b + 1) + m_1. \tag{4.28}$$

The maximum order r_i of design variables x_i needs to be selected for the surrogate model. At first, latin hypercude sampling (LHS) is applied to generate approximately $40,000$ valid powertrain designs, which are combinations of the 7 design variables in vector $\mathbf{x}$. The combined fuel economy of all these designs are evaluated using the high-fidelity ECMS model. The resulting data set is divided into a training and a validation set (in a $80\% - 20\%$ ratio).

Training the surrogate model with a specified set of maximum orders r_i is equivalent to finding coefficients β_n of all terms. The total number of samples within the training set is denoted as N, and the k^{th} design is denoted by $\tilde{\mathbf{x}}^{(k)} = [x_1^{(k)}, x_2^{(k)}, \ldots, x_7^{(k)}]$, $k = 1, 2, \ldots, n$. The combined fuel economy of the k^{th} sample is denoted as $y^{(k)}$, where $y^{(k)} = F_{e,cb}(\mathbf{x}^{(k)})$, given by Eqn. 4.1. For a specified set of maximum orders r_i, a matrix $\tilde{\mathbf{X}}$ and a column array $\tilde{\mathbf{y}}$ are constructed. The matrix $\tilde{\mathbf{X}}$ is a N by $\prod_{i=1}^{7}(r_i + 1)$ matrix. The terms on the k^{th} row and n^{th} column of $\tilde{\mathbf{X}}$ can be denoted as $\tilde{X}_{k,n}$. The k^{th} term in $\tilde{\mathbf{y}}$ can be denoted as $\tilde{y}_k$. Elements in the matrix $\tilde{\mathbf{X}}$ and in the array $\tilde{\mathbf{y}}$ can be expressed as

$$\tilde{X}_{k,n} = x_1^{(k)^{m_1}} x_2^{(k)^{m_2}} x_3^{(k)^{m_3}} x_4^{(k)^{m_4}} x_5^{(k)^{m_5}} x_6^{(k)^{m_6}} x_7^{(k)^{m_7}}, \tag{4.29}$$

$$\tilde{y}_k = y^{(k)}, \tag{4.30}$$

where the relationship between index of term n and order of variables m_i is expressed in Eqn. 4.28.

Matrix $\tilde{\mathbf{X}}$ can be close to singular due to the existence of high-order polynomial terms for large r_i values. Normalization of $\tilde{\mathbf{X}}$ and $\tilde{\mathbf{y}}$ addresses this issue. The normalized matrix and array can be denoted as $\mathbf{X}$ and $\mathbf{y}$, respectively. The column-wise normalization is expressed as

$$\begin{aligned} \mathbf{X}_n &= \frac{\tilde{\mathbf{X}}_n - \bar{\mathbf{X}}_n}{\sigma(\tilde{\mathbf{X}}_n)}, \\ \mathbf{y} &= \frac{\tilde{y} - \bar{y}}{\sigma(\tilde{y})}, \end{aligned} \tag{4.31}$$

where $\tilde{\mathbf{X}}_n$ and $\mathbf{X}_n$ are the n^{th} column in matrices $\tilde{\mathbf{X}}$ and $\mathbf{X}$, respectively. The terms $\bar{\mathbf{X}}_n$ and $\sigma(\tilde{\mathbf{X}}_n)$ denote the average value and the standard deviation of all elements in column $\tilde{\mathbf{X}}_n$. Note that the first column in $\tilde{\mathbf{X}}_n$ contains all ones as elements and represents the constant term in the surrogate model. This column can remain the same in the normalized matrix $\mathbf{X}_n$. Thus, the normalization for $\tilde{\mathbf{X}}_n$ is executed for $n = 2, 3, \ldots, \prod_{i=1}^{7}(r_i + 1)$. Finally, the following equation holds for normalized matrix $\mathbf{X}$ and array $\mathbf{y}$.

$$\mathbf{x}\boldsymbol{\beta} = \mathbf{y}, \tag{4.32}$$

where $\boldsymbol{\beta}$ is a column array with elements β_n. The array $\boldsymbol{\beta}$ contains all coefficients of the normalized surrogate model. The coefficients $\boldsymbol{\beta}$ that minimize the regression error between the model and data can be obtained as

$$\boldsymbol{\beta} = (\mathbf{X}^T\mathbf{X})^{-1}\mathbf{X}^T\mathbf{y}. \tag{4.33}$$

For powertrain designs within the validation set, the performance approximations are obtained using the surrogate model. These approximations can be denoted as $\mathbf{y}_s$. The results given by the high-fidelity ECMS model can be denoted as $\mathbf{y}_v$. A residual δ is applied as criterion of determining the quality of the surrogate model. The residual is expressed as

$$\delta = \frac{\|\mathbf{y}_s - \mathbf{y}_v\|_2}{\|\mathbf{y}_v\|_2}. \tag{4.34}$$

The residual values are associated with each combination of r_i values. The combination of maximum orders r_i that yields the smallest residual in the surrogate model validation are listed in Tab. 4.4. These r_i values are used in the overall co-optimization.

Table 4.4: Maximum orders of design variables in the tuned surrogate model

Order	r_1	r_2	r_3	r_4	r_5	r_6	r_7
Value	5	2	4	2	4	1	1

4.4 Optimization Results and Discussion

4.4.1 Parameters and Constraints

A mid-sized passenger vehicle is chosen to demonstrate the design and control co-optimization for novel powertrain. The parameters of the vehicle are specified in Tab. 4.5. Limits of design variables are shown in Tab. 4.6. Safety and physical constraints are summarized in Tabs. 4.7 and 4.8.

Table 4.5: Vehicle parameters in powertrain optimization problem

Notation	**Value**	**Notation**	**Value**
f	0.0015	r_w	0.287 m
η_f	0.96	ρ_a	1.20 kg/m^3
C_d	0.29	m_w	7.5 kg
m_f	1,560 kg	A_v	2.20 m^2

Table 4.6: Litmits of design variable

Variable	**Lower bound**	**Upper bound**
x_1	20 kW	100 kW
x_2	150 Nm	400 Nm
x_3	20 kW	100 kW
x_4	150 Nm	400 Nm
x_5	1.75	5.25
x_6	100 V	400 V
x_7	5 Ah	30 Ah

Table 4.7: Physical constraints

Expression	**Description**
$c_1 x_2 - x_6 \leq 0$	Minimum battery voltage requirement to drive machine A
$c_1 x_4 - x_6 \leq 0$	Minimum battery voltage requirement to drive machine B
$-\frac{30}{\pi}\frac{x_1}{x_2} + c_2 \leq 0$	Minimum nominal angular velocity requirement of machine A
$-\frac{(x_4+T_{En})x_5}{r_w m_v} + c_3 \leq 0$	Vehicle acceleration capacity requirement
$(x_4 + T_{En})x_5 - c_4 \leq 0$	Maximum shaft torque allowance

Table 4.8: Parameters in Physical Constraints

Parameter	**Value**	**Description**
c_1	0.45 V/Nm	Voltage/torque conversion factor
c_2	2,000 rpm	Angular velocity threshold
c_3	2 m/s^2	Vehicle acceleration threshold
c_4	4,000 Nm	Driving shaft torque threshold
T_{En}	100 Nm	Most frequent engine torque

The conversion factor c_1 in Tab. 4.8 is derived from electric machines and power electronics models for different motor sizes. The threshold value c_2 is derived from the powertrain kinematics. Parameters c_3 and c_4 are empirical values from powertrain simulations of mid-sized passenger HEVs.

4.4.2 Optimization of the Novel Powertrain

Multiple objectives are considered in the co-optimization problem as stated in Eqn. 4.1. An approximation of the Pareto front for the novel powertrain architecture is necessary. Collecting results from all LHS-generated powertrain designs when building the surrogate model, the Pareto front obtained for the novel architecture is shown in Fig. 4.3.

The Pareto front is approximated using all data points. Adjusting the parameter α leads to different single utility functions as shown in Eqn. 4.3. A family of straight lines $J_f + \alpha J_c = J$ can be defined in the (J_f, J_c) space. There exist a straight line $J_f + \alpha_{sl} J_c = J_{sl}$ that is tangent the Pareto front for some α_{sl} value. In this case, the tangential point indicates the optimal design for the single objective function $J = J_f + \alpha_{sl} J_c$. Multiple tangential lines are shown in Fig. 4.4, which select different optimal designs.

The Pareto front curve illustrated in Fig. 4.4 is an approximation of the exact

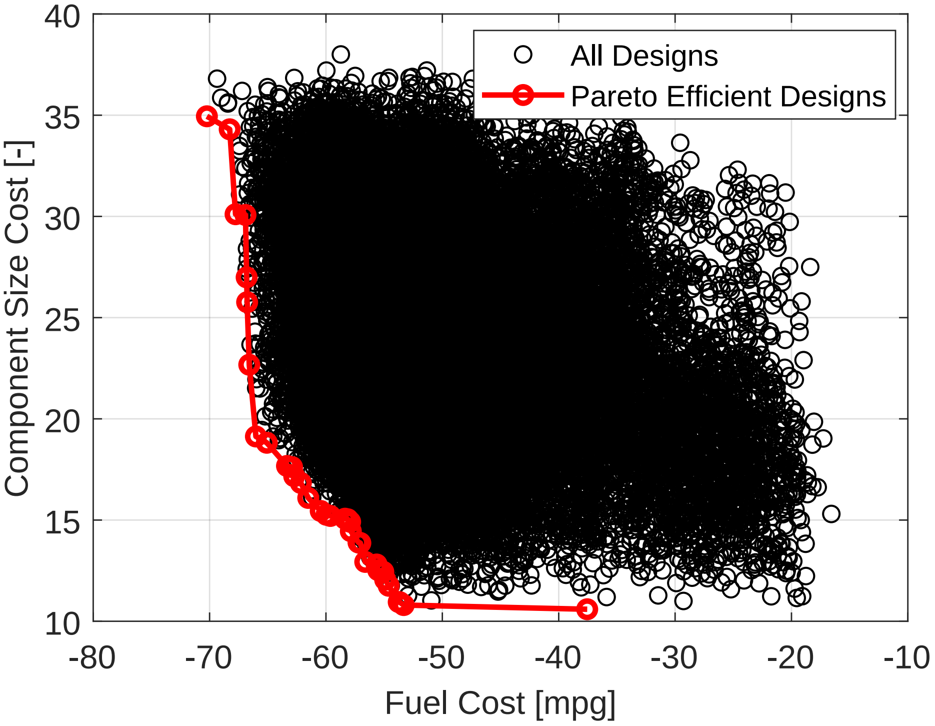

Figure 4.3: An approximation of the Pareto front can be obtained by selecting Pareto efficient designs in the (J_f, J_c) space using simulation results collected from randomly generated designs.

Pareto front, due to the fact that exhaustive search in continuous design space is impossible. Thus, powertrain optimization is necessary. In this study, multiple initial powertrain designs are randomly generated in the design space. A modified single objective function is applied in optimization. A soft penalty on large deviation between urban and highway drive cycle is added to the objective function as

$$\hat{J} = J_f + \alpha J_c + J_d, \tag{4.35}$$

where

$$J_d = \gamma_5 \big(\max(0, |F_{e,ur} - F_{e,hw}| - 10)\big)^2. \tag{4.36}$$

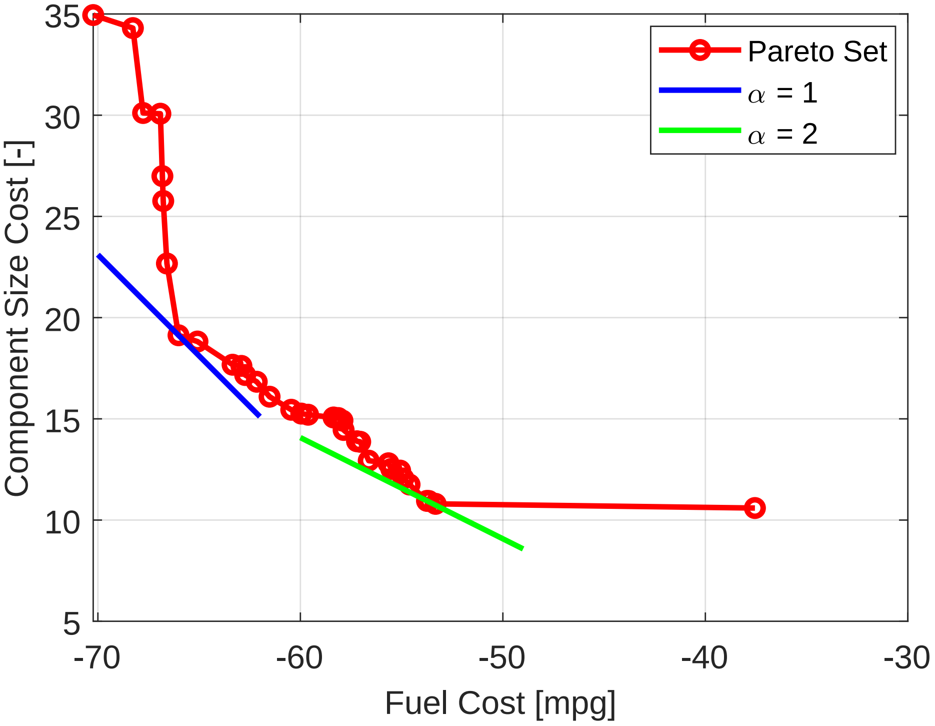

Figure 4.4: The optimal design can be selected using straight lines that represent a single utility function. The tangential point of the straight line and Pareto front can be considered a near-optimal design. Varying the value of α forms different single utility functions and leads to a different slope of the straight line.

Surrogate model is applied in the nested powertrain optimization as an approximation of ECMS model. Thus, the performances of the optimal designs are evaluated using the ECMS model. The residual between the surrogate model and the high-fidelity ECMS model for the optimal designs are computed using the method illustrated in Eqn. 4.34. The residual is less than 3%. This small residual value verifies that the surrogate model is an accurate approximation of the ECMS model at optimal designs. In addition, the optimal design variables are rounded considering commercial availability of components. Specifically, designs are obtained by rounding the all design variables except for final drive ratio. Optimal designs for two α values are presented in Tab. 4.9.

Table 4.9: Optimal Designs for Novel Powertrain

	Optimal Design 1		**Optimal Design 2**	
Variable	**Original**	**Rounded**	**Original**	**Rounded**
α	1 mpg	1 mpg	2 mpg	2 mpg
P_{Ar}	54.66 kW	55.00 kW	30.48 kW	30.00 kW
T_{Ar}	334.2 Nm	330.0 Nm	170.0 Nm	170.0 Nm
P_{Br}	88.19 kW	90.00 kW	41.93 kW	40.00 kW
T_{Br}	231.7 Nm	230.0 Nm	363.4 Nm	360.0 Nm
r_f	2.003	2.003	2.158	2.158
V_b	162.4 V	162.0 V	160.7 V	161.0 V
C_b	15.87 Ah	16.00 Ah	5.968 Ah	6.000 Ah
$J_f(-F_{e,cb})$	-66.02 mpg	-65.69 mpg	-54.24 mpg	-53.66 mpg
J_c	19.13	19.30	10.94	10.82

4.4.3 Benchmark Powertrain Architectures

Existing powertrain architectures are compared to the novel architecture. Specificly, four commercially available benchmark powertrain (BP) configurations are selected, including Toyota Hybrid System generations 1 through 3 (BP1, BP2, BP3) and Chevy Volt generation 2 (BP4). The configurations of the four selected BPs are illustrated in Fig. 4.5. In this study, the same vehicle parameters as in the novel powertrain co-optimization are applied when evaluating the BPs.

All selected BPs are in power split topology due to their similarity in component operations with the novel powertrain, regardless of the number of planetary gears (PGs). All BP configurations contain an ICE and two electric machines. The electric machines are referred to as motor/generator (MG). For all BP configurations, the engine and one of the electric machines (MG1, WLOG) are directly connected to the same PG (PG1) that is farthest from the wheel. In such a connection, MG1 allows the freedom of choosing the ICE speed. At the same time, MG1 is able to leverage the torque that is transferred to the vehicle. Thus, the functions of MG1 is similar to machine A in the novel powertrain.

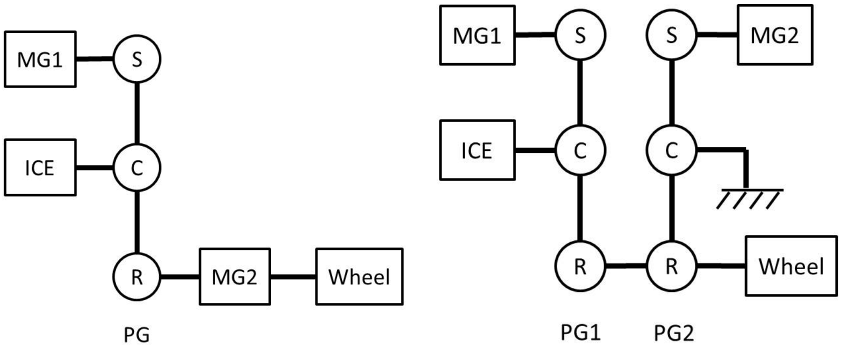

(a) BP1 (b) BP2

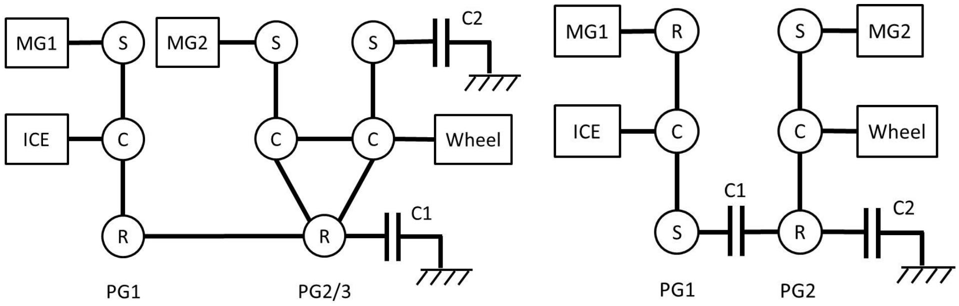

(c) BP3 (d) BP4

Figure 4.5: Architectures of the benchmark power-split hybrid powertrains are illustrated using level diagram. The notations S, C, and R represents sun, carrier, and ring gear in a planetary gear (PG), respectively. The powertrain components, namely the ICE and the electric machines are denoted as ICE, MG1, and MG2. Clutches are denoted as C1 and C2 for BP3 and BP4. Engaging different clutches in BP3 and BP4 lead to different powertrain operating modes.

The wheels and MG2 are typically connected to the same PG (PG2). Thus, MG2 is able to drive the vehicle or regenerate power directly. For multi-mode configurations, engaging different clutches only changes the gear ratio from MG2 to vehicle or ICE to vehicle. Thus, the function of MG2 is similar to Machine B in the novel powertrain.

A Three-PG configuration usually just adds an additional PG as additional transmission to the powertrain either between PG1 and PG2, or between PG2 and the wheels. This does not change the functionality of the ICE, MG1 and MG2.

Over 1,000 designs are generated using LHS for each BP. These data provide an

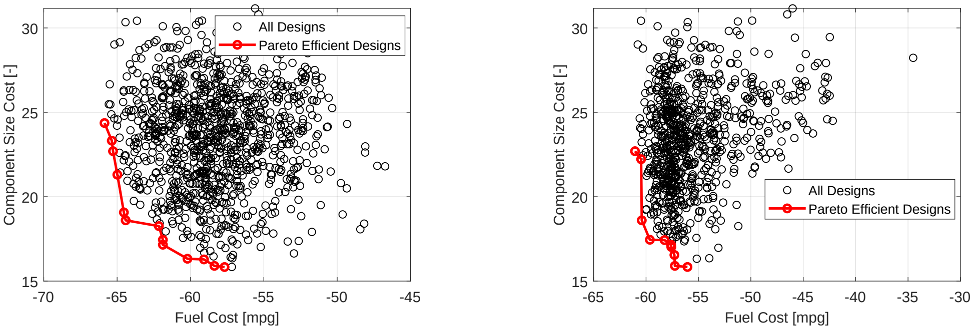

(a) BP1 (b) BP2

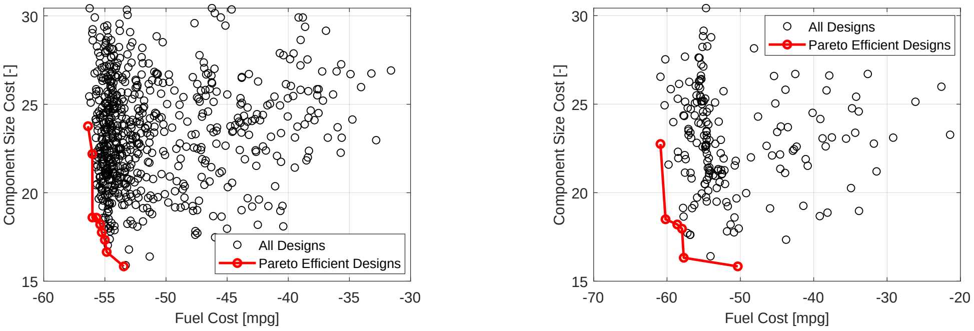

(c) BP3 (d) BP4

Figure 4.6: Simulation results for all benchmark powertrains are shown. The approximation of Pareto fronts are obtained by selecting Pareto efficient designs. The plot is ordered as (a) BP1, THS G1; (b)BP2, THS G2; (c) BP3, THS G3; (d) BP4, Volt G2.

approximation of the Pareto front for each BP, as shown in Fig. 4.6.

To compare the performance of BPs and the novel powertrain, same weight α is selected as applied earlier for the novel powertrain. Under each selected α value, the best design is determined and applied as the initial design in a BP optimization. The fuel economy and component cost J_c of optimal designs for novel architecture and all BPs are shown in Fig. 4.7. These optimal designs for all BPs are specified and illustrated in Tabs. A.1 through A.4 in Appendix A. Similar to the optimal novel powertrain designs, designs with rounded component sizes are illustrated for BPs. The columns indicated as rounded contain the powertrain designs with rounded

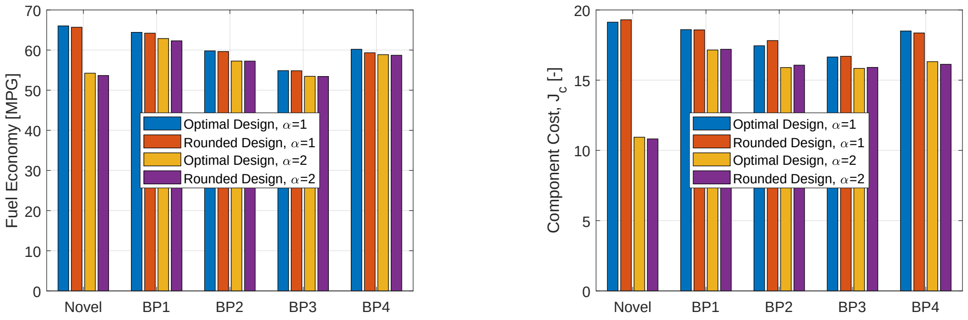

(a) Fuel Economy

(b) Component Cost

Figure 4.7: The optimal powertrain architecture shows comparable performance with all BPs. Novel Architecture is more sensitive to the value of α.

design parameters and the performance metrics for such designs.

The optimal novel powertrain designs perform comparably with optimal BP designs. Overall the performance of BP1 and BP4 are closer to the novel powertrain, while the performance of BP2 and BP3 can be slightly worse. The main reason for this difference is that BP2 and BP3 are designed for vehicles in a different size from the mid-sized passenger vehicle in this study. In contrast, the original commercially available vehicles for BP1 and BP4 are vehicles with similar size.

Among the conventional power-split hybrid powertrain configurations like the BPs, the factors that affect the powertrain performance are the gear ratios. The net effect of changing the number of PGs, the ratio of such PGs, and mode switches (clutch engagements) is changing the gear ratios, specifically the net gear ratios from components to wheels. Taking BP1 and BP2 as examples, these are architectures in two consecutive generations of the Toyota Hybrid System. One additional PG is added between MG2 and wheels in BP1 and forms BP2. Thus, the net gear ratios from engine to wheels and from MG1 remain the same. The only difference between BP1 and BP2 is the net gear ratio between MG2 and the wheels. This leads to the difference of performance among all BPs.

The novel powertrain architecture does not demand any PGs or clutches. Nevertheless, the novel powertrain allows the stator of machine A to rotate. Thus, the freedom in selecting the ICE operation point is granted like in power-split powertrains. In addition, machine A allows a various ratio transmission between such component and the wheels. In contrast, the net gear ratio from MG1 to wheel in power-split hybrid powertrains is either fixed or contains a limited number of choices. Thus, the operation of machine A in novel powertrain is more flexible than in power-split powertrains. Nevertheless, machine B in the novel powertrain architecture is less flexible than MG2 in power-split powertrains. Machine B is a conventional electric machine without transmission. In power-split powertrains, PG2 usually serves as the transmission for MG2. Proper selection of gear ratio can improve efficiency in MG2 operations. Thus, machine A operation in the novel powertrain architecture is more flexible than that for MG1 in power-split powertrains, while the contrary applies for machine B and MG2.

4.5 Conclusions

This study demonstrated the co-optimization of the design and control for a novel powertrain architecture. Fuel economy and component sizes were considered as utility functions. A nested approach was applied to decouple the design and control optimization problems and to make use of an existing near optimal power management strategy, ECMS. A high-fidelity powertrain model with physics-based component models and ECMS control were implemented. Using randomly generated powertrain designs, an approximation of the Pareto front in the objective space was formed. A single objective function is formed using a weighted sum of utility functions. Optimal solutions were obtained through single objective optimization by assigning different weight values to individual utility functions. A polynomial surrogate model was designed and trained to improve computational efficiency of the optimization process. The optimal novel powertrain designs were compared with optimal designs for several selected benchmark powertrains. The selected powertrains all have a power-split configuration. Overall, the performance of the novel powertrain architecture is comparable to the selected benchmark powertrains. Although the novel powertrain does not require any planetary gears or clutches, similarities in functionalities of components were identified. The lack of planetary gears or clutches trades flexibility of machine B operation for that of machine A operation.

CHAPTER V

Platooning of Connected Hybrid Electric Vehicles

5.1 Overview of Platoon Optimization

The purpose of platoon optimization in this study is to enhance the drive schedule and vehicle control for a platoon that is executing a specific task in order to minimize energy consumption, while maintaining the platoon ability to keep a desired headway between neighbouring vehicles. The task of the platoon is to move a desired distance with a limited time on a road with given road load. In this study, the road load considers road resistance from the road grade. A three-subsystem optimization framework organized in a three-layer structure is created, as shown in Fig. 5.1.

The optimization subsystem optimizes the drive schedule and vehicle controls for a platoon. The drive cycles and parameters for vehicle controls from the optimization subsystem are sent to the platoon subsystem. The high-level vehicle controller determines the traction or brake force for each vehicle. The traction or brake requirement for each vehicle is handled by the powertrain subsystem. The traction or brake force generated by the powertrain is sent to the platoon dynamics. The performance of the platoon on the current drive cycle is reported to the optimization subsystem.

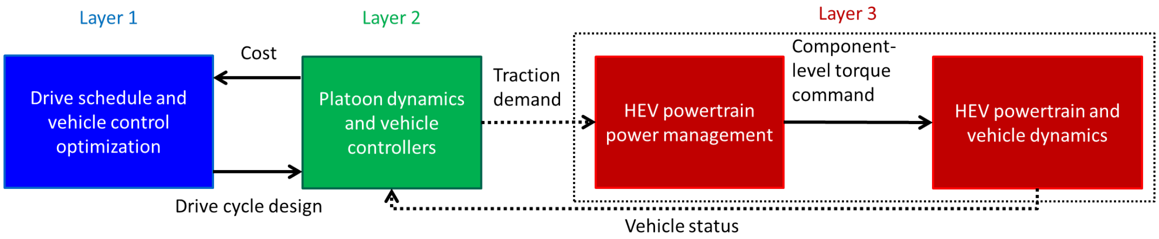

Figure 5.1: A three-layer optimization framework is shown. The optimization subsystem on the left solves the drive schedule and vehicle control optimization problem. The middle layer contains the platoon subsystem, including platoon dynamics and vehicle controllers. The powertrain subsystem, including component models and powertrain controls, are on the right. The powertrain subsystem can be simplified to enhance computational speed.

5.2 Powertrain Model

5.2.1 Component Models

The powertrain configuration explored in this study was developed in an earlier study [142]. The configuration is illustrated in Fig 5.2. The internal combustion engine (ICE) is connected to the rotor of electric machine A. The stator of machine A is allowed to rotate and is connected to the rotor of electric machine B. Machine B is a conventional electric machine connected to the final transmission and vehicle.

This powertrain consists of 2 degrees of freedom (DOF) when all shaft connections are considered rigid. The powertrain dynamics for the i^{th} vehicle in a platoon can be expressed as

$$\begin{aligned}(I_{E,i}+I_{AR,i})\ddot{\theta}_{E,i} =& T_{E,i}+T_{A,i},\\ (I_{AS,i}+I_{B,i}+I_{d,i})\ddot{\theta}_{d,i} =& T_{B,i}-T_{A,i}-T_{r,i},\end{aligned} \tag{5.1}$$

where the parameters and variables in this equation are illustrated in Tab. 5.1. In the context of platoon models, including platoon dynamics and powertrain control, the subscript i represents a variable or parameter that belongs to the i^{th} vehicle, if not specified otherwise.

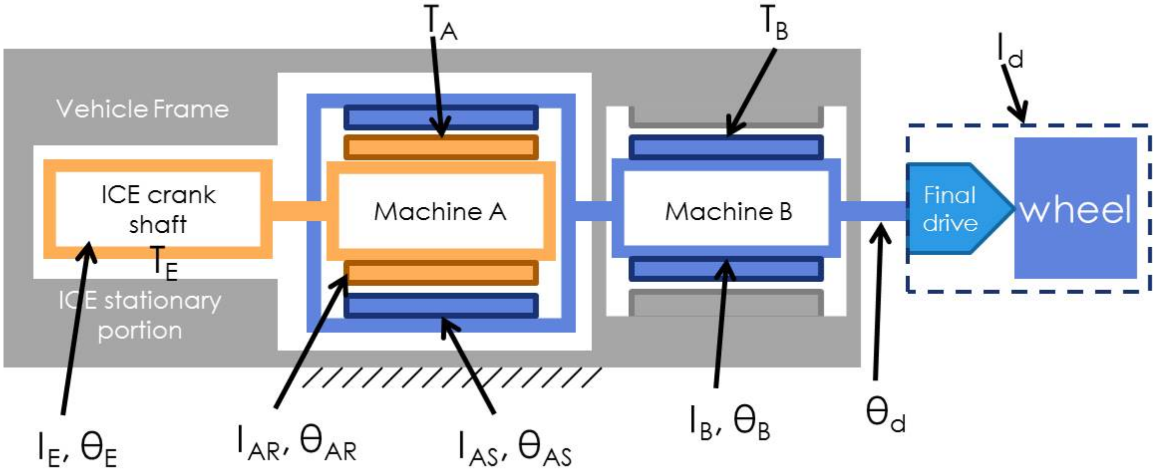

Figure 5.2: Novel configuration of powertrain contains an ICE, two electric machines (machine A and B), a battery pack (not shown in this drawing), and final transmission.

The ICE considered in this study is a $2.6L$, $350hp$ gasoline engine. The fuel rate can be obtained from the fuel map of the engine expressed as

$$\dot{m}_{E,i} = \dot{m}_E(T_{E,i}, \omega_{E,i}), \tag{5.2}$$

where $T_{E,i}$ is the torque created by the ICE of the i^{th} vehicle, and $\omega_{E,i}$ is the angular speed of the ICE.

Engine operations are bounded by angular speed and torque limits. Such boundaries can be expressed as

$$\begin{aligned} 0 \leq& \omega_{E,i} \leq \omega_{E,max}, \\ T_{E,min}(\omega_{E,i}) \leq& T_{E,i} \leq T_{E,max}(\omega_{E,i}). \end{aligned} \tag{5.3}$$

The optimal brake-specific fuel consumption (BSFC) curve is obtained to reduce the computational cost. The optimal BSFC curve indicates an ICE torque-angular velocity relationship. The curve can be expressed as

Table 5.1: Parameters in the dynamic equation governing the powertrain

Notation	Parameter
$I_{E,i}$	Rotational moment of inertia, crankshaft of ICE
$I_{AR,i}$	Rotational moment of inertia, rotor of machine A
$I_{AS,i}$	Rotational moment of inertia, stator of machine A
$I_{B,i}$	Rotational moment of inertia, rotor of machine B
$I_{d,i}$	Equivalent rotational moment of inertia, vehicle, pre-final-transmission
$\theta_{E,i}$	Angle of rotational, crankshaft of ICE
$\theta_{d,i}$	Equivalent angle of rotational, vehicle
$T_{E,i}$	Torque of ICE
$T_{A,i}$	Torque of machine A
$T_{B,i}$	Torque of machine B
$T_{r,i}$	Equivalent torque of road resistance

$$T_{E,i,opt}(\omega_{E,i}) = \underset{T_{E,i}}{\operatorname{argmin}} BSFC_i(T_{E,i}, \omega_{E,i}), \tag{5.4}$$

where

$$BSFC_i(T_{E,i}, \omega_{E,i}) = \frac{\dot{m}_{E,i}(T_{E,i}, \omega_{E,i})}{T_{E,i}\omega_{E,i}}. \tag{5.5}$$

Similar to the model of an ICE, the information needed to build a model for an electric machine includes an efficiency map and the speed-dependent torque limit. The efficiency map and torque limit are obtained using an electric machine scaling tool that was developed in the literature [151]. The efficiency map and torque limits are expressed as

$$\begin{aligned} \eta_{A,i} &= \eta_{A,i}(T_{A,i}, \omega_{A,i}), \\ \eta_{B,i} &= \eta_{B,i}(T_{B,i}, \omega_{B,i}), \end{aligned} \tag{5.6}$$

where $\eta_{A,i}$ and $\eta_{B,i}$ are the efficiencies of electric machines A and B for the i^{th} vehicle, respectively. The limits of the operating points for machine A and B are expressed as

$$\begin{aligned} \omega_{A,i,min} \leq& \omega_{A,i} \leq \omega_{A,i,max}, \\ T_{A,i,min}(\omega_{A,i}) \leq& T_{A,i} \leq T_{A,i,max}(\omega_{A,i}), \\ \omega_{B,i,min} \leq& \omega_{B,i} \leq \omega_{B,i,max}, \\ T_{B,i,min}(\omega_{B,i}) \leq& T_{B,i} \leq T_{B,i,max}(\omega_{B,i}). \end{aligned} \tag{5.7}$$

Here, the angular velocity of machine A, $\omega_{A,i}$ is defined as $\omega_{A,i} = \omega_{AR,i} - \omega_{AS,i}$, where $\omega_{AR,i} = \omega_{E,i}$ and $\omega_{AS,i} = \omega_{d,i}$. The total electric power for both electric machines in a powertrain is expressed as [142]

$$P_{bus,i} = T_{A,i}\omega_{A,i}\eta_{A,i}^{-\text{sign}(T_{A,i}\omega_{A,i})} + T_{B,i}\omega_{B,i}\eta_{B,i}^{-\text{sign}(T_{B,i}\omega_{B,i})}. \tag{5.8}$$

The battery current can be calculated as [78]

$$I_{b,i} = \frac{V_{oc,i} - \sqrt{V_{oc,i}^2 - 4P_{bus,i}R_{int,i}}}{2}, \tag{5.9}$$

where the open circuit voltage is $V_{oc,i} = V_{oc,i}(SOC_i)$, and the internal resistance of the battery is $R_{int,i} = R_{int,i}(SOC, \text{sign}(P_{bus,i}))$, with SOC_i being the state of charge (SOC) of the i^{th} battery.

The battery power and time derivative of the SOC are given by

$$P_{b,i} = I_{b,i}V_{oc,i}, \tag{5.10}$$

$$S\dot{O}C_i = \frac{I_{b,i}}{C_{b,i}}, \tag{5.11}$$

where $C_{b,i}$ is the capacity of the i^{th} battery.

5.2.2 Powertrain Control Algorithm

The powertrain control algorithm applied in this study is the adaptive ECMS. Adaptive ECMS is a near-optimal power management algorithm for electrified vehicles. The algorithm aims to minimize the total equivalent fuel, which contains the actual fuel consumption and a virtual fuel consumption that is converted from the battery energy. The power management problem can be written as [94]

$$\min_{T_{E,i}(t),T_{A,i}(t),T_{B,i}(t)} \int_{t=0}^{t_f} \dot{m}_{E,i} + p_i(SOC_i)C_{v,i}P_{b,i}\mathrm{d}t, \tag{5.12}$$

where $C_{v,i}$ is the conversion factor, $p_i(SOC_i)$ is the penalty function that limits battery SOC in a desired range, and t_f is the total time required for a platoon to complete a drive cycle. The fuel rate of an ICE ($\dot{m}_{E,i}$) and the battery power ($P_{b,i}$) depend on the battery SOC and on the torques and angular velocities of the ICE and electric machines (SOC_i, $T_{E,i}$, $T_{A,i}$, $T_{B,i}$, $\omega_{E,i}$, $\omega_{A,i}$, $\omega_{B,i}$).

The power management problem is constrained by powertrain equations of motion (Eqn. (5.1)) and by the relationship between the SOC and the operation of the electric machines. In addition, limits of angular velocities and torques of the ICE and electric machines apply. Another condition that needs to be satisfied is the consistency of the initial and final SOC, $SOC_i(t = 0) = SOC_i(t = t_f)$.

Both the conversion factor $C_{v,i}$ and the penalty function $p_i(SOC_i)$ have an impact on the final SOC by indicating the cost of electric power. The conversion factor is a constant that requires tuning to obtain consistency of initial and final SOC. The penalty function is a SOC-dependent penalty on conversion and helps maintain the SOC within a range. The penalty function in this study is adapted from [94] and is expressed as

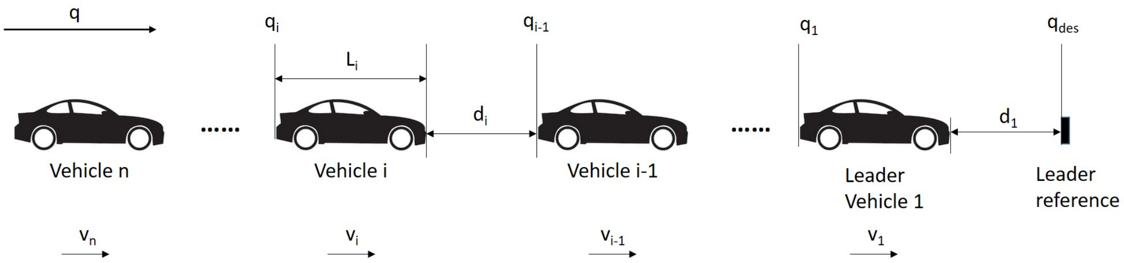

Figure 5.3: The configuration of the platoon contains leader vehicle and $n-1$ follower vehicles. Speeds of vehicles are v_i and the coordinate of the vehicle along the road is q_i. The leader reference has coordinate q_{des}. The headway for vehicle i is d_i.

$$p_i(SOC_i) = 1 - \left(2\frac{SOC_i - SOC_{des,i}}{SOC_{high,i} - SOC_{low,i}}\right)^3, \tag{5.13}$$

where $SOC_{des,i}$ is the desired state of charge that is between high and low SOC limits $SOC_{high,i}$ and $SOC_{low,i}$.

5.3 Platoon Dynamics and Vehicle Controllers

The platoon system contains the platoon dynamics and vehicle controllers. Longitudinal vehicle dynamics are considered in this study. The full vehicle dynamics are derived and linearized. The vehicle controllers are then designed using the linearized system.

5.3.1 Platoon Dynamics

The platoon configuration is illustrated in Fig 5.3. For an n-vehicle platoon, vehicle 1 is the leading vehicle, while vehicles 2 through n are following vehicles. The leading vehicle is following a leader reference that is a point moving exactly at the velocity that the drive schedule defines.

The platoon dynamics are expressed in state space. For an n-vehicle platoon, the state variables contain the headways and longitudinal velocities of all vehicles as

$$\mathbf{x}_s = [d_1, v_1, \cdots, d_i, v_i, \cdots, d_n, v_n]^T. \tag{5.14}$$

The platoon dynamics can be expressed as

$$\frac{d\mathbf{x}_s}{dt} = \frac{d}{dt}\begin{bmatrix} d_1 \\ v_1 \\ \vdots \\ d_i \\ v_i \\ \vdots \\ d_n \\ v_n \end{bmatrix} = \begin{bmatrix} v_{des} - v_1 \\ \frac{F_1 - R_1}{m_1} \\ \vdots \\ v_{i-1} - v_i \\ \frac{F_i - R_i}{m_i} \\ \vdots \\ v_{n-1} - v_n \\ \frac{F_n - R_n}{m_n} \end{bmatrix} = \mathbf{f}(\mathbf{x}_s, \mathbf{u}_s), \tag{5.15}$$

where $\mathbf{u}_s = [F_1, \cdots, F_i, \cdots, F_n]^T$ denotes the driving force generated by each vehicle. The driving forces are control inputs to the system. The mass of the vehicles are denoted by m_i, $i = 1, \ldots, n$. The road resistances for all vehicles are denoted as R_i, $i = 1, \ldots, n$. The resistance is expressed as

$$R_i(\mathbf{x}_s) = f_i m_i g \cos\theta_i + 1/2\rho_a C_{d,i}(1 - D_{R,i}(\mathbf{x}_s))A_i v_i^2 + m_i g \sin\theta_i. \tag{5.16}$$

Here f_i, m_i, g, $C_{d,i}$, A_i denote the coefficient of rolling resistance, the weight of vehicle, the gravitational acceleration, the aerodynamics drag coefficient, and the vehicle frontal area, respectively. The road grade is denoted by θ_i. The value of θ_i depends on the position of vehicle i. The variable ρ_a represents the density of air. The term $D_{R,i}$ is the aerodynamic drag reduction that is attributed from vehicles driving closely after one another in a platoon. A vehicle creates highly turbulent flow behind it, forming a wake propagation. The wake propagation reduces the drag that the following vehicles experience. The equations for drag reduction are derived experimentally in [122]. The equations for drag reduction for a two-vehicle platoon (leading vehicle and one following vehicle) can be expressed as

$$\begin{aligned} D_{R,1} &= C_{pb}, \\ D_{R,2} &= 1 - (1 - \epsilon_1)^2 (1 + C_{pf}), \end{aligned} \tag{5.17}$$

where

$$\begin{aligned} \epsilon_1 &= 1.05 C_{d,1}^{0.2} (1 - C_{pb})^{0.2} \left(\frac{v_0 h_{t,2}}{A_1^{1/2}} \right)^{-2/3}, \\ C_{pb} &= 1 - \left(1 - \left(\frac{6.3}{v_0 h_{t,2} + 6.3} \right)^3 \right)^2, \\ C_{pf} &= 97.124 (v_0 h_{t,2})^{-2.745}, \\ h_{t,2} &= \frac{d_2}{v_2}. \end{aligned}$$

The term A_1 represents the frontal area of the leading vehicle, and v_0 represents the constant velocity of the vehicles in the experiment to determine drag reduction. These equations are slightly modified from headway-dependent equations into headway-time-dependent equations, in order to adapt for platoons with time-varying speed.

The drag reductions for a three-vehicle platoon can be written as [122]

$$\begin{aligned} D_{R,1} &= C_{pb}, \\ D_{R,2} &= 1 - (1 - \epsilon_1)^2 (1 + C_{pf,1} - C_{pb,1}), \\ D_{R,3} &= 1 - (1 - \epsilon_2)^2 (1 + C_{pf,2})(1 - D'_{R,2}), \end{aligned} \tag{5.18}$$

where

$$\begin{aligned}
\epsilon_k &= 1.05 C_{d,k}^{0.2}(1 - C_{pb,k})^{0.2}\left(\frac{v_0 h_{t,k+1}}{A_k^{1/2}}\right)^{-2/3}, \\
C_{pb,k} &= 1 - \left(1 - \left(\frac{6.3}{v_0 h_{t,k+1} + 6.3}\right)^3\right)^2, \\
C_{pf,k} &= 97.124(v_0 h_{t,k+1})^{-2.745}, \\
h_{t,k+1} &= \frac{d_{k+1}}{v_{k+1}}, \quad k = 1, 2.
\end{aligned}$$

5.3.2 Linearization and Controller Design

The platoon dynamics contain nonlinear terms and some quantities that are hard to measure in real-time. For the purpose of developing vehicle controllers, linearization of the platoon dynamics with respect to a time-varying reference is performed. The platoon dynamics are written in a simplified form considering the aerodynamic drag reduction and resistance from road grade disturbances.

$$\frac{d\mathbf{x}_s}{dt} = \frac{d}{dt}\begin{bmatrix} d_1 \\ v_1 \\ \vdots \\ d_i \\ v_i \\ \vdots \\ d_n \\ v_n \end{bmatrix} = \begin{bmatrix} v_{des} - v_1 \\ \frac{F_1}{m_1} - \frac{R_{1,0}(v_1)}{m_1} \\ \vdots \\ v_{i-1} - v_i \\ \frac{F_i}{m_i} - \frac{R_{i,0}(v_i)}{m_i} \\ \vdots \\ v_{n-1} - v_n \\ \frac{F_n}{m_n} - \frac{R_{n,0}(v_n)}{m_n} \end{bmatrix} = \hat{\mathbf{f}}(\mathbf{x}_s, \mathbf{u}_s), \tag{5.19}$$

where

$$R_{i,0}(\mathbf{x}_s) = f_i m_i g + 1/2 \rho C_{d,i} A_i v_i^2. \tag{5.20}$$

To linearize the simplified dynamics with respect to a time-varying reference, the states and control inputs are decomposed into a summation of their errors and references as

$$\mathbf{x}_s = \begin{bmatrix} d_1 \\ v_1 \\ \vdots \\ d_i \\ v_i \\ \vdots \\ d_n \\ v_n \end{bmatrix} = \begin{bmatrix} \tilde{d}_1 \\ \tilde{v}_1 \\ \vdots \\ \tilde{d}_i \\ \tilde{v}_i \\ \vdots \\ \tilde{d}_n \\ \tilde{v}_n \end{bmatrix} + \begin{bmatrix} d_{1,ref} \\ v_{1,ref} \\ \vdots \\ d_{i,ref} \\ v_{i,ref} \\ \vdots \\ d_{n,ref} \\ v_{n,ref} \end{bmatrix} = \tilde{\mathbf{x}}_s + \mathbf{x}_{s,ref}, \tag{5.21}$$

$$\mathbf{u}_s = \begin{bmatrix} F_1 \\ \vdots \\ F_i \\ \vdots \\ F_n \end{bmatrix} = \begin{bmatrix} \tilde{F}_1 \\ \vdots \\ \tilde{F}_i \\ \vdots \\ \tilde{F}_n \end{bmatrix} + \begin{bmatrix} F_{1,ref} \\ \vdots \\ F_{i,ref} \\ \vdots \\ F_{n,ref} \end{bmatrix} = \tilde{\mathbf{u}}_s + \mathbf{u}_{s,ref}, \tag{5.22}$$

where $\tilde{\mathbf{x}}_s$ and $\tilde{\mathbf{u}}_s$ denote the errors of states and control inputs. The terms $\mathbf{x}_{s,ref}$ and $\mathbf{u}_{s,ref}$ represent the time-varying references of states and control inputs. To establish the error dynamics, the reference dynamics are defined. First, the reference headways for all vehicles are selected as

$$\begin{aligned} d_{1,ref} &= 0, \\ d_{i,ref} &= d_{i,0} + h_{des} v_{i,ref}, \end{aligned} \tag{5.23}$$

where h_{des} denotes a constant headway time which accounts for the need to increase the headway as the speed increases, and $d_{i,0}$ represents a constant headway at zero speed for all the following vehicles. Under this definition of reference headways, the leading vehicle is expected to follow the drive schedule exactly. For all following vehicles, the reference headways are velocity-dependent. Thus, the reference velocities for all following vehicles are not exactly the same but depend on the velocity defined by the drive schedule $v_{des}(t)$. Using both the definition of headways and the expression for desired headways, the reference velocities can be derived from the drive schedule. Therefore, all references can be determined using the reference dynamics as

$$\frac{d\mathbf{x}_{s,ref}}{dt} = \frac{d}{dt}\begin{bmatrix} 0 \\ v_{1,ref} \\ \vdots \\ d_{i,0} + h_{des}v_{i,ref} \\ v_{i,ref} \\ \vdots \\ d_{n,0} + h_{des}v_{n,ref} \\ v_{n,ref} \end{bmatrix} = \begin{bmatrix} v_{des} - v_{1,ref} \\ \frac{F_{1,ref}}{m_1} - \frac{R_{1,0}(v_{1,ref})}{m_1} \\ \vdots \\ v_{i-1} - v_{i,ref} \\ \frac{F_{i,ref}}{m_i} - \frac{R_{i,0}(v_{i,ref})}{m_i} \\ \vdots \\ v_{n-1} - v_{n,ref} \\ \frac{F_{n,ref}}{m_n} - \frac{R_{n,0}(v_{n,ref})}{m_n} \end{bmatrix}. \tag{5.24}$$

The reference velocity of the leading vehicle in Eqn. (5.24) is the same as that defined by the drive schedule. Note that in the reference dynamics, the reference of vehicle i is derived from the actual velocity of vehicle $(i-1)$ instead of its reference velocity. Such a way of deriving the reference velocity avoids potential collisions in case a large velocity error occurs with the front vehicle. However, such a definition of reference velocities can cause $\frac{d\mathbf{x}_s}{dt} \neq \hat{\mathbf{f}}(\mathbf{x}_{s,ref}, \mathbf{u}_{s,ref})$. This inconsistency becomes apparent in the final linearization. Thus, a residual function is defined as

$$\tilde{\mathbf{f}}(\tilde{\mathbf{x}}_s) = \frac{d\mathbf{x}_{s,ref}}{dt} - \hat{\mathbf{f}}(\mathbf{x}_{s,ref}, \mathbf{u}_{s,ref}). \tag{5.25}$$

The residual function in matrix form can be expressed as

$$\tilde{\mathbf{f}}(\tilde{\mathbf{x}}_s) = \mathbf{A}'\tilde{\mathbf{x}}_s, \tag{5.26}$$

where matrix $\mathbf{A}'$ is a $2n \times 2n$ matrix that contains mostly zeros, but a few ones in sub-diagonal terms as shown below

$$A'_{2i,2i-1} = 0, \quad i = 1, \ldots, n. \tag{5.27}$$

The error dynamics of the linearized platoon dynamics are expressed as

$$\frac{d\tilde{\mathbf{x}}_s}{dt} = -\mathbf{A}'\tilde{\mathbf{x}}_s + \left.\frac{\partial \hat{\mathbf{f}}}{\partial \mathbf{x}_s}\right|_{\mathbf{x}_{s,ref},\mathbf{u}_{s,ref}} \tilde{\mathbf{x}}_s + \left.\frac{\partial \hat{\mathbf{f}}}{\partial \mathbf{u}_s}\right|_{\mathbf{x}_{s,ref},\mathbf{u}_{s,ref}} \tilde{\mathbf{u}}_s. \tag{5.28}$$

The linearized platoon dynamics becomes a linear time-varying system and the state matrix $\mathbf{A}(t)$ and input matrix $\mathbf{B}(t)$ can be determined using Eqn. 5.28. The force commands are determined using LQR control as

$$\mathbf{u}_{s,c} = -\mathbf{K}\tilde{\mathbf{x}}_s + \mathbf{u}_{s,ref}, \tag{5.29}$$

where

$$\mathbf{K} = \mathrm{LQR}(\mathbf{A}(t), \mathbf{B}(t), \mathbf{Q}, \mathbf{R}). \tag{5.30}$$

Here, the $\mathbf{Q}$ and $\mathbf{R}$ are matrices that define the cost of errors of states and control inputs when determining the control gains using LQR control. The terms in these matrices are determined using the design variables in the optimization problem. The force commands $\mathbf{u}_{s,c}$ are transformed into angular acceleration commands as

$$\dot{\omega}_{d,i,com} = \frac{T_{d,i,com} - T_{r,i}}{I_{d,i}}, \tag{5.31}$$

where

$$\begin{aligned} T_{d,i,com} &= \frac{u_{s,i,c} r_{w,i}}{r_{f,i}}, \\ T_{r,i} &= \frac{r_{w,i} R_{i,0}}{r_{f,i}}. \end{aligned} \tag{5.32}$$

Here, the term $u_{s,i,c}$ is the i^{th} component of the force command $\mathbf{u}_{s,c}$. The tire radius is denoted as $r_{w,i}$. The torques of components in the powertrain are determined using the adaptive ECMS algorithm. The final control inputs, expressed in terms of torques of powertrain components, are

$$u_{s,i} = (\dot{\omega}_{d,i} I_{d,i} + T_{r,i}) \frac{r_{f,i}}{r_{w,i}}, \tag{5.33}$$

where

$$\begin{aligned}
\dot{\omega}_{d,i} &= \frac{T_{B,i} - T_{A,i} - T_{brk,i} - T_{r,i}}{I_{AS,i} + I_{B,i} + I_{d,i}}, \\
T_{brk,i} &= T_{B,i} - T_{A,i} - T_{d,i,com}, \quad \text{when} \quad T_{d,i,com} < 0, \quad T_{d,i,com} < T_{B,i} - T_{A,i}, \\
I_{d,i} &= \frac{2m_{w,i} + m_i}{\eta_{f,i}} \Big(\frac{r_{w,i}}{r_{f,i}}\Big)^2.
\end{aligned} \tag{5.34}$$

Here, $r_{f,i}$ and $\eta_{f,i}$ denote the ratio and efficiency of the final drive, respectively. The parameter $m_{w,i}$ represents the mass of a wheel. Note that the component torques are bounded by component sizes. Thus, the final force inputs may not be exactly the same as the force commands.

5.4 Platoon Optimization

5.4.1 Design Variables

The platoon optimization contains the drive schedule design and the vehicle controller design. The design variables are denoted as $\mathbf{x} = [\mathbf{x}_{DC}^T, \mathbf{x}_{CT}^T]^T$, where $\mathbf{x}_{DC}$ contains design variables that define the drive schedule, and the entries of $\mathbf{x}_{CT}$ are related to designing the $\mathbf{Q}$ and $\mathbf{R}$ matrices in the vehicle controllers in Eqn. (5.38). Details of these design variables are described in this section.

The design variables in $\mathbf{x}_{DC}$ are the desired velocities at the characteristic points between the initial position and the destination. The positions of the characteristic points $\mathbf{d}_{DC}$ are obtained using Chebychev sampling as

$$d_{DC,k} = \frac{d_{tot}}{2}\left(1 - \cos\left(\frac{2k-1}{2n_{DC}}\pi\right)\right), \quad k = 1, \ldots, n_{DC}. \tag{5.35}$$

Here, $d_{DC,k}$ is the k^{th} component in $\mathbf{d}_{DC}$. The constant n_{DC} is the number of characteristic points in the drive schedule design. Thus, n_{DC} is the length of both $\mathbf{x}_{DC}$ and $\mathbf{d}_{DC}$ vectors. The total distance of the road is denoted as d_{tot}.

The full drive schedule v_{des} as a function of distance d_{des} is expressed using piecewise cubic Hermite polynomial interpolation, using the characteristic velocities in $\mathbf{x}_{DC}$ and distances in $\mathbf{d}_{DC}$. Note that the characteristic distances in $\mathbf{d}_{DC}$ do not involve the initial and final position of the road. At these two positions, the desired velocities are always zero. Thus, the desired velocities at these two points are not design variables. The drive schedule as a function distance can be expressed as

$$v_{des}(t) = f_{DC}(d_{des}(t)). \tag{5.36}$$

Here, the drive schedule $v_{des}(t)$ and distance $d_{des}(t)$ are both functions of time. By definition, $v_{des}(t) = \frac{d}{dt}d_{des}(t)$. Thus, $v_{des}(t)$ and $d_{des}(t)$ can be obtained by solving

$$v_{des}(t) = \frac{\mathrm{d}}{\mathrm{d}t}d_{des}(t) = f_{DC}(d_{des}(t)). \tag{5.37}$$

The design variables in $\mathbf{x}_{CT}$ define the diagonal terms of the diagonal matrices $\mathbf{Q}$ and $\mathbf{R}$ in controller design as

$$\begin{aligned} Q_{j,j} &= x_{CT,j}, \quad j = 1, \ldots, 2n, \\ R_{k,k} &= x_{CT,2n+j}, \quad k = 1, \ldots, n. \end{aligned} \tag{5.38}$$

Note that index k is a dummy variable and is not the same as in Eqn (5.35). For an n-vehicle platoon, the length of $\mathbf{x}_{CT}$ is $3n$. Also, the length of $\mathbf{x}_{CT}$ is $3n$.

5.4.2 Cost Function and Constraints

The purpose of the platoon optimization is to minimize energy consumption while maintaining minimal error in headway keeping. Thus, the optimization problem can be written as

$$\underset{\mathbf{x}}{\text{minimize}} \quad J(\mathbf{x}) = \sum_{i=1}^{n} \int_{t=0} t_f P_{E,i} + P_{b,i} \mathrm{d}t + \alpha \sum_{i=1}^{n} \int_{t=0} t_f \tilde{d}_i^2 \mathrm{d}t, \tag{5.39}$$

subject to

$$\begin{aligned} &\mathbf{g}_a(\mathbf{x}_{DC}) \leq 0, \\ &g_t(\mathbf{x}_{DC}) \leq 0, \\ &\mathbf{g}_{bDC}(\mathbf{x}_{DC}) \leq 0, \\ &\mathbf{g}_{bCT}(\mathbf{x}_{CT}) \leq 0, \end{aligned} \tag{5.40}$$

where $\mathbf{g}_a(\mathbf{x}_{DC})$ contains acceleration constraints on drive schedule velocities at characteristic points, which can be expressed as

$$g_{a,k} = \left| \frac{x_{DC,k+1}^2 - x_{DC,k}^2}{2(d_{DC,k+1} - d_{DC,k})} \right| - a_{max}. \tag{5.41}$$

where the maximum acceleration a_{max} is a value chosen by the designer.

The g_t constraint ensures the time the platoon requires to reach the destination is not longer than a defined time t_{max}. The function g_t is expressed as

$$g_t(\mathbf{x}_{DC}) = \int_{d=0}^{d_{tot}} \frac{\mathrm{d}d_{des}}{v_{des}} - t_{max}. \tag{5.42}$$

Note that g_t depends on $\mathbf{x}_{DC}$ because d_{des} and v_{des} depend on $\mathbf{x}_{DC}$.

The last two constraints $\mathbf{g}_{bDC}(\mathbf{x}_{DC})$ and $\mathbf{g}_{bCT}(\mathbf{x}_{CT})$ define upper and lower boundaries of all design variables.

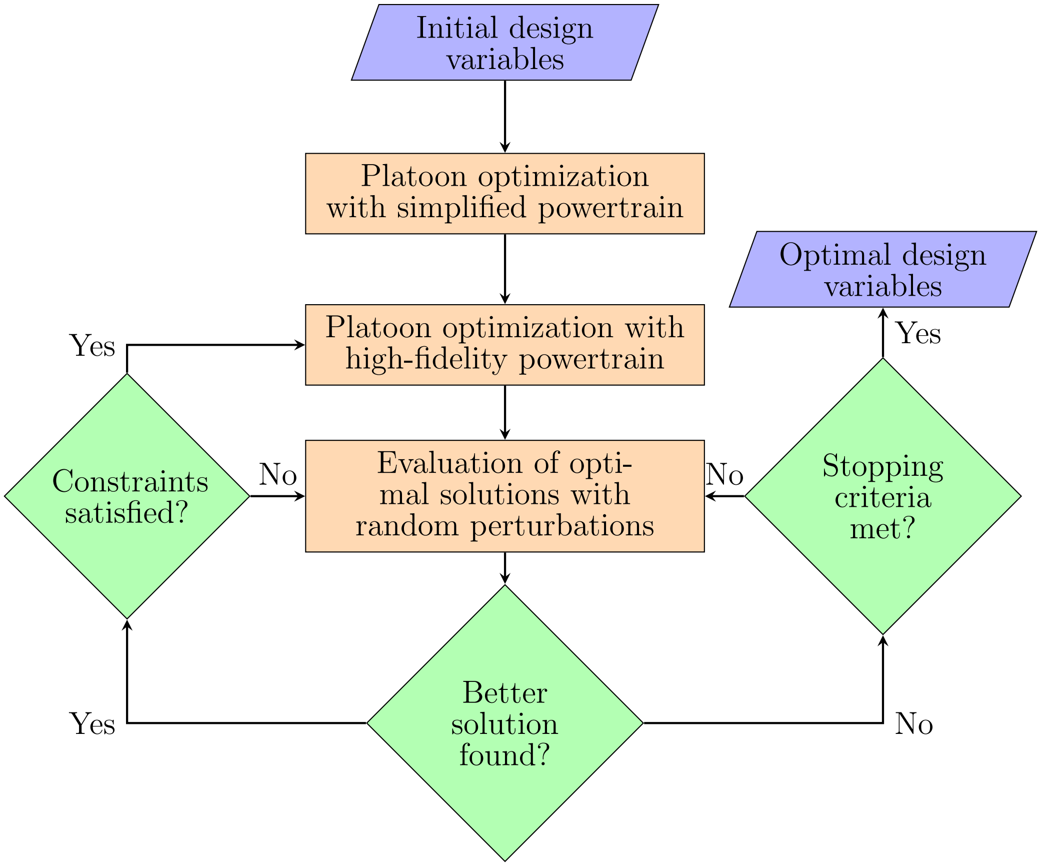

Figure 5.4: A problem-specified optimization process is designed, combining optimization with both simplified and high-fidelity model, and random perturbations to avoid narrow/local optimal solution.

5.4.3 Design of Procedures for Platoon Optimization

A high-fidelity model was created and contains the powertrain operations and controls as shown in Sec. 5.2. The platoon optimization using this high-fidelity model requires a high computational cost. To speed up the computation, a series of problem-associated optimization procedures were designed. These procedures are illustrated in Fig. 5.4.

The idea for designing these procedures is to speed up the first steps of optimization using a simplified model. In the simplified model, the high-fidelity powertrain model is replaced by vehicle power limits. The optimal solution from optimization with the simplified model becomes the initial solution in the next optimization using the high-fidelity model. Random perturbations are applied to the optimization results obtained using the high-fidelity model to avoid the algorithm being trapped in narrow local optimal solutions. Only the random perturbations on the local optimal solution that lead to a smaller cost value and satisfy all constraints at the same time are stored. The optimal solution with the stored random perturbations becomes the initial solution in the new optimization. Once applying random perturbations to the local optimal solution does not yield a better performance of the platoon after a certain number of sampling iterations, the process ends and the current optimal solution is considered the final (and optimal) solution.

5.5 Results

The optimization framework enables the study of various platoons by allowing flexibility in selecting vehicle and powertrain component sizes. A homogeneous and a heterogeneous platoon are studied using the framework. A homogeneous platoon contains identical vehicles, while various vehicles can form a heterogeneous platoon. Parametric studies are proviced in this section for both platoons.

The upper and lower bounds for each desired velocity in $\mathbf{x}_{DC}$ are 100 m/s and 0 m/s, respectively. The upper and lower bounds for each controller parameter in $\mathbf{x}_{CT}$ are 10^3 and 10^{-1}. The maximum acceleration a_{max} is 3 m/s^2. The threshold number of iterations in applying random perturbations is 500.

5.5.1 Parametric Study of a Homogeneous Platoon

The parametric study is enabled with the optimization framework with high fidelity model that has been designed and implemented. In this section, a parametric study on the headway is demonstrated. A homogeneous platoon with 2 vehicles is considered. The vehicle and powertrain parameters are listed in Tab 5.2.

Notation	Value	Notation	Value
m_i	2,300 kg	ρ_a	1.2 kg/m^3
A_i	6.97 m^2	$C_{d,i}$	0.36
f_i	0.015	$P_{Ar,i}$	120 kW
g	9.81 m/s^2	$T_{Ar,i}$	300 N
$m_{w,i}$	10 kg	$P_{Br,i}$	120 kW
$r_{t,i}$	0.4 m	$T_{Br,i}$	300 N
$r_{f,i}$	7	$V_{br,i}$	600 V
$\eta_{f,i}$	0.96	$C_{br,i}$	5 Ah

Table 5.2: Parameters used in the homogeneous platooning problem.

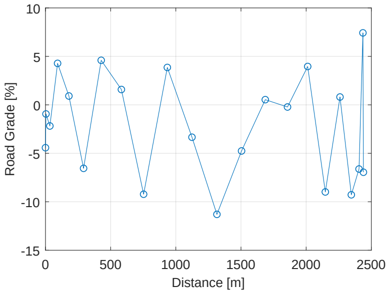

Figure 5.5: The road grade is defined at characteristic positions and linearly interpolated in between.

The parameter being explored here is the constant component in reference headway, or $d_{2,0}$. The selected values of $d_{2,0}$ are 3 m, 10 m, and 30 m.

The total distance of the road is 2,439.3 m. The road grade is defined at characteristic points and linearly interpolated at other locations, as shown in Fig 5.5. The road grade is randomly generated to match the pattern of the measured data for actual roads in the United States [137].

The initial drive schedule in the optimization problem is a constant-speed drive cycle. The desired velocities at the initial position and the destination are both zero. Thus, such a drive schedule contains acceleration, constant speed driving, and deceleration, where the acceleration and deceleration at both ends of the drive schedule satisfy the acceleration constraints. The initial and final drive schedule in the optimizations are illustrated in Fig 5.6. The intermediate results in the optimization

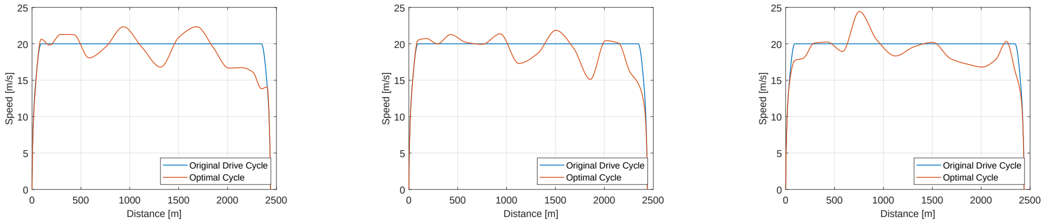

(a) (b) (c)

Figure 5.6: The optimal drive schedule depends on the constant component of reference headway $d_{2,0}$. Optimal drive schedules are shown above for (a) $d_{2,0} = 3\ m$, (b) $d_{2,0} = 10\ m$, and (c) $d_{2,0} = 30\ m$.

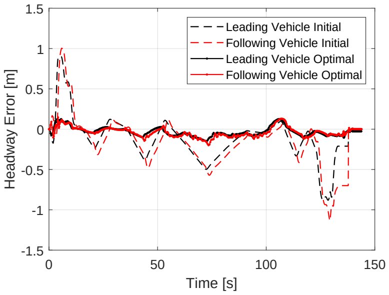

Figure 5.7: The headway keeping errors of both leading and following vehicles are smaller with the optimized vehicle controller compared to initial controller. Control optimization reduces the maximum headway-keeping error from over $1.0[m]$ to less than $0.2[m]$.

process are not shown in the figure for clarity.

The initial design variables for vehicle controllers are selected as $\mathbf{x}_{CT,init} = [10, 10, 10, 10, 100, 100]$ To illustrate the effectiveness of vehicle control optimization, the headway-keeping errors of both vehicles in platoon with initial and optimal controllers are shown in Fig 5.7. The constant component of reference headway is 10 m for the results that are shown in the figure.

The headway-keeping errors become smaller when the control is optimized. With optimal controllers, the component of the cost that comes from the headway keeping error is significantly reduced from that of the initial controller.

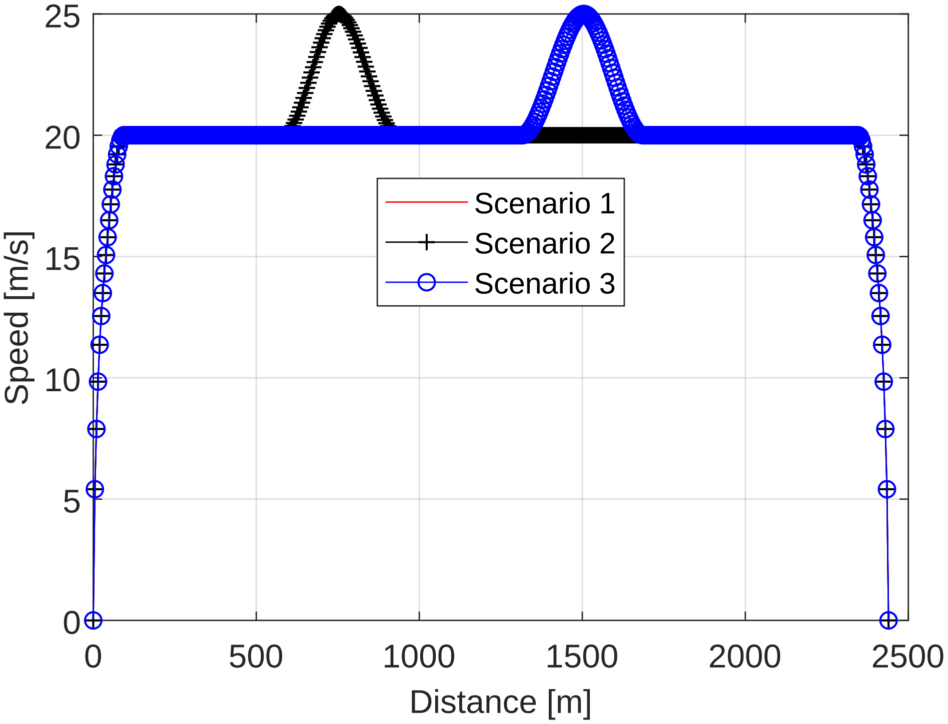

Figure 5.8: The drive schedules in the three scenarios are illustrated. The drive schedule in baseline scenario 1 is a constant speed schedule without any peaks. The other two drive schedules contain each one a peak at different locations.

In the optimal drive schedule, when $d_{2,0} = 30\ m$, the peak of the vehicles' velocity is near 750 m, instead of 1,500 m in the other cases where the desired headway is smaller. To validate the peak shift at high intravehicular distancing, three different drive schedule scenarios were designed, as shown in Fig 5.8. The three drive schedules contain scenario 1 as a baseline design, which is a constant speed drive schedule at 20 m/s. In the other two drive schedules, a single velocity peak is added at the characteristic position close to 750 m in scenario 2 and at 1,500 m in drive schedule 3, respectively. The scenarios are created to study the impact of the location of the velocity peak on energy consumption when $d_{2,0} = 30\ m$.

For each of these drive schedules, the same platoon with the same vehicle controllers is evaluated. The vehicle controllers in all scenarios are optimal controllers for $d_{2,0} = 30\ m$. The resulting energy consumption is summarized in Tab 5.3. The initial and optimal costs in all cases in this parametric study are summarized in Tab 5.4.

Scenario	**Energy Consumption**
2	7.132 MJ
3	7.232 MJ

Table 5.3: The energy consumption in scenario 2 is smaller than that in scenario 3, indicating higher energy efficiency of early peak when $d_{2,0} = 30\ m$.

The results suggests that when $d_{2,0} = 30\ m$, a velocity peak near 750 m can result in slightly lower energy consumption compared to the peak near 1,500 m, given the specific road grade in this study of headway.

Constant Headway	**Initial Cost**	**Optimal Cost**	**Cost Reduction**
3 m	5.561 MJ	4.520 MJ	18.7%
10 m	6.376 MJ	5.280 MJ	17.4%
30 m	6.910 MJ	5.523 MJ	20.1%

Table 5.4: Energy reductions are observed in all reference constant headway settings.

The total energy consumption of multiple vehicles that drive through a specified path is reduced due to two factors, namely the drive schedule and vehicle controller improvement, and platoon formation. Applying either of these factors, or a combination of both, can save energy. The optimal results obtained in this study are taking advantage of both optimization and platoon formation to save energy.

The effectiveness of the factors are evaluated by establishing four cases with different $d_{2,0}$ values. Case 1 is a baseline case, with decoupled vehicles driving through the constant speed drive schedule (initial drive schedule in optimization) with non-optimal vehicle controllers. The other three cases modify the setup in the baseline case to highlight the effects of the two energy saving factors. In case 2, the drive schedule and vehicle controllers are replaced by the final optimal design. Note that, in case 2, the vehicles are still decoupled. Thus, the final drive schedule and vehicle

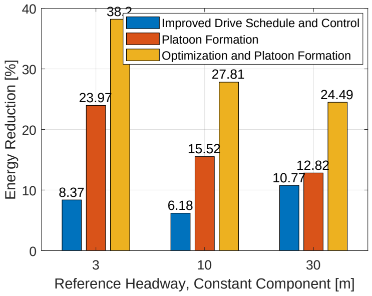

Figure 5.9: Percentage energy savings of cases 2 to 4 compared with the baseline case are summarized to evaluate the effectiveness of two factors on reducing energy consumption. The two factors in combination can save over 20% of energy for a two-vehicle homogeneous platoon.

controller design for a platoon is not necessarily optimal, but improved compared to the initial drive schedule and vehicle controllers. In case 3, the coupling of vehicles is considered while the drive schedule and vehicle controllers remain the same as in case 1. Case 4 contains the platoon driving through the final drive schedule with the optimal controllers, which is the overall optimal solution. The percentage energy reductions by comparing cases 2 through 4 to the baseline case for all $d_{2,0}$ values are summarized in Fig 5.9.

The energy saving is over 20% when both optimization and platoon formation are applied. Such saving can be close to 40% when the headway is smaller. A significant part of the energy reduction within cases 3 and 4 compared to the baseline case 1 is from platoon formation. The energy saving through platoon formation is obtained through drag reduction, which is headway-dependent. Thus, the longer the headway, the smaller these energy reductions are, and the weaker the effect the platoon formation has on energy saving.

5.5.2 Parametric Study of a Heterogeneous Platoon

A 3-vehicle heterogeneous platoon is defined and implemented. The three vehicles are referred to as light, medium, and heavy vehicles according to their weight. The vehicle and component-level parameters are shown in Tab 5.5.

Notation	**Heavy Vehicle**	**Medium Vehicle**	**Light Vehicle**
m_i	3,000 kg	2,300 kg	1,600 kg
A_i	4.32 m^2	6.97 m^2	2.20 m^2
f_i	0.015	0.015	0.015
$m_{w,i}$	10 kg	10kg	7.5 kg
$r_{t,i}$	0.400 m	0.400 m	0.287 m
$r_{f,i}$	10.0	7.0	7.0
$\eta_{f,i}$	0.96	0.96	0.96
$C_{d,i}$	0.57	0.36	0.29
$P_{Ar,i}$	200 kW	120 kW	60 kW
$T_{Ar,i}$	500 N	300 N	200 N
$P_{Br,i}$	200 kW	120 kW	60 kW
$T_{Br,i}$	500 N	300 N	200 N
$V_{br,i}$	600 V	600 V	400 V
$C_{br,i}$	10 Ah	5 Ah	5 Ah

Table 5.5: Parameters of vehicles in the heterogeneous platoon.

The purpose of this study is to explore the effects of the order of vehicles in the 3-vehicle platoon. The vehicle orders in the heterogeneous platoon are defined in Tab 5.6.

Order	**Leading Vehicle**	**Following Vehicle 1**	**Following Vehicle 2**
1	Heavy	Medium	Light
2	Heavy	Light	Medium
3	Medium	Heavy	Light
4	Medium	Light	Heavy
5	Light	Heavy	Medium
6	Light	Medium	Heavy

Table 5.6: Order of vehicles in the heterogeneous platoon.

The initial drive schedule in this study is the 20 m/s constant speed drive schedule like in homogeneous platoon optimizations. The initial design variables for vehicle controllers are $\mathbf{x}_{CT,init} = [10, 10, 10, 10, 10, 10, 100, 100, 100]^T$. The initial and final cost of the optimization for platoons in all orders are listed in Tab. 5.7. The initial and final drive schedules are summarized in Fig. 5.10.

In this study, the drive schedule and vehicle controller optimization is able to

Order	Initial Solution	Optimal Solution	Improvement
1	14.20 MJ	10.43 MJ	26.6%
2	13.17 MJ	09.06 MJ	31.2%
3	14.54 MJ	09.17 MJ	37.0%
4	12.33 MJ	09.49 MJ	23.0%
5	13.30 MJ	08.36 MJ	37.2%
6	13.20 MJ	09.67 MJ	26.7%

Table 5.7: Significant energy reductions are observed within the heterogeneous platoon for all vehicle orders.

reduce the energy consumption for the 3-vehicle heterogeneous platoon in all orders. The energy reductions are over 20% for vehicles in all orders.

The effectiveness of energy saving from two factors are presented in Fig. 5.11. These two factors contain the improvement of the drive schedule and vehicle controller design, and the platoon formation.

The order of vehicles can impact the inter-vehicular coupling, which leads to differences in resistances and force demands for each vehicle. In an optimization process, the boundaries on powertrain components are activated and affect the optimization results. Focusing on the optimal solution for order 6, the torque of machine B in the light vehicle (leading vehicle in this case) and the battery SOC is shown in Figs. 5.12 and 5.13. All torque constraints, including those for ICE and both electric machines, for each vehicle are hard constraints. The constraints on battery SOC, on the other hand, are soft constraints. The desired range for SOC is defined, and the cost of electrical energy is penalized as shown in Eqn. 5.13.

5.6 Conclusions

Platooning of electrified vehicles can improve vehicle performance by enhancing energy efficiency and safety. The control algorithm and sizes of components can impact the performance of the platoon. In this study, a system-level optimization of the drive schedule and vehicle control for platoons of electrified vehicles was designed.

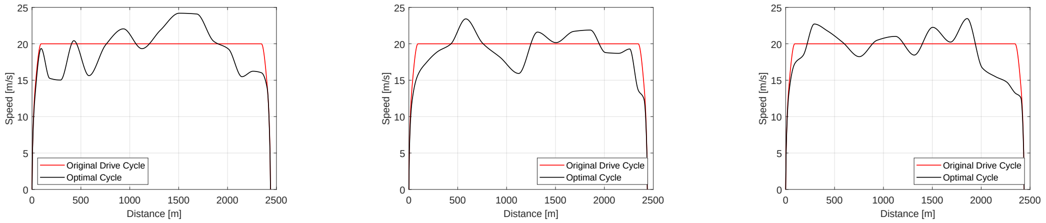

(a) Order 1 (b) Order 2 (c) Order 3

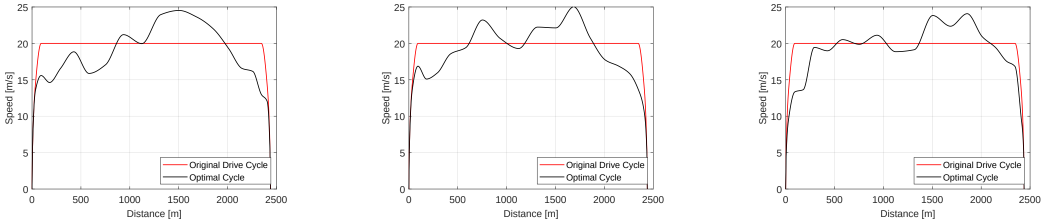

(d) Order 4 (e) Order 5 (f) Order 6

Figure 5.10: Initial and optimal drive schedules for all vehicle orders of the three-vehicle heterogeneous platoon are presented. The optimal drive schedules show similar behaviors because the road grade is the same in all cases.

A high-fidelity modeling and optimization framework was implemented considering vehicle dynamics, powertrain controls and operations. Parametric studies for both homogeneous and heterogeneous platoons were implemented using the high-fidelity optimization framework to explore parameters that can impact platoon efficiencies. The results of these optimizations and energy comparisons suggest that optimization of drive schedule and vehicle control can lead to significant reduction in energy consumption for vehicles on a specific path without compensation on the duration of the drive schedule. The effectiveness of the optimization for energy saving is comparable or even higher than that of the formation of the platoon. Validations of results were designed and revealed the impact of powertrain operations and component-level power limits on the optimization and platoon-level energy efficiency.

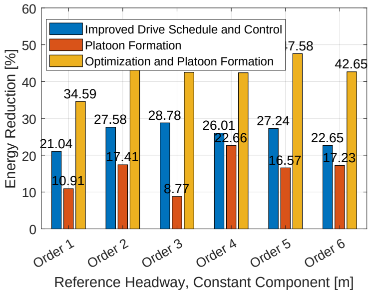

Figure 5.11: Percentage energy savings suggest higher significance of drive schedule and vehicle control improvement than platoon formation in energy saving for a three-vehicle heterogeneous platoon. The combination of both factors can lead to over 40% energy reduction in some cases.

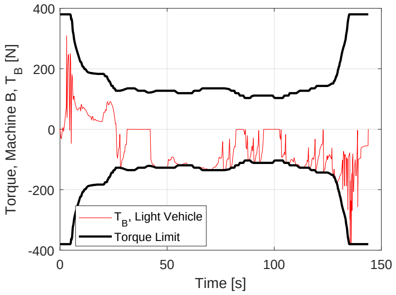

Figure 5.12: Torque constraint for machine B in the light vehicle is activated in several occasions in the optimal solution for vehicle order 6.

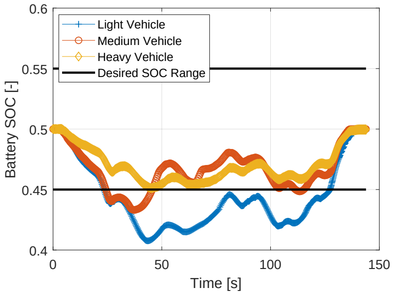

Figure 5.13: The soft SOC constraints for all vehicles in the platoon penalize the SOC change from the initial SOC value, through varying the cost of electrical energy.

CHAPTER VI

Conclusions and Contributions

In this dissertation, multiple topic have been covered. To summarize, the topics include building the multi-physics ROM for EMS coupling, design and model of a novel hybrid electric powertrain architecture, design and control optimization of the novel powertrain, and platooning of electrified powertrain.

The multi-physics ROM targets at a key component in electrified powertrains, the electric machine. This modeling method innovatively suggested the model of the coupling between electromagnetic force and the structural motion. The model turned out to be a system under parametric excitation, in the form of damped Mathieu's equation. The stability of damped Mathieu's equation was revisited. The threshold values for amplitude of parametric excitation that separates stable and unstable regions were derived. Two versions of multi-physics ROMs were developed, including the ROM with linearized force and nonlinear force. Using the multi-physics ROM and the results of stability We were able to find the parametric resonances on a proof-of-concept design. Frequency domain responses showed that the parametric resonance could occur in electric machines and other electromagnetic devices. In addition, a shift and amplification of the primary resonance that is caused by force harmornic could occur due to the softening effect of a constant component of the parametric excitation of the electric machine. Eventually, time-domain analyses verified the simulation results from the ROM.

The design of the novel hybrid electric powertrain in this work was inspired by the idea of efficiently removing the torque fluctuation from the smaller ICEs that are usually applied for HEVs. The design allows the stator of one electric machine to rotate, so that no clutches or planetary gears are needed. In addition, the architecture allows flexible operation for the ICE. A multi-state rule-based controller have been developed to prove the functions of the novel powertrain. The electric machines, which are designed for specific purposes, are able to acrry out their functionality successfully. Overall, the torque fluctuation is removed and the AC energy associated with that can be efficiently recovered. At the same time, the controller showed comparable performance to other existing HEV powertrains.

The architecture of novel powertrain was designed and the first model proved its functionalities. However, a fuel economy analysis suggested that by either resizing the components or replace the rule-based controller with a optimal controller, improvements in fuel efficiency were observed. Thus, the design and control optimization is necessary in order to improve the newly designed architecture and find the benchmark performance. Nested approach is applied for the coupled design and control optimization for the novel powertrain. Sequential quadratic programming was applied in the outer loop while the ECMS was employed in the inner loop. A polynomial surrogate model that approximates the ECMS calculation was designed and built lower computation cost in the optimization problem. The physics-based models for the components were built, as oppose to the look-up table model in similar studies. The optimization is designed as a multi-objective problem. Approach of forming single utility function is designed using the Pareto front of the novel powertrain. Multiple optimal powertrain designs can be selected by assigning different relative weight to individual objectives. Numerous commercially available HEV powertrains are selected as benchmark powertrains. The benchmark powertrains are evaluated and optimized.

The optimal results of novel powertrain and benchmark powertrains are compared under different weight selection in single utility function. The novel powertrain shows comparable or better fuel economy to benchmark powertrains. Similarities and differences between functionalities of components in novel powertrain and benchmark powertrains are detected.

Platooning problem in this study focused on optimizing the drive cycle, in order to minimize the energy consumption when a platoon of electrified vehicles are moving through a certain distance, while maintaining the headway keeping quality. The platooning problem in this study takes account of the powertrain operation and the impact of powertrain status on platoon performance. The drive cycle and vehicle controllers are optimized to minimize the energy consumption for a platoon on a specified task. The performance of platoon is evaluated using high-fidelity platoon model. A three-level optimization problem was formulated, including optimization, platoon dynamics and vehicle control, and powertraion subsystem. Platoon dynamics are investigated and vehicle controllers are designed and developed. The driver is designed as a model that takes account of inter-vehicular communication, perceptions, and predictions. High-fidelity hybrid powertrain model with near-optimal adaptive ECMS power management is implemented. The optimization framework enables the study of different types of platoons. Homogeneous and heterogeneous platoons are investigated in this dissertation. Parametric studies are designed and completed for both types of platoons. The results suggested a significant drop in headway keeping error and energy consumption for all platoons after optimization.

CHAPTER VII

Future Work

Multi-physics ROM for system with EMS coupling is implemented in this dissertation. The ROM is able to reduce computation time significantly compared to full-order FEA time marching simulations. The method can be improved by applying strucural symmetry. The symmetry can further reduce the computational cost by approximately one order of magnitude. The basic ideas of EMS ROM can be extended to other multi-physics system, like battery or fuel cell where chemical-structural interactions occur.

A major improvement that could happen to HEV powertrain is on vehicle control. The existing optimal and near optimal power management strategies require solving in discretized time domain in practice. In addition, the number operating points to select is finite. The discretization in time and control space lead to imperfect boundary condition satisfaction. This results in nonsmoothness of energy-related powertrain performance with respect to design variables of powertrain. Such nonsmoothness has caused some issues in the research area of HEVs. Current solutions usually contain relaxing the boundary condition to tolerate the nonsmoothness. However, such method do not eliminate the nonsmoothness in powertrain evaluation. Methods like surrogate model could potentially resolve the issue. The format of the surrogate model could be improved from the polynomial model in this dissertation.

Optimization-based control like optimal powertrain control strategies and Lyapunov like control can be applied as baseline controls to develop data-driven control strategy. Due to the wide adaptivity of optimal control methods, the control strategy can potentially be applied on but not limited to powertrains and vehicles.

Limitations and challenges remain on platooning problem. The optimization problem is a high-dimension problem with hundreds of design variables. The cost function for the drive cycle optimization is a result of a complete time domain simulation. Such simulation goes through a optimization process to determine powertrain component operation. Approach that speeds up the platoon evaluation can be valuable.

The study of platooning can be extended to more vehicle motions, such as lateral motion. More vehicle motions means more dimensions in the environment that the vehicle is travelling on. When platooning problem is extended to 2D or 3D space, the optimization problem become a subset of motion planning problem, but with powertrain operation as constrains. The high-fidelity platoon modeling and longitudinal planning framework in this dissertation can be extended to integrate with path planning problem.

APPENDIX

APPENDIX A

Optimal Powertrain Designs and Their Performance

Table A.1: Optimal designs for benchmark powertrain 1 (BP1)

	Optimal Design 1		**Optimal Design 2**	
Variable	**Original**	**Rounded**	**Original**	**Rounded**
α	1 mpg	1 mpg	2 mpg	2 mpg
P_{Ar}	58.26 kW	60.00 kW	49.33 kW	50.00 kW
T_{Ar}	233.6 Nm	230.0 Nm	323.6 Nm	320.0 Nm
P_{Br}	79.99 kW	80.00 kW	73.70 kW	75.00 kW
T_{Br}	233.4 Nm	230.0 Nm	327.1 Nm	330.0 Nm
r_f	1.760	1.760	2.709	2.709
V_b	220.9 V	221.0 V	203.4 V	203.0 V
C_b	11.34 Ah	11.00 Ah	11.15 Ah	11.00 Ah
$J_f(-F_{e,cb})$	-64.42 mpg	-64.21 mpg	-62.88 mpg	-62.31 mpg
J_c	18.60	18.58	17.15	17.20

Table A.2: Optimal designs for benchmark powertrain 2 (BP2)

	Optimal Design 1		**Optimal Design 2**	
Variable	**Original**	**Rounded**	**Original**	**Rounded**
α	1 *mpg*	1 *mpg*	2 *mpg*	2 *mpg*
P_{Ar}	44.15 *kW*	45.00 *kW*	46.27 *kW*	45.00 *kW*
T_{Ar}	349.9 *Nm*	350.0 *Nm*	298.3 *Nm*	300.0 *Nm*
P_{Br}	72.73 *kW*	75.00 *kW*	43.23 *kW*	45.00 *kW*
T_{Br}	216.5 *Nm*	220.0 *Nm*	288.3 *Nm*	290.0 *Nm*
r_f	1.985	1.985	2.476	2.476
V_b	238.2 *V*	238.0 *V*	224.6 *V*	225.0 *V*
C_b	10.51 *Ah*	11.00 *Ah*	11.66 *Ah*	12.00 *Ah*
$J_f(-F_{e,cb})$	-59.80 *mpg*	-59.64 *mpg*	-57.26 *mpg*	-57.25 *mpg*
J_c	17.45	17.82	15.90	16.07

Table A.3: Optimal designs for benchmark powertrain 3 (BP3)

	Optimal Design 1		**Optimal Design 2**	
Variable	**Original**	**Rounded**	**Original**	**Rounded**
α	1 *mpg*	1 *mpg*	2 *mpg*	2 *mpg*
P_{Ar}	52.45 *kW*	50.00 *kW*	57.62 *kW*	60.00 *kW*
T_{Ar}	223.3 *Nm*	220.0 *Nm*	397.6 *Nm*	400.0 *Nm*
P_{Br}	48.46 *kW*	50.00 *kW*	42.33 *kW*	40.00 *kW*
T_{Br}	276.9 *Nm*	280.0 *Nm*	151.8 *Nm*	150.0 *Nm*
r_f	2.249	2.249	2.666	2.666
V_b	211.1 *V*	211.0 *V*	210.7 *V*	211.0 *V*
C_b	12.73 *Ah*	13.00 *Ah*	10.83 *Ah*	11.00 *Ah*
$J_f(-F_{e,cb})$	-54.88 *mpg*	-54.85 *mpg*	-53.46 *mpg*	-53.43 *mpg*
J_c	16.65	16.70	15.84	15.91

Table A.4: Optimal designs for benchmark powertrain 4 (BP4)

	Optimal Design 1		**Optimal Design 2**	
Variable	**Original**	**Rounded**	**Original**	**Rounded**
α	1 *mpg*	1 *mpg*	2 *mpg*	2 *mpg*
P_{Ar}	44.72 *kW*	45.00 *kW*	40.48 *kW*	40.00 *kW*
T_{Ar}	352.3 *Nm*	350.0 *Nm*	224.1 *Nm*	220.0 *Nm*
P_{Br}	54.14 *kW*	55.00 *kW*	51.06 *kW*	50.00 *kW*
T_{Br}	353.1 *Nm*	350.0 *Nm*	226.5 *Nm*	230.0 *Nm*
r_f	2.433	2.433	3.210	3.210
V_b	244.1 *V*	244.0 *V*	212.0 *V*	212.0 *V*
C_b	15.50 *Ah*	15.00 *Ah*	13.26 *Ah*	13.00 *Ah*
$J_f(-F_{e,cb})$	-60.20 *mpg*	-59.33 *mpg*	-58.86 *mpg*	-58.71 *mpg*
J_c	18.50	18.36	16.32	16.13

BIBLIOGRAPHY

BIBLIOGRAPHY

[1] Ahn, K., and P. Papalambros (2009), Engine optimal operation lines for power-split hybrid electric vehicles, *Proceedings of the Institution of Mechanical Engineers, Part D: Journal of Automobile Engineering*, *223*(9), 1149–1162, doi: 10.1243/09544070JAUTO1124.

[2] Al-Aawar, N., and A. R. A. Arkadan (2015), Optimal control strategy for hybrid electric vehicle powertrain, *IEEE Journal of Emerging and Selected Topics in Power Electronics*, *3*(2), 362–370, doi:10.1109/JESTPE.2014.2323019.

[3] Alam, A., B. Besselink, V. Turri, J. Martensson, and K. H. Johansson (2015), Heavy-duty vehicle platooning for sustainable freight transportation: A cooperative method to enhance safety and efficiency, *IEEE Control Systems Magazine*, *35*(6), 34–56, doi:10.1109/MCS.2015.2471046.

[4] Alam, A., J. Mårtensson, and K. H. Johansson (2015), Experimental evaluation of decentralized cooperative cruise control for heavy-duty vehicle platooning, *Control Engineering Practice*, *38*, 11–25, doi:10.1016/j.conengprac.2014.12.009.

[5] Alvarez, L., and R. Horowitz (1999), Safe platooning in automated highway systems part i: Safety regions design, *Vehicle System Dynamics*, *32*(1), 23–55, doi:10.1076/vesd.32.1.23.4228.

[6] Barraquand, J., and J. C. Latombe (1993), Nonholonomic multibody mobile robots: Controllability and motion planning in the presence of obstacles, *Algorithmica*, *10*(2-4), 121–155, doi:10.1007/bf01891837.

[7] Bayrak, A., Y. Ren, and P. Papalambros (2013), *Design of hybrid-electric vehicle architectures using auto-generation of feasible driving modes*, vol. 1, American Society of Mechanical Engineers, doi:10.1115/DETC2013-13043.

[8] Bayrak, A., N. Kang, and P. Papalambros (2016), Decomposition-based design optimization of hybrid electric powertrain architectures: Simultaneous configuration and sizing design, *Journal of Mechanical Design - Transactions of the ASME*, *138*(7), doi:10.1115/1.4033655.

[9] Bayrak, A. E., Y. Ren, and P. Y. Papalambros (2013), Design of hybrid-electric vehicle architectures using auto-generation of feasible driving modes, in *Volume 1: 15th International Conference on Advanced Vehicle Technologies; 10th International Conference on Design Education; 7th International Conference*

on Micro- and Nanosystems, American Society of Mechanical Engineers, doi: 10.1115/detc2013-13043.

[10] Bayrak, A. E., Y. Ren, and P. Y. Papalambros (2014), Optimal dual-mode hybrid electric vehicle powertrain architecture design for a variety of loading scenarios, in *Volume 3: 16th International Conference on Advanced Vehicle Technologies; 11th International Conference on Design Education; 7th Frontiers in Biomedical Devices*, American Society of Mechanical Engineers, doi:10.1115/ detc2014-34897.

[11] Bergenheim, C., S. Shladover, and E. Coelingh (2012), Overview of platooning systems, in *Proceedings of the 19th ITS World Congress, Vienna, Austria.*

[12] Bergenhem, C., E. Hedin, and D. Skarin (2012), Vehicle-to-vehicle communication for a platooning system, *Procedia - Social and Behavioral Sciences*, *48*, 1222–1233, doi:10.1016/j.sbspro.2012.06.1098.

[13] Bladh, R., C. Pierre, M. P. Castanier, and M. J. Kruse (2002), Dynamic response predictions for a mistuned industrial turbomachinery rotor using reduced-order modeling, *Journal of Engineering for Gas Turbines and Power*, *124*(2), 311–324, doi:10.1115/1.1447236.

[14] Blaschke, F. (1972), The principle of field orientation as applied to the new transvector closed loop control for rotating field machines, *Siemens Review*, *34*(5), 217–219.

[15] Bohm, A., M. Jonsson, and E. Uhlemann (2013), Performance comparison of a platooning application using the IEEE 802.11p MAC on the control channel and a centralized MAC on a service channel, in *2013 IEEE 9th International Conference on Wireless and Mobile Computing, Networking and Communications (WiMob)*, IEEE, doi:10.1109/wimob.2013.6673411.

[16] Borhan, H., A. Vahidi, A. M. Phillips, M. L. Kuang, I. V. Kolmanovsky, and S. D. Cairano (2012), Mpc-based energy management of a power-split hybrid electric vehicle, *IEEE Transactions on Control Systems Technology*, *20*(3), 593–603, doi:10.1109/TCST.2011.2134852.

[17] Bougrine, S., S. Richard, J.-B. Michel, and D. Veynante (2014), Simulation of {CO} and {NO} emissions in a {SI} engine using a 0d coherent flame model coupled with a tabulated chemistry approach, *Applied Energy*, *113*, 1199 – 1215, doi:http://dx.doi.org/10.1016/j.apenergy.2013.08.038.

[18] Boysal, A., and H. Rahnejat (1997), Torsional vibration analysis of a multi-body single cylinder internal combustion engine model, *Applied Mathematical Modelling*, *21*(8), 481–493, doi:10.1016/s0307-904x(97)00032-2.

[19] Broucke, M., and P. Varaiya (1996), A theory of traffic flow in automated highway systems, *Transportation Research Part C: Emerging Technologies*, *4*(4), 181–210, doi:10.1016/s0968-090x(96)00011-3.

[20] Campolo, C., A. Molinaro, G. Araniti, and A. O. Berthet (2017), Better platooning control toward autonomous driving : An LTE device-to-device communications strategy that meets ultralow latency requirements, *IEEE Vehicular Technology Magazine*, *12*(1), 30–38, doi:10.1109/mvt.2016.2632418.

[21] Castanier, M. P., and C. Pierre (2002), Using intentional mistuning in the design of turbomachinery rotors, *AIAA Journal*, *40*(10), 2077–2086, doi:10.2514/2.1542.

[22] Chan, C., A. Bouscayrol, and K. Chen (2010), Electric, hybrid, and fuel-cell vehicles: Architectures and modeling, *IEEE Transactions on Vehicular Technology*, *59*(2), 589–598, doi:10.1109/tvt.2009.2033605.

[23] Chan, C. C. (2007), The state of the art of electric, hybrid, and fuel cell vehicles, *Proceedings of the IEEE*, *95*(4), 704–718, doi:10.1109/JPROC.2007.892489.

[24] Chau, K. T., C. C. Chan, and C. Liu (2008), Overview of permanent-magnet brushless drives for electric and hybrid electric vehicles, *IEEE Transactions on Industrial Electronics*, *55*(6), 2246–2257, doi:10.1109/TIE.2008.918403.

[25] Chen, L., F. Zhu, M. Zhang, Y. Huo, C. Yin, and H. Peng (2011), Design and analysis of an electrical variable transmission for a series-parallel hybrid electric vehicle, *IEEE Transactions on Vehicular Technology*, *60*(5), 2354–2363, doi:10.1109/TVT.2011.2134876.

[26] Cheng, C., A. McGordon, R. P. Jones, and P. A. Jennings (2012), Development of a comprehensive and flexible forward dynamic powertrain simulation tool for various hybrid electric vehicle architectures, *Proceedings of the Institution of Mechanical Engineers, Part D: Journal of Automobile Engineering*, *226*(3), 385–398, doi:10.1177/0954407011417764.

[27] de Paula, G. T., J. R. B. de A. Monteiro, B. P. de Alvarenga, T. E. P. de Almeida, W. C. A. Pereira, and M. P. de Santana (2018), On-load back EMF of PMSM using maxwell stress tensor, *IEEE Transactions on Magnetics*, *54*(7), 1–15, doi:10.1109/tmag.2018.2829692.

[28] Delfino, F., R. Procopio, and M. Rossi (2002), Evaluation of forces in magnetic materials by means of energy and co-energy methods, *The European Physical Journal B - Condensed Matter*, *25*(1), 31–38, doi:10.1140/e10051-002-0005-y.

[29] Dextreit, C., and I. V. Kolmanovsky (2014), Game theory controller for hybrid electric vehicles, *IEEE Transactions on Control Systems Technology*, *22*(2), 652–663, doi:10.1109/TCST.2013.2254597.

[30] di Bernardo, M., A. Salvi, and S. Santini (2015), Distributed consensus strategy for platooning of vehicles in the presence of time-varying heterogeneous communication delays, *IEEE Transactions on Intelligent Transportation Systems*, *16*(1), 102–112, doi:10.1109/tits.2014.2328439.

[31] Dowell, E. H. (1996), Eigenmode analysis in unsteady aerodynamics - reduced-order models, *AIAA Journal*, *34*(8), 1578–1583, doi:10.2514/3.13274.

[32] D'Souza, K., C. Jung, and B. I. Epureanu (2013), Analyzing mistuned multi-stage turbomachinery rotors with aerodynamic effects, *Journal of Fluids and Structures*, *42*, 388–400, doi:10.1016/j.jfluidstructs.2013.07.007.

[33] Durrani, U., C. Lee, and H. Maoh (2016), Calibrating the wiedemann's vehicle-following model using mixed vehicle-pair interactions, *Transportation Research Part C: Emerging Technologies*, *67*, 227–242, doi:10.1016/j.trc.2016.02.012.

[34] EPUREANU, B., E. DOWELL, and K. HALL (2000), REDUCED-ORDER MODELS OF UNSTEADY TRANSONIC VISCOUS FLOWS IN TURBOMACHINERY, *Journal of Fluids and Structures*, *14*(8), 1215–1234, doi:10.1006/jfls.2000.0320.

[35] EPUREANU, B., K. HALL, and E. DOWELL (2001), REDUCED-ORDER MODELS OF UNSTEADY VISCOUS FLOWS IN TURBOMACHINERY USING VISCOUS–INVISCID COUPLING, *Journal of Fluids and Structures*, *15*(2), 255–273, doi:10.1006/jfls.2000.0334.

[36] Fancher, P., H. Peng, Z. Bareket, C. Assaf, and R. Ervin (2002), Evaluating the influences of adaptive cruise control systems on the longitudinal dynamics of strings of highway vehicles, *Vehicle System Dynamics*, *37*(sup1), 125–136, doi:10.1080/00423114.2002.11666226.

[37] Fathy, H. K., J. A. Reyer, P. Y. Papalambros, and A. G. Ulsov (2001), On the coupling between the plant and controller optimization problems, in *Proceedings of the 2001 American Control Conference. (Cat. No.01CH37148)*, vol. 3, pp. 1864–1869 vol.3, doi:10.1109/ACC.2001.946008.

[38] Fernandes, P., and U. Nunes (2012), Platooning with IVC-enabled autonomous vehicles: Strategies to mitigate communication delays, improve safety and traffic flow, *IEEE Transactions on Intelligent Transportation Systems*, *13*(1), 91–106, doi:10.1109/tits.2011.2179936.

[39] Finesso, R., E. Spessa, and M. Venditti (2014), Layout design and energetic analysis of a complex diesel parallel hybrid electric vehicle, *Applied Energy*, *134*, 573 – 588, doi:http://dx.doi.org/10.1016/j.apenergy.2014.08.007.

[40] Granovskii, M., I. Dincer, and M. A. Rosen (2006), Economic and environmental comparison of conventional, hybrid, electric and hydrogen fuel cell vehicles, *Journal of Power Sources*, *159*(2), 1186–1193, doi:10.1016/j.jpowsour.2005.11.086.

[41] Grewe, T., B. Conlon, and A. Holmes (2007), Defining the general motors 2-mode hybrid transmission, in *SAE Technical Paper. Proceedings of the SAE World Congress and Exhibition*, doi:10.4271/2007-01-0273.

[42] Guler, S. I., M. Menendez, and L. Meier (2014), Using connected vehicle technology to improve the efficiency of intersections, *Transportation Research Part C: Emerging Technologies*, *46*, 121–131, doi:10.1016/j.trc.2014.05.008.

[43] Gundlach, I., and U. Konigorski (2019), Modellbasierte online-trajektorienplanung für zeitoptimale rennlinien, *at - Automatisierungstechnik*, *67*(9), 799–813, doi:10.1515/auto-2019-0032.

[44] Gupta, A., B. Landge, and B.Seth (2013), Modeling and simulation for hybrid electric vehicles. i. modeling, *SAE Technical Paper*, pp. 2009–28–0045, doi:10.4271/2009-28-0045.

[45] Haapala, K., A. Thul, S. Andrasko, C. Muehlfield, B. Bloss, R. Nesbitt, and J. E. Beard (2002), Defining the general motors 2-mode hybrid transmission, in *Design and Development of the 2001 Michigan Tech FutureTruck, a Power-Split Hybrid Electric Vehicle*, doi:10.4271/2002-01-1212.

[46] Hadžiselimović, M., P. Virtič, G. Štumberger, T. Marčič, and B. Štumberger (2008), Determining force characteristics of an electromagnetic brake using co-energy, *Journal of Magnetism and Magnetic Materials*, *320*(20), e556–e561, doi:10.1016/j.jmmm.2008.04.013.

[47] Hall, K. C., R. Florea, and P. J. Lanzkron (1995), A reduced order model of unsteady flows in turbomachinery, *Journal of Turbomachinery*, *117*(3), 375–383, doi:10.1115/1.2835672.

[48] He, X., and J. W. Hodgson (2002), Modeling and simulation for hybrid electric vehicles. i. modeling, *IEEE Transactions on Intelligent Transportation Systems*, *3*(4), 235–243, doi:10.1109/TITS.2002.807781.

[49] Heffner, R. R., K. S. Kurani, and T. S. Turrentine (2007), Symbolism in california's early market for hybrid electric vehicles, *Transportation Research Part D: Transport and Environment*, *12*(6), 396–413, doi:10.1016/j.trd.2007.04.003.

[50] Hong, S.-K., B. I. Epureanu, and M. P. Castanier (2014), Parametric reduced-order models of battery pack vibration including structural variation and prestress effects, *Journal of Power Sources*, *261*, 101–111, doi:10.1016/j.jpowsour.2014.03.008.

[51] Hou, C., L. Xu, H. Wang, M. Ouyang, and H. Peng (2015), Energy management of plug-in hybrid electric vehicles with unknown trip length, *Journal of the Franklin Institute*, *352*(2), 500 – 518, doi:http://dx.doi.org/10.1016/j.jfranklin.2014.07.009, special Issue on Control and Estimation of Electrified vehicles.

[52] Hwang, H. S., D. H. Yang, H. K. Choi, H. S. Kim, and S. H. Hwang (2011), Torque control of engine clutch to improve the driving quality of hybrid electric vehicles, *International Journal of Automotive Technology*, *12*(5), 763–768, doi:10.1007/s12239-011-0088-7.

[53] Ioannou, P., and C. Chien (1993), Autonomous intelligent cruise control, *IEEE Transactions on Vehicular Technology*, *42*(4), 657–672, doi:10.1109/25.260745.

[54] Islam, R., and I. Husain (2010), Analytical model for predicting noise and vibration in permanent-magnet synchronous motors, *IEEE Transactions on Industry Applications*, *46*(6), 2346–2354, doi:10.1109/tia.2010.2070473.

[55] J. Liu, H. P., and Z. Filipi (2005), Modeling and control analysis of toyota hybrid system, in *Advanced Intelligent Mechatronics. Proceedings, 2005 IEEE/ASME International Conference on*, pp. 134–139, doi:10.1109/AIM.2005.1500979.

[56] Joshi, A. G. S., and B. I. Epureanu (2012), Reduced order models for blade-to-blade damping variability in mistuned blisks, *Journal of Vibration and Acoustics*, *134*(5), 051,015, doi:10.1115/1.4006880.

[57] Jung, C., B. I. Epureanu, S. Baik, and M. B. Huffman (2014), Nonlinear reduced order models for the structural dynamics of combustor systems with prestress and friction, *Journal of Computational and Nonlinear Dynamics*, *10*(1), doi: 10.1115/1.4028014.

[58] Karaman, S., and E. Frazzoli (2011), Sampling-based algorithms for optimal motion planning, *The International Journal of Robotics Research*, *30*(7), 846–894, doi:10.1177/0278364911406761.

[59] Kato, S., S. Tsugawa, K. Tokuda, T. Matsui, and H. Fujii (2002), Vehicle control algorithms for cooperative driving with automated vehicles and intervehicle communications, *IEEE Transactions on Intelligent Transportation Systems*, *3*(3), 155–161, doi:10.1109/tits.2002.802929.

[60] Katrašnik, T. (2009), Analytical framework for analyzing the energy conversion efficiency of different hybrid electric vehicle topologies, *Energy Conversion and Management*, *50*(8), 1924 – 1938, doi:http://dx.doi.org/10.1016/j.enconman.2009.04.016.

[61] Kavraki, L., P. Svestka, J.-C. Latombe, and M. Overmars (1996), Probabilistic roadmaps for path planning in high-dimensional configuration spaces, *IEEE Transactions on Robotics and Automation*, *12*(4), 566–580, doi:10.1109/70.508439.

[62] Kianfar, R., P. Falcone, and J. Fredriksson (2015), A control matching model predictive control approach to string stable vehicle platooning, *Control Engineering Practice*, *45*, 163–173, doi:10.1016/j.conengprac.2015.09.011.

[63] Kim, H., J. Kim, and H. Lee (2011), Torque control of engine clutch to improve the driving quality of hybrid electric vehicles, *International Journal of Automotive Technology*, *12*(5), 763–768, doi:10.1007/s12239-011-0088-7.

[64] Kim, N., S. Cha, and H. Peng (2011), Optimal control of hybrid electric vehicles based on pontryagin's minimum principle, *IEEE Transactions on Control Systems Technology*, *19*(5), 1279–1287, doi:10.1109/TCST.2010.2061232.

[65] Kim, S. J., Y.-S. Yoon, S. Kim, and K.-S. Kim (2015), Fuel economy assessment of novel multi-mode parallel hybrid electric vehicle, *International Journal of Automotive Technology*, *16*(3), 501–512, doi:10.1007/s12239-015-0052-z.

[66] Kovacic, I., R. H. Rand, and S. M. Sah (2018), Mathieu's equation and its generalizations: Overview of stability charts and their features, *Applied Mechanics Reviews*, *70*(2), 020,802, doi:10.1115/1.4039144.

[67] Kum, D., H. Peng, and N. K. Bucknor (2011), Supervisory control of parallel hybrid electric vehicles for fuel and emission reduction, *ASME. Journal of Dynamics Systems, Measurements, and Control.*, *133*(6), 061,010–061,010–10, doi:10.1115/1.4002708.

[68] Kum, D., H. Peng, and N. K. Bucknor (2013), Optimal energy and catalyst temperature management of plug-in hybrid electric vehicles for minimum fuel consumption and tail-pipe emissions, *IEEE Transactions on Control Systems Technology*, *21*(1), 14–26, doi:10.1109/TCST.2011.2171344.

[69] Lai, L., and M. Ehsani (2013), Dynamic programming optimized constrained engine on and off control strategy for parallel hev, in *2013 IEEE Vehicle Power and Propulsion Conference (VPPC)*, pp. 1–5, doi:10.1109/VPPC.2013.6671731.

[70] Lee, H., and H. Kim (2005), Improvement in fuel economy for a parallel hybrid electric vehicle by continuously variable transmission ratio control, *Proceedings of the Institution of Mechanical Engineers, Part D: Journal of Automobile Engineering*, *219*(1), 43–51, doi:10.1243/095440705X6514.

[71] Li, S. E., Y. Zheng, K. Li, Y. Wu, J. K. Hedrick, F. Gao, and H. Zhang (2017), Dynamical modeling and distributed control of connected and automated vehicles: Challenges and opportunities, *IEEE Intelligent Transportation Systems Magazine*, *9*(3), 46–58, doi:10.1109/mits.2017.2709781.

[72] Li, S. E., F. Gao, K. Li, L.-Y. Wang, K. You, and D. Cao (2018), Robust longitudinal control of multi-vehicle systems—a distributed h-infinity method, *IEEE Transactions on Intelligent Transportation Systems*, *19*(9), 2779–2788, doi:10.1109/tits.2017.2760910.

[73] Li, X., Z. Sun, D. Cao, Z. He, and Q. Zhu (2016), Real-time trajectory planning for autonomous urban driving: Framework, algorithms, and verifications, *IEEE/ASME Transactions on Mechatronics*, *21*(2), 740–753, doi:10.1109/tmech.2015.2493980.

[74] Lidstrom, K., K. Sjoberg, U. Holmberg, J. Andersson, F. Bergh, M. Bjade, and S. Mak (2012), A modular CACC system integration and design, *IEEE*

Transactions on Intelligent Transportation Systems, *13*(3), 1050–1061, doi:10.1109/tits.2012.2204877.

[75] Lin, C.-C., H. Peng, J. W. Grizzle, and J.-M. Kang (2003), Power management strategy for a parallel hybrid electric truck, *IEEE Transactions on Control Systems Technology*, *11*(6), 839–849, doi:10.1109/TCST.2003.815606.

[76] Lin, C.-C., Z. Filipi, L. Louca, H. Peng, D. Assanis, and J. Stein (2004), Modelling and control of a medium-duty hybrid electric truck, *International Journal of Heavy Vehicle Systems*, *11*(3-–4), 349–173, doi:10.1504/IJHVS.2004.005455.

[77] Lin, C.-C., H. Peng, and J. W. Grizzle (2004), A stochastic control strategy for hybrid electric vehicles, in *Proceedings of the 2004 American Control Conference*, vol. 5, pp. 4710–4715 vol.5.

[78] Liu, J., and H. Peng (2008), Modeling and control of a power-split hybrid vehicle, *IEEE Transactions on Control Systems Technology*, *16*(6), 1242–1251, doi:10.1109/TCST.2008.919447.

[79] Liu, J., H. Peng, and Z. Filipi (2005), Modeling and analysis of the toyota hybrid system, *International Conference on Advanced Intelligent Mechatronics*.

[80] Liu, J., H. Peng, and Z. Filipi (2005), Modeling and control analysis of toyota hybrid system, pp. 134 – 139, doi:10.1109/AIM.2005.1500979.

[81] Ma, J., J. D. Summers, and P. F. Joseph (2011), Application of meshless integral method in soil mechanics, in *Volume 2: 31st Computers and Information in Engineering Conference, Parts A and B*, ASMEDC, doi:10.1115/detc2011-47046.

[82] MacLean, H. L., and L. B. Lave (2003), Evaluating automobile fuel/propulsion system technologies, *Progress in Energy and Combustion Science*, *29*(1), 1–69, doi:10.1016/s0360-1285(02)00032-1.

[83] Mahdisoozani, H., M. Mohsenizadeh, M. Bahiraei, A. Kasaeian, A. Daneshvar, M. Goodarzi, and M. R. Safaei (2019), Performance enhancement of internal combustion engines through vibration control: State of the art and challenges, *Applied Sciences*, *9*(3), 406, doi:10.3390/app9030406.

[84] Mashadi, B., and S. A. M. Emadi (2010), Dual-mode power-split transmission for hybrid electric vehicles, *IEEE Transactions on Vehicular Technology*, *59*(7), 3223–3232, doi:10.1109/TVT.2010.2049870.

[85] Mezouar, Y., and F. Chaumette (2002), Path planning for robust image-based control, *IEEE Transactions on Robotics and Automation*, *18*(4), 534–549, doi:10.1109/tra.2002.802218.

[86] Millithaler, P., É. Sadoulet-Reboul, M. Ouisse, J.-B. Dupont, and N. Bouhaddi (2015), Structural dynamics of electric machine stators: Modelling guidelines

and identification of three-dimensional equivalent material properties for multi-layered orthotropic laminates, *Journal of Sound and Vibration*, *348*, 185–205, doi:10.1016/j.jsv.2015.03.010.

[87] Millo, F., L. Rolando, R. Fuso, and J. Zhao (2015), Development of a new hybrid bus for urban public transportation, *Applied Energy*, *157*, 583 – 594, doi:http://dx.doi.org/10.1016/j.apenergy.2015.03.131.

[88] Mohan, G., F. Assadian, and S. Longo (2013), An optimization framework for comparative analysis of multiple vehicle powertrains, *Energies*, *6*(10), 5507–5537, doi:10.3390/en6105507.

[89] Nakamura, Y., and R. Mukherjee (1991), Nonholonomic path planning of space robots via a bidirectional approach, *IEEE Transactions on Robotics and Automation*, *7*(4), 500–514, doi:10.1109/70.86080.

[90] Naus, G. J. L., R. P. A. Vugts, J. Ploeg, M. J. G. van de Molengraft, and M. Steinbuch (2010), String-stable CACC design and experimental validation: A frequency-domain approach, *IEEE Transactions on Vehicular Technology*, *59*(9), 4268–4279, doi:10.1109/tvt.2010.2076320.

[91] Newell, G. (2002), A simplified car-following theory: a lower order model, *Transportation Research Part B: Methodological*, *36*(3), 195–205, doi:10.1016/s0191-2615(00)00044-8.

[92] Nilsson, J., M. Brännström, E. Coelingh, and J. Fredriksson (2015), Longitudinal and lateral control for automated lane change maneuvers, in *2015 American Control Conference (ACC)*, pp. 1399–1404.

[93] Olson, B. J., S. W. Shaw, C. Shi, C. Pierre, and R. G. Parker (2014), Circulant matrices and their application to vibration analysis, *Applied Mechanics Reviews*, *66*(4), 040,803, doi:10.1115/1.4027722.

[94] Onori, S., L. Serrao, and G. Rizzoni (2010), Adaptive equivalent consumption minimization strategy for hybrid electric vehicles, in *ASME 2010 Dynamic Systems and Control Conference, Volume 1*, ASMEDC, doi:10.1115/dscc2010-4211.

[95] Paganelli, G., S. Delprat, T. M. Guerra, J. Rimaux, and J. J. Santin (2002), Equivalent consumption minimization strategy for parallel hybrid powertrains, in *Vehicular Technology Conference. IEEE 55th Vehicular Technology Conference. VTC Spring 2002 (Cat. No.02CH37367)*, vol. 4, pp. 2076–2081, doi:10.1109/VTC.2002.1002989.

[96] Park, R. H. (1929), Two-reaction theory of synchronous machines generalized method of analysis-part i, *Transactions of the American Institute of Electrical Engineers*, *48*(3), 716–727, doi:10.1109/T-AIEE.1929.5055275.

[97] Pathak, K., and S. Agrawal (2005), An integrated path-planning and control approach for nonholonomic unicycles using switched local potentials, *IEEE Transactions on Robotics*, *21*(6), 1201–1208, doi:10.1109/tro.2005.853484.

[98] Pellerey, P., V. Lanfranchi, and G. Friedrich (2012), Coupled numerical simulation between electromagnetic and structural models. influence of the supply harmonics for synchronous machine vibrations, *IEEE Transactions on Magnetics*, *48*(2), 983–986, doi:10.1109/tmag.2011.2175714.

[99] Pichot, F., D. Laxalde, J.-J. Sinou, F. Thouverez, and J.-P. Lombard (2006), Mistuning identification for industrial blisks based on the best achievable eigenvector, *Computers & Structures*, *84*(29-30), 2033–2049, doi:10.1016/j.compstruc.2006.08.022.

[100] Ploeg, J., D. P. Shukla, N. van de Wouw, and H. Nijmeijer (2014), Controller synthesis for string stability of vehicle platoons, *IEEE Transactions on Intelligent Transportation Systems*, *15*(2), 854–865, doi:10.1109/tits.2013.2291493.

[101] Ploeg, J., N. van de Wouw, and H. Nijmeijer (2014), Lp string stability of cascaded systems: Application to vehicle platooning, *IEEE Transactions on Control Systems Technology*, *22*(2), 786–793, doi:10.1109/tcst.2013.2258346.

[102] Rand, R. H. (2012), Lecture notes on nonlinear vibrations, Cornell University, Ithaca, NY, https://ecommons.cornell.edu/handle/1813/28989.

[103] Reed, D. M., J. Sun, and H. F. Hofmann (2014), A robust adaptive controller for surface-mount permanent magnet synchronous machines, in *American Control Conference (ACC), 2014*, pp. 5236–5241, doi:10.1109/ACC.2014.6858829.

[104] Saber, A. Y., and G. K. Venayagamoorthy (2011), Plug-in vehicles and renewable energy sources for cost and emission reductions, *IEEE Transactions on Industrial Electronics*, *58*(4), 1229–1238, doi:10.1109/tie.2010.2047828.

[105] Saito, A., H. Suzuki, M. Kuroishi, and H. Nakai (2015), Efficient forced vibration reanalysis method for rotating electric machines, *Journal of Sound and Vibration*, *334*, 388–403, doi:10.1016/j.jsv.2014.09.004.

[106] Salari, K., and J. Ortega (2018), Experimental investigation of the aerodynamic benefits of truck platooning, in *SAE Technical Paper Series*, SAE International, doi:10.4271/2018-01-0732.

[107] Samaras, C., and K. Meisterling (2008), Life cycle assessment of greenhouse gas emissions from plug-in hybrid vehicles: Implications for policy, *Environmental Science & Technology*, *42*(9), 3170–3176, doi:10.1021/es702178s.

[108] Sasaki, S. (1998), Toyota's newly developed hybrid powertrain, in *Power Semiconductor Devices and ICs, 1998. ISPSD 98. Proceedings of the 10th International Symposium on*, pp. 17–22, doi:10.1109/ISPSD.1998.702540.

[109] Saxena, S., A. Phadke, and A. Gopal (2014), Understanding the fuel savings potential from deploying hybrid cars in china, *Applied Energy*, *113*, 1127 – 1133, doi:http://dx.doi.org/10.1016/j.apenergy.2013.08.057.

[110] Schulze, T., and T. Fliess (1997), Urban traffic simulation with psycho-physical vehicle-following models, in *Proceedings of the 29th conference on Winter simulation - WSC '97*, ACM Press, doi:10.1145/268437.268764.

[111] Serrao, L., and G. Rizzoni (2008), Optimal control of power split for a hybrid electric refuse vehicle, in *2008 American Control Conference*, pp. 4498–4503, doi:10.1109/ACC.2008.4587204.

[112] Serrao, L., S. Onori, and G. Rizzoni (2009), Ecms as a realization of pontryagin's minimum principle for hev control, in *2009 American Control Conference*, pp. 3964–3969, doi:10.1109/ACC.2009.5160628.

[113] Shabbir, W., and S. A. Evangelou (2014), Real-time control strategy to maximize hybrid electric vehicle powertrain efficiency, *Applied Energy*, *135*, 512 – 522, doi:http://dx.doi.org/10.1016/j.apenergy.2014.08.083.

[114] Silvas, E., T. Hofman, A. Serebrenik, and M. Steinbuch (2015), Functional and cost-based automatic generator for hybrid vehicles topologies, *IEEE/ASME Transactions on Mechatronics*, *20*(4), 1561–1572, doi:10.1109/TMECH.2015.2405473.

[115] Singh, O., T. Sreenivasulu, and M. Kannan (2014), The effect of rubber dampers on engine's NVH and thermal performance, *Applied Acoustics*, *75*, 17–26, doi:10.1016/j.apacoust.2013.07.007.

[116] Song, Z., H. Hofmann, J. Li, J. Hou, X. Han, and M. Ouyang (2014), Energy management strategies comparison for electric vehicles with hybrid energy storage system, *Applied Energy*, *134*, 321–331, doi:10.1016/j.apenergy.2014.08.035.

[117] Song, Z., H. Hofmann, J. Li, X. Han, X. Zhang, and M. Ouyang (2015), A comparison study of different semi-active hybrid energy storage system topologies for electric vehicles, *Journal of Power Sources*, *274*, 400–411, doi:10.1016/j.jpowsour.2014.10.061.

[118] Spargo, C. M., B. C. Mecrow, and J. D. Widmer (2014), A seminumerical finite-element postprocessing torque ripple analysis technique for synchronous electric machines utilizing the air-gap maxwell stress tensor, *IEEE Transactions on Magnetics*, *50*(5), 1–9, doi:10.1109/tmag.2013.2295547.

[119] Spyropoulou, I. (2007), SIMULATION USING GIPPS' CAR-FOLLOWING MODEL—AN IN-DEPTH ANALYSIS, *Transportmetrica*, *3*(3), 231–245, doi:10.1080/18128600708685675.

[120] Stentz, A. (), Optimal and efficient path planning for partially-known environments, in *Proceedings of the 1994 IEEE International Conference on Robotics and Automation*, IEEE Comput. Soc. Press, doi:10.1109/robot.1994.351061.

[121] Swaroop, D., and J. K. Hedrick (1999), Constant spacing strategies for platooning in automated highway systems, *Journal of Dynamic Systems, Measurement, and Control*, *121*(3), 462–470, doi:10.1115/1.2802497.

[122] Tadakuma, K., T. Doi, M. Shida, and K. Maeda (2016), Prediction formula of aerodynamic drag reduction in multiple-vehicle platooning based on wake analysis and on-road experiments, *SAE International Journal of Passenger Cars - Mechanical Systems*, *9*(2), 645–656, doi:10.4271/2016-01-1596.

[123] Tang, D., E. H. Dowell, and D. A. Peters (1998), Reduced order aerodynamic models based upon inflow eigenmodes, *Journal of the American Helicopter Society*, *43*(4), 342–351, doi:10.4050/jahs.43.342.

[124] Tank, T., and J.-P. Linnartz (1997), Vehicle-to-vehicle communications for AVCS platooning, *IEEE Transactions on Vehicular Technology*, *46*(2), 528–536, doi:10.1109/25.580791.

[125] Thomas, D. L. (1979), Dynamics of rotationally periodic structures, *International Journal for Numerical Methods in Engineering*, *14*(1), 81–102, doi:10.1002/nme.1620140107.

[126] Torres, J., R. Gonzalez, A. Gimenez, and J. Lopez (2014), Energy management strategy for plug-in hybrid electric vehicles. a comparative study, *Applied Energy*, *113*, 816 – 824, doi:http://dx.doi.org/10.1016/j.apenergy.2013.08.007.

[127] Treiber, M., A. Hennecke, and D. Helbing (2000), Congested traffic states in empirical observations and microscopic simulations, *Physical Review E*, *62*(2), 1805–1824, doi:10.1103/physreve.62.1805.

[128] Tsugawa, S., S. Kato, and K. Aoki (2011), An automated truck platoon for energy saving, in *2011 IEEE/RSJ International Conference on Intelligent Robots and Systems*, IEEE, doi:10.1109/iros.2011.6094549.

[129] van de Hoef, S., K. H. Johansson, and D. V. Dimarogonas (2015), Fuel-optimal centralized coordination of truck platooning based on shortest paths, in *2015 American Control Conference (ACC)*, IEEE, doi:10.1109/acc.2015.7171911.

[130] Vegendla, P., T. Sofu, R. Saha, M. M. Kumar, and L.-K. Hwang (2015), Investigation of aerodynamic influence on truck platooning, in *SAE Technical Paper Series*, SAE International, doi:10.4271/2015-01-2895.

[131] Walker, P. D., and N. Zhang (2014), Active damping of transient vibration in dual clutch transmission equipped powertrains: A comparison of conventional and hybrid electric vehicles, *Mechanism and Machine Theory*, *77*, 1 – 12, doi: http://dx.doi.org/10.1016/j.mechmachtheory.2014.02.008.

[132] Waltermann, P. (1996), Modelling and control of the longitudinal and lateral dynamics of a series hybrid vehicle, in *Control Applications, 1996., Proceedings of the 1996 IEEE International Conference on*, pp. 191–198, doi:10.1109/CCA.1996.558629.

[133] Wang, R., and S. M. Lukic (2012), Dynamic programming technique in hybrid electric vehicle optimization, in *2012 IEEE International Electric Vehicle Conference*, pp. 1–8, doi:10.1109/IEVC.2012.6183284.

[134] Wang, W., R. Song, M. Guo, and S. Liu (2014), Analysis on compound-split configuration of power-split hybrid electric vehicle, *Mechanism and Machine Theory*, *78*, 272 – 288, doi:http://dx.doi.org/10.1016/j.mechmachtheory.2014.03.019.

[135] Wang, X., X.-B. Wang, and P. R. Gascoyne (1997), General expressions for dielectrophoretic force and electrorotational torque derived using the maxwell stress tensor method, *Journal of Electrostatics*, *39*(4), 277–295, doi:10.1016/s0304-3886(97)00126-5.

[136] Whitefoot, J. W., K. Ahn, and P. Y. Papalambros (2010), The case for urban vehicles: Powertrain optimization of a power-split hybrid for fuel economy on multiple drive cycles, in *Volume 4: 12th International Conference on Advanced Vehicle and Tire Technologies; 4th International Conference on Micro- and Nanosystems*, ASMEDC, doi:10.1115/detc2010-28457.

[137] Wood, E., A. Duran, E. Burton, J. Gonder, and K. Kelly (2015), Epa ghg certification of medium- and heavy-duty vehicles: Development of road grade profiles representative of us controlled access highways, URL: `https://www.nrel.gov/docs/fy15osti/63853.pdf`.

[138] Wu, G., X. Zhang, and Z. Dong (2015), Powertrain architectures of electrified vehicles: Review, classification and comparison, *Journal of the Franklin Institute*, *352*(2), 425 – 448, doi:http://dx.doi.org/10.1016/j.jfranklin.2014.04.018, special Issue on Control and Estimation of Electrified vehicles.

[139] Xie, Y., L. Liu, G. Tang, and W. Zheng (2013), Highly constrained entry trajectory generation, *Acta Astronautica*, *88*, 44–60, doi:10.1016/j.actaastro.2013.01.024.

[140] Xu, Q., and R. Sengupta (), Simulation, analysis, and comparison of ACC and CACC in highway merging control, in *IEEE IV2003 Intelligent Vehicles Symposium. Proceedings (Cat. No.03TH8683)*, IEEE, doi:10.1109/ivs.2003.1212915.

[141] Yi, C., and B. I. Epureanu (2017), Control and design optimization of a novel hybrid electric powertrain system, in *2017 ASME Dynamics and Controls Conference (DSCC)*, ASME, doi:10.1115/dscc2017-5200.

[142] Yi, C., B. I. Epureanu, S.-K. Hong, T. Ge, and X. G. Yang (2016), Modeling, control, and performance of a novel architecture of hybrid electric powertrain system, *Applied Energy*, *178*, 454–467, doi:10.1016/j.apenergy.2016.06.068.

[143] Yi, C., B. I. Epureanu, S.-K. Hong, T. Ge, and X. G. Yang (2016), Modeling, control, and performance of a novel architecture of hybrid electric powertrain system, *Applied Energy*, *178*, 454 – 467, doi:http://doi.org/10.1016/j.apenergy.2016.06.068.

[144] Zeynu, A., and H. Hofmann (2017), Design of field-oriented-control-based brushless, self-excited synchronous field-winding machine with combined finite element/rectifier model, in *2017 IEEE Energy Conversion Congress and Exposition (ECCE)*, IEEE, doi:10.1109/ecce.2017.8096017.

[145] Zhang, M., Y. Yang, and C. C. Mi (2012), Analytical approach for the power management of blended-mode plug-in hybrid electric vehicles, *IEEE Transactions on Vehicular Technology*, *61*(4), 1554–1566, doi:10.1109/TVT.2012.2187318.

[146] Zhang, X., S. E. Li, H. Peng, and J. Sun (2015), Efficient exhaustive search of power-split hybrid powertrains with multiple planetary gears and clutches, *ASME. Journal Dynamics Systems, Measurement, and Control*, *137*(12), 121,006–121,006–12, doi:10.1115/1.4031533.

[147] Zhang, X., H. Peng, and J. Sun (2015), A near-optimal power management strategy for rapid component sizing of multimode power split hybrid vehicles, *IEEE Transactions on Control Systems Technology*, *23*(2), 609–618, doi:10.1109/TCST.2014.2335060.

[148] Zheng, H., J. Zhou, Q. Shao, and Y. Wang (2019), Investigation of a longitudinal and lateral lane-changing motion planning model for intelligent vehicles in dynamical driving environments, *IEEE Access*, *7*, 44,783–44,802, doi:10.1109/access.2019.2909273.

[149] Zheng, Y., S. E. Li, K. Li, and W. Ren (2018), Platooning of connected vehicles with undirected topologies: Robustness analysis and distributed h-infinity controller synthesis, *IEEE Transactions on Intelligent Transportation Systems*, *19*(5), 1353–1364, doi:10.1109/tits.2017.2726038.

[150] Zhou, K., A. Ivanco, Z. Filipi, and H. Hofmann (2015), Finite-element-based computationally efficient scalable electric machine model suitable for electrified powertrain simulation and optimization, *IEEE Transactions on Industry Applications*, *51*(6), 4435–4445, doi:10.1109/TIA.2015.2451094.

[151] Zhou, K., J. Pries, and H. Hofmann (2015), Computationally efficient 3-d finite-element-based dynamic thermal models of electric machines, *IEEE Transactions on Transportation Electrification*, *1*(2), 138–149, doi:10.1109/tte.2015.2456429.

[152] Zhu, F., L. Chen, and C. Yin (2013), Design and analysis of a novel multimode transmission for a hev using a single electric machine, *IEEE Transactions on Vehicular Technology*, *62*(3), 1097–1110, doi:10.1109/TVT.2012.2222456.

[153] Zhu, S., W. ai Shen, and Y. lin Xu (2012), Linear electromagnetic devices for vibration damping and energy harvesting: Modeling and testing, *Engineering Structures*, *34*, 198–212, doi:10.1016/j.engstruct.2011.09.024.

[154] Zhu, Z. Q., and D. Howe (2007), Electrical machines and drives for electric, hybrid, and fuel cell vehicles, *Proceedings of the IEEE*, *95*(4), 746–765, doi: 10.1109/jproc.2006.892482.

[155] Zucca, S., and B. I. Epureanu (2017), Reduced order models for nonlinear dynamic analysis of structures with intermittent contacts, *Journal of Vibration and Control*, *24*(12), 2591–2604, doi:10.1177/1077546316689214.